Fluidic Control of Shear Layer in Dump Combustors Using Microjets

BY

HARISH P. KANCHI
B.E., University of Pune, Pune, India, 2001
M.S., University of Illinois at Chicago, Chicago, USA, 2006

THESIS

Submitted as partial fulfillment of the requirements
for the degree of Doctor of Philosophy in Mechanical Engineering
in the Graduate College of the
University of Illinois at Chicago, 2013

Chicago, Illinois

Defense Committee:

Farzad Mashayek, Chair and Advisor
Suresh Aggarwal
Kenneth Brezinsky
Paul F. Fischer, Argonne National Laboratory
Paul Strykowsky, University of Minnesota

To my parents, family and friends...

ACKNOWLEDGMENTS

Completing this dissertation would not have been possible without the invaluable help and tremendous support from many wonderful people in my life.

First and foremost, I would like to express my sincere gratitude to my advisor, Dr. Farzad Mashayek, for his encouragement, support and guidance to pursue my graduate research and get involved in extracurricular activities as a Ph.D. student. I am extremely grateful to Dr. Paul Fischer for his advice and patience in answering my questions about Nek5000. I would like to thank Dr. Paul Strykowski and his group for their collaboration and significant contribution to this project. In addition, I am thankful to Dr. Suresh K. Aggarwal and Dr. Kenneth Brezinsky for agreeing to be members of my Ph.D. defense committee and for their advice and feedback.

This research project is made possible with support from the Office of Naval Research and the HPC resources provided by the Extereme Science and Engineering Discovery Environment (XSEDE) network and ANSYS, Inc.. A special note of thanks to the administrative and support staff of the Mechanical and Industrial Engineering Department (MIE) for their motivation, support and patience in answering my questions. I also truly appreciate and value the pep talks and encouragement by my colleagues at TRIO Academic Support Program, African American Academic Network, the Graduate Student Council, MIE department and ANSYS, Inc. from whom I have learned valuable life lessons.

ACKNOWLEDGMENTS (Continued)

My time in the Computational Multiphase Transport Laboratory was wonderful with a great group of colleagues from my lab: Karima Russell, Hessam Abbasi, Seyed Ali Hedeyat, and Jon Komperda. Their support and help in figuring things out during my studies are valuable. For example, the coffee break and lunch break discussions with them were something to look forward to. My deep gratitude to my mentors at ANSYS, Peyman Davoudabadi and Ashwini Kumar, without whose knowledge, guidance and assistance, I would not have been able to balance my work at ANSYS and thesis work. My doctoral student life had its share of challenging times and I was able to face such moments of self-doubt and unpredictability with the help of my friends Sandeep Krishnan, Manish Tiwari, Kaustav Sengupta, Manu Murthy and Christopher Pelzman. They have guided me through these tough times and helped me make decisions that motivated me to get to this point.

Completing my doctoral program and living my life as an international student would not have been possible without the unconditional love and support of my family. I dedicate my success and accomplishments to my parents, Pandurang Canchi and Lalitha Canchi, and my brother, Dinesh Canchi. I value their love, sacrifices and care in sending me to the US and making me realize that learning is a lifelong process. I also want to thank my in-laws Nayana Bhat, Ramdas Bhat and sister-in-law Sneha Bhat for their constant support in my endeavors. Finally, I am extremely grateful for the support, motivation and guidance of my wife, Meghna Bhat, which has been invaluable. During the last year of my Ph.D. work, she especially helped me to keep my calm and to stay focused on the bigger picture of fulfilling this dream.

In summary, my time at UIC, the people I have met and lessons I have learned will be beneficial to me for all my life.

Harish P. Kanchi

TABLE OF CONTENTS

CHAPTER **PAGE**

LIST OF TABLES

LIST OF FIGURES

LIST OF FIGURES (Continued)

FIGURE **PAGE**

LIST OF FIGURES (Continued)

FIGURE **PAGE**

LIST OF FIGURES (Continued)

FIGURE **PAGE**

LIST OF FIGURES (Continued)

FIGURE **PAGE**

SUMMARY

There is a worldwide interest to investigate efficient approaches for energy conversion. The tools provided by high fidelity computer simulations can be utilized as predictors for understanding the fluid dynamics and testing novel design concepts in dump combustors. This thesis explores the use of microjets as an effective means to improve the performance of dump combustors using computational fluid dynamics (CFD) tools.

The introduction of microjets from the dump plane at an angle of 45^{o} to the dump plane in dump combustors increases the complexity of the problem. Reynolds averaged Navier-Stokes (RANS) simulations are well suited for performing various parametric studies to arrive at a finalized design for the implementation of microjets in dump combustors. The RANS simulations in this thesis show that adding microjets in dump combustors significantly increases the heat release rate in a round (axisymmetric) and planar (asymmetric) dump combustors.

For a more accurate understanding of the fluid dynamics, large-eddy simulation (LES) is utilized. A semi-implicit Legendre spectral element code, Nek5000, is utilized for the LES studies. The technique of implicit LES with no sub-grid model is utilized for all the LES studies. A reacting flow case with multiple microjets in a combustor, as performed in RANS simulations, is too complex and computationally expensive. Hence, as a first step, non-reacting flow cases with only "one" microjet in the backward-facing step geometry are simulated at different microjet velocities. This LES study to capture the dynamics of the interaction between

the microjet and the primary shear layer in a backward-facing step geometry is the first of its kind.

The microjet is placed on the step face and enters the combustor at an angle of 45° to the step face. Two microjet velocities, 20 m/s and 40 m/s, are simulated to study the effect of microjet in a backward-facing step flow. The microjet cases are simulated with a passive scalar to study the effect of microjet on scalar field and quantify scalar mixing. For both the microjet velocities, the averaged streamwise velocity profiles and streamwise root-mean-squared (rms) velocity profiles are in good agreement with the experimental data.

The introduction of a microjet changes the flow structure in the shear layer and creates a three-dimensional flow pattern as compared to the case without microjet, where the shear layer is primarily two-dimensional. The 40 m/s microjet case penetrates deeper into the flow field, has higher impact on the shear layer, and gives rise to higher turbulent kinetic energy in the shear layer as compared to the 20 m/s microjet case. The microjet entering at a 45° angle to the step face impacts the primary shear layer and gives rise to a counter-rotating vortex pair. This counter-rotating vortex pair entrains the surrounding fluid and enhances the mixing of the passive scalar due to the microjet. The momentum of the 40 m/s microjet carries the passive scalar deeper into the flow field and leads to lower spreading of the mass fraction as compared to the 20 m/s microjet. Various indices are used in the analysis of mixing efficiency. The indices show that mixing is higher in 20 m/s microjet case as compared to the 40 m/s microjet case.

CHAPTER 1

INTRODUCTION

The present economic situation, the volatility of oil prices, and depleting oil reserves have invigorated interest in research for sustainable/renewable energy resources. These factors have challenged researchers to investigate alternative ways of energy production and energy utilization. In addition, a push for greener economy due to environmental concerns provides further incentive for more intense research on liquid-fuel combustion to reduce emissions. Therefore, this thesis work utilizes tools provided by computational fluid dynamics (CFD) to tackle a problem of critical importance to our economy, national security, and environmental protection.

1.1 Dump combustors

An increased demand for compact combustion accompanied by low drag, high turndown, and reliable flame stabilization has invigorated research on dump combustor configurations. A schematic of the planar dump combustor is shown in Figure 1.

Dump combustors are commonly used in air-breathing (ramjet) propulsion systems. The ramjet propulsion systems employ inherently simple geometries, however they require improvements in operability to become more useful technologies. Currently ramjet engines operate successfully over a very narrow range of conditions, greatly limiting maneuverability, range, speed, fuel type and consumption rates. In the absence of turbo-compression, ramjet engines must operate at high velocities using ram compression to achieve high pressures within the

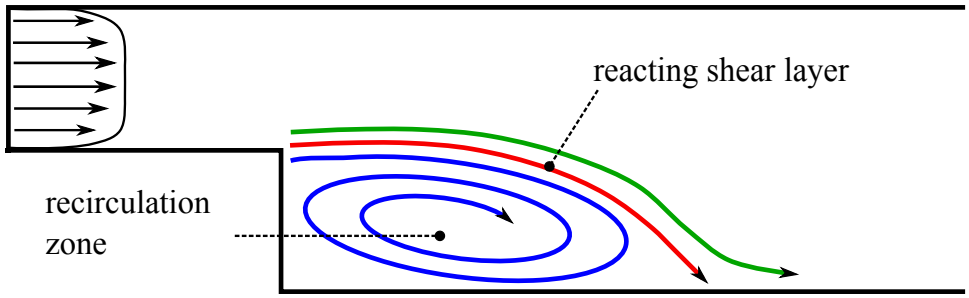

Figure 1. Schematic of a planar dump combustor.

combustor. At these high velocities, the residence times within the combsutor are short, on the order of millisecond in a ramjet, and typically insufficient to fully combust most hydrocarbon fuels. To sustain a flame, highly reactive fuels, such as hydrogen, with high flame speeds are needed and must be stabilized by a flame holder, typically a bluff body. Unfortunately, these fuels are extremely volatile compared to common hydrocarbon jet fuels, which are readily accessible and easily stored. In addition, these bluff-body flame anchors carry excessive thrust penalties. To achieve maximum range and maneuverability, the combustion process must be stable and sustained over a wide operating domain with minimal associated drag. This is inherently difficult because in order to sustain combustion, flames are anchored by a low-speed zone created by a bluff body. Examples of bluff bodies include v-gutters, cavities and sudden expansions, all of which are plagued by high drag. However, this high drag is the very reason that bluff bodies are conducive to flame anchoring, as they create flow separation and the reverse flow needed for residence and relight capability.

The sudden expansion in dump combustors are utilized as bluff bodies for flame stabilization. There are two common geometries of dump combustors, namely round (axisymmetric) and planar (asymmetric). In these dump combustors, the flow separates either over a single-sided step or an axisymmetric sudden expansion, producing a strong recirculation zone that is needed for flame stabilization. Flow separation over the step creates a mechanism for turbulence production leading to vigorous mixing and burning. Large-scale structures form in the shear layer originating from the step. The growth of the mixing layer is thereby governed by the dynamics of these large-scale structures as well as the amplitude and spectral content of disturbances residing in the boundary layer prior to separation. These structures grow by coalescing with their neighbors and by entraining fluid from both sides of the shear layer. Under reacting conditions, premixed reactants and products are folded together in the shear layer, and combustion occurs at the interface between reactants and hot products. The efficiency of the burning process is determined by the diffusive and turbulent mixing that exposes the fresh reactants to high-temperature regions mostly occupied by the products.

The flame anchor geometry is also closely linked to the ability to sustain combustion; therefore simply reducing flame anchor size to reduce drag is not a suitable strategy as it narrows the range of operability. Thus, short combustion residence times and high drag due to stagnation pressure loss behind bluff body flame anchors are problems that hinder ramjet engine performance. To overcome these deleterious effects, various novel control strategies have been explored that create a turbulent flow field with large three-dimensional energetic flow structures, having energy distributed over a wide range of length scales, with reduced spanwise or

azimuthal coherence. These features have been observed in fluidic-based control applications based on countercurrent shear flow technology (1) and microjet flow control (2). These fluidic strategies also have been shown to produce fluidic flame anchors that have perhaps the greatest promise of delivering on-demand mixing control for combustion over the largest range of operating conditions.

Flow control is traditionally considered to be passive or active. Passive control typically has the advantage of simplicity, durability and low cost; however, it often suffers from a limited operating domain and high thrust penalties in propulsion systems. Active control requires intelligent feedback control for system activation and optimization which provides expanded operability; however, it is inherently more complex and often requires fragile sensors/actuators to implement feedback for optimization. The concept of absolute/global instability exploits self-excitation, namely the ability of an open flow to achieve feedback through the vorticity field, eliminating the need for imposed feedback. In this way, fluidic control employs the simplicity of passive control with the authority of active control.

1.2 Problem description

The present work is part of our systematic approach to investigate fluidic control using "horizontal" (streamwise) microjets in dump combustors. The schematic of the implementation of the microjet in the planar dump combustor is shown in Figure 2. The microjets are placed on the step and enter the combustor at an angle of 45^{o} to the flow. In the first part of this thesis, Reynolds-averaged Navier Stokes (RANS) simulations are carried out to test various design concepts of dump combustors with microjets. These simulations are computationally

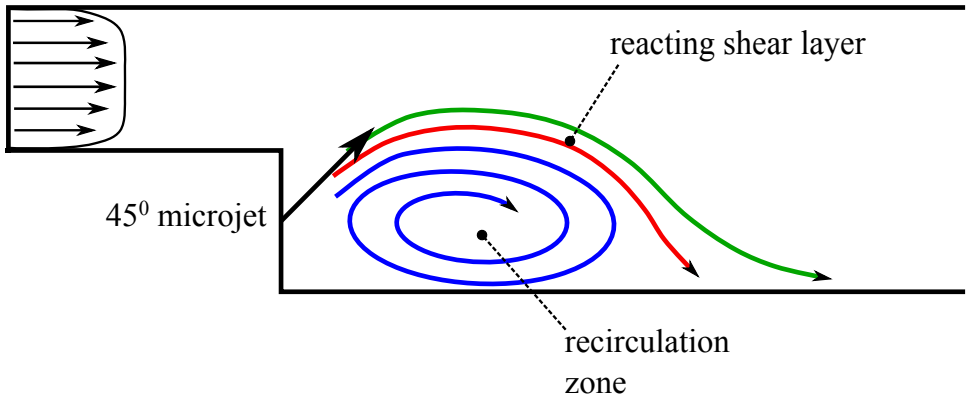

Figure 2. Planar combustor design for implementation of microjets.

affordable and allow many design concepts to be simulated to finalize a working design. The RANS simulations on the finalized combustor geometry are validated with experimental data from our collaborators. Finally, for a more accurate representation of the flow dynamics and to fine tune the design, large-eddy simulations (LES) are performed.

1.3 Approach to the problem

The most accurate approach to simulate the flow inside a combustor is direct numerical simulation (DNS), where turbulence is directly simulated by resolving all the scales of the flow and without resorting to any turbulence model. Unfortunately, DNS is too expensive to be used for flows with moderate to high Reynolds numbers which are of practical interest. The other established computational technique is RANS formulation, where all unsteady turbulence scales are modeled. While this reduces computational cost and enables computation of most engineering applications, it also prevents RANS from adequately capturing the detailed dy-

namics of the flow. LES bridges the gap between DNS and RANS and efficiently computes unsteady turbulent flows in moderately complex geometries at mid range Reynolds numbers found in many real applications. At moderate Reynolds numbers, LES is also more accurate than RANS simulations. LES is based on scale separation in turbulent flows. The large scales, which are anisotropic and sensitive to boundary conditions are computed directly as in DNS, while the small scales that are more isotropic and universal are modeled. The modeling of the small scales reduces the computational cost, while the computation of the large scales provides detailed flow field information. Application of LES outside the well-validated regime requires careful assessment and interpretation of the results, consideration of the effect of numerical method and grid resolution on the solution, and specification of accurate boundary conditions.

1.4 Background studies

During the past few years, our research group at the Computational Multiphase Transport Laboratory (CMTL) has investigated novel design strategies for controlling the flow in the shear layer of planar dump combustors. In order to improve the combustor performance, control techniques such as counter-current shear flow, sloped step extension, and microjets have been investigated. Sengupta et al. (3) conducted reacting flow studies to investigate the effect of countercurrent shear flow and geometric alterations of the step. This investigation of control strategies led to enhanced mixing, increased turbulence and heat release at minimal system penalties; however, the overall effects were somewhat limited. For the countercurrent case, an increase in heat release rate was observed, while step geometry modifications results were similar to that of traditional backward-facing step. Furthermore, previous research by

Sengupta et al. (4) and Russell et al. (5) have shown that multiple, high speed microjets (carrying vertical flow) placed across the lower wall of the inlet duct before the edge of the step in a planar combustor promote increased heat release rates and three-dimensionality in the shear layer. However, the case with two vertical microjets lead to an unstable flame due to large amplitude deformations. Another case with 39 vertical microjets exhibited a stable flame with marginal increase in heat release rate compared to the case without microjets.

Microjets have previously been considered as a means to reduce noise generated from high-speed jets. Alkislar et al. (6) have shown that microjets eliminate large-scale structures and decrease turbulent kinetic energy in the mixing region inside supersonic twin jets. Microjets have also been shown to suppress turbulence in subsonic axisymmetric jets by Arakeri et al. (7) and to reduce shock noise by using aqueous microjets in high-speed jets by Greska and Krothapalli (8). Altay et al. (9) investigated the effect of using steady air injection in the cross-stream direction near the step to stabilize combustion in a backward-facing step combustor. Altay et al. (10) also conducted experiments to investigate the effectiveness of steady air injection near the flame anchoring zone in suppressing thermoacoustic instabilities driven by flame-vortex interaction mechanism. The experiments were conducted on two configurations of air injection, cross-stream direction just upstream of the step and streamwise direction on the face of the step near the edge. It was shown that the streamwise air injection, at an optimum air flow rate, prevents the shedding of an unsteady vortex and eliminates the flame-vortex interaction mechanism, thus resulting in a stable flame to form near the step.

Axisymmetric dump combustors are capable of providing a more stable anchor for the flame compared to planar combustors due to a larger volume of the recirculation bubble for the same diameter ratio. This geometry is more suitable for propulsion applications because of its more complete combustion and better pattern factor at the exit. In the past, experimental studies of sudden expansion flows have been reported in literature over wide range of expansion ratios [1-4]. So and Ahmed (11; 12) have conducted a series of experiments and argued that reattachment length decreases as a result of increase in inlet turbulence. Gould et al. (13) made simultaneous two-component LDV measurements in the reacting turbulent flow field following an axisymmetric sudden expansion. They compared the experimental results with those of their own k-ϵ turbulence model. A good agreement was obtained between the experimental and numerical results for axial velocities and turbulent kinetic energy. However, the numerical value of turbulent kinetic energy were underpredicted compared to measured value in the region between the shear layer and the center line of the flow. Mishra et al. (14) performed computational studies of a premixed flame based dump combustor. They observed that there is a significant reduction in the length of the recirculation zone for higher inlet turbulent intensities and at higher equivalence ratios. Although several studies were undertaken to investigate the characteristics of dump combustors, there has not been any study on the fluidic control of the dump combustor with horizontal microjets.

LES studies are performed for better understanding of the interaction of the jet with the primary flow field. As far as we know, there are no published results on LES of microjets in a backward facing geometry. This makes the study presented in this thesis the first of its kind.

To study and analyze the case of microjets in a backward facing geometry, some of the studies performed on jet in cross flow (JCF) can be utilized. Muppidi and Mahesh (15) carried out DNS studies on trajectories of jets in crossflow. Muppidi and Mahesh (16) also did DNS study of passive scalar transport in transverse jets. Yuan et al. (17) studied jet in crossflow for two velocity ratios at two Reynolds numbers using LES. Deven et al. (18) have carried out various parametric studies of jet in cross flow at different swirl numbers with scalar transport.

1.5 Outline and significant contributions

The thesis is outlined in a way that justifies a systematic approach to the problem of studying the effect of microjets on a shear layer in dump combustors. RANS studies are suitable for performing various design studies. Chapter 2 provides the design studies to investigate the effect of microjets in a round dump combustor and a planar dump combustor. The RANS studies are utilized to arrive at a finalized design for the planar dump combustor with microjets that is provided for experimental validation. LES provides a better understanding of the flow dynamics by resolving the large scales of the flow structure. Chapter 3 provides a brief description of the Nek5000 code, based on the Legendre spectral element method, that is utilized for the LES studies. Before moving to perform complex simulations with a microjet in a backward-facing step flow, LES validation studies have been performed on flow over a backward-facing step, reported in chapter 4. In addition to the validation studies, the effect of inflow boundary condition on the developing flow are studied. All the experience gained from the validation studies are utilized for setting up and performing LES studies of the effect of single microjet in a backward-facing step flow. Chapter 5 provides the results of these LES studies. Finally,

chapter 6 provides conclusions for this thesis and the future work that can be performed on this project.

The significant contributions from this thesis are enumerated below:

1. Design simulations are conducted for implementation of microjets using RANS equations in the framework of standard k-ϵ turbulence models. The effect of microjets on the primary flow and combustion is studied in two dump combustor geometries, namely round (axisymmetric) and planar dump combustors. Microjets are placed on the dump plane and angled at 45^{o} to the flow axis. Compared to the baseline case without microjets, simulations show that adding microjets results in an increase in heat release rate of $\sim 22\%$ and $\sim 140\%$ in round and planar dump combustors, respectively. A parametric study is conducted by varying the microjet velocity. The finalized design for implementation of microjets, based on RANS simulations, has been utilized for experiments. The data collected from the experiments qualitatively confirm the trends predicted by the simulations (2).

2. For a more accurate understanding of the fluid dynamics, LES is utilized. A semi-implicit Legendre spectral element code, Nek5000, is utilized for the LES studies. The technique of implicit LES with no sub-grid model is utilized for all the LES studies. Two different backward-facing step configurations are simulated at Reynolds numbers 5000 and $28,000$ to test the implicit LES technique. The simulations results of Nek5000 for averaged streamwise velocity data compare well with the published experimental data and DNS

results. Hence, explicit filtering is a viable choice for sub-grid dissipation mechanism in LES studies using spectral element method.

3. In addition, the effect of turbulent inflow boundary condition at the two Reynolds numbers are also evaluated. A stochastic model for generating inflow turbulence is implemented and compared to the method of generating inflow turbulence with random fluctuations. Frequency analysis is performed at various points in the boundary layer and in the shear layer to study the effect of inflow boundary condition. The spectral method requires correlated velocity input data generated by the stochastic model for predicting the correct transition to turbulence at $\mathsf{Re} = 5000$. It is also observed that at $\mathsf{Re} = 5000$, the semi-implicit method requires small time step size to correctly predict transition to turbulence. The large time step size leads to laminarization of the flow in the inlet channel. The two techniques, stochastic and random, of generating inflow turbulence give similar results for $\mathsf{Re} = 28,000$ (19).

4. The validated implicit LES technique is utilized for performing LES studies in a planar dump combustor with microjets. A reacting flow case with multiple microjets in a combustor, as performed in RANS simulations, is too complex and computationally expensive. Hence as a start, non-reacting cases with only "one" microjet in the backward-facing step geometry are simulated at different microjet velocities. The LES study to capture the dynamics of the interaction between the microjet and the primary shear layer in a backward-facing step geometry is the first of its kind. Hence, a step by step approach is adopted to establish a process for conducting these LES studies. The microjet is placed

on the step face and its flow enters the combustor at an angle of 45^o to the step face. Two microjet velocities, 20 m/s and 40 m/s, are simulated to study the effect of microjet in a backward-facing step flow. The microjet cases are simulated with a passive scalar to study the effect of microjet on scalar field and quantify scalar mixing. In addition, RANS simulations are performed on the same geometry at the two microjet velocities within the framework of k-ϵ turbulence models. For both the microjet velocities, the averaged streamwise velocity profiles and streamwise root-mean-squared (rms) velocity profiles are in good agreement with the experimental data. RANS simulations underpredict the penetration of the 20 m/s microjet, while the penetration of the 40 m/s microjet is well predicted. Jets entering at a 45^o angle to the step face impact the primary shear layer and give rise to a counter-rotating vortex pair. This counter-rotating vortex pair entrains the surrounding fluid and enhances the mixing of the passive scalar due to the microjet. The mixing efficiency of the passive scalar is analyzed using various indices.

CHAPTER 2

RANS SIMULATIONS OF DUMP COMBUSTORS WITH MICROJETS

2.1 Introduction

The objective of RANS simulations is to perform design studies to evaluate the effectiveness of microjets in round and planar dump combustors. The studies are utilized in arriving at a finalized design that can be experimentally validated.

This chapter is structured as follows: first a description of the numerical approach for the reacting flow simulations is presented. Then, in the following sections the results are presented and the effect of microjets on the overall combustor performance is discussed. Finally, experimental validation study in a planar combustor with microjets is provided, followed by some concluding remarks.

2.2 Numerical approach

The design study for implementation of microjets involves the selection of design parameters based on mean flow characteristics. We implement a framework that would resolve the mean flow with acceptable accuracy and manageable computational cost to allow for a large number of simulations that are needed at this "design" stage of our systematic study.

Density variation due to pressure changes are negligible because of low Mach number at the combustor inlet, and the primary density variation across the flame is due to large temperature gradients. Hence, we perform the computations considering the flow to be steady-state with

a temperature-dependent density. The governing equations for the turbulent flow encountered in this design study are the steady-state RANS equations solved using the commercial code ANSYS Fluent.

Continuity:

$$\frac{\partial}{\partial x_i}\left(\rho U_i\right) = 0 \tag{2.1}$$

Momentum:

$$\frac{\partial}{\partial x_j}\left(\rho U_i U_j\right) = -\frac{\partial P}{\partial x_i} + \left[\mu\left(\frac{\partial U_i}{\partial x_j} + \frac{\partial U_j}{\partial x_i} - \frac{2}{3}\delta_{ij}\frac{\partial U_l}{\partial x_l}\right)\right] + \frac{\partial}{\partial x_i}\left(-\rho\overline{u_i' u_j'}\right) \tag{2.2}$$

Species transport:

$$\frac{\partial}{\partial x_i}\left(\rho U_i Y_p\right) = \frac{\partial}{\partial x_i}\left[\left(\frac{\mu}{Sc} + \frac{\mu_t}{Sc_t}\right)\frac{\partial Y_p}{\partial x_i}\right] + R_p \tag{2.3}$$

where, ρ is the mean density, U_i is the mean velocity, P is the mean pressure, μ is the molecular viscosity, $-\rho\overline{u_i' u_j'}$ is the Reynolds stresses, Y_p is the mean mass fraction of species p, Sc is the Schmidt number, μ_t is the turbulent (or eddy) viscosity and R_p is the mean rate of production of species p due to chemical reaction. The value of turbulent Schmidt number (Sc_t) is assumend to be 0.7. The modeled energy equation is given by,

Energy, h_s:

$$\frac{\partial}{\partial x_i}\left(\rho U_i h_s\right) = \frac{\partial}{\partial x_i}\left[\left(\frac{\mu}{Pr} + \frac{\mu_t}{Pr_t}\right)\frac{\partial h_s}{\partial x_i}\right] + S_h \tag{2.4}$$

where, S_h includes the heat of chemical reaction, Pr is the Prandtl number and the turbulent Prandtl number (Pr_t) is taken as 0.85.

To correctly account for turbulence, Reynolds stresses are modeled in order to achieve closure of equation Equation 2.2. The method of modeling employed utilizes the Boussinesq hypothesis to relate the Reynolds stresses to the mean velocity gradients within the flow. Therefore the Reynolds stresses are given by:

$$-\rho\overline{u_i' u_j'} = \mu_t \left(\frac{\partial U_i}{\partial x_j} + \frac{\partial U_j}{\partial x_i} \right) - \frac{2}{3} \left(\rho k + \mu_t \frac{\partial U_i}{\partial x_i} \right) \delta_{ij} \tag{2.5}$$

In Equation 2.5, μ_t is the turbulent (or eddy) viscosity and k is the turbulent kinetic energy. As in our previous work (20; 3), we select the optimal turbulence model by comparing the model predictions with the experimental data. The standard $k-\varepsilon$ model provided better agreement with the experimental data for the round combustor (13). The same RANS model was also used for the planar combustor. In the two-equation standard $k-\varepsilon$ turbulence model, the turbulent viscosity is computed through the solution of two additional transport equations for the turbulent kinetic energy, k, and the turbulence dissipation rate, ε. The modeled transport equation for k and ε, are given as:

$$\frac{\partial}{\partial x_i}(\rho k U_i) = \frac{\partial}{\partial x_j} \left[\left(\mu + \frac{\mu_t}{\sigma_k} \right) \frac{\partial k}{\partial x_j} \right] + P_k - \rho\varepsilon \tag{2.6}$$

$$\frac{\partial}{\partial x_i}(\rho \varepsilon U_i) = \frac{\partial}{\partial x_j} \left[\left(\mu + \frac{\mu_t}{\sigma_\varepsilon} \right) \frac{\partial \varepsilon}{\partial x_j} \right] + C_{1\varepsilon} \frac{\varepsilon}{k}(P_k) - C_{2\varepsilon} \rho \frac{\varepsilon^2}{k} \tag{2.7}$$

In Equation 2.6 and Equation 2.7, σ_k and σ_ε are the turbulent Prandtl numbers for k and ε, respectively. The production of turbulence kinetic energy, P_k is approximated in a manner consistent with the Boussinesq hypothesis by

$$P_k = \mu_t S^2 \tag{2.8}$$

S is the modulus of the mean rate-of-strain tensor, defined by

$$S = \sqrt{2 S_{ij} S_{ij}}; \qquad S_{ij} = \frac{1}{2}\left(\frac{\partial U_j}{\partial x_i} + \frac{\partial U_i}{\partial x_j}\right) \tag{2.9}$$

The turbulent viscosity is computed through a formulation of k and ε, given as

$$\mu_t = \rho C_\mu \frac{k^2}{\varepsilon} \tag{2.10}$$

The values of the constants in the standard $k-\varepsilon$ model are given as

$$C_{1\varepsilon} = 1.44, C_{2\varepsilon} = 1.92, C_\mu = 0.09, \sigma_k = 1.0, \sigma_\varepsilon = 1.3 \tag{2.11}$$

Most fuels are fast burning, and the overall rate of reaction is controlled by turbulent mixing. In premixed flames, the turbulence slowly convects/mixes cold reactants and hot products into the reaction zones, where reaction occurs rapidly. In such cases, the combustion is said to be mixing-limited, and the complex, and often unknown, chemical kinetic rates can be safely neglected.

In this work, we have considered a single step global reaction for propane as the fuel premixed with air,

$$C_3H_8 + 5O_2 \rightarrow 3CO_2 + 4H_2O \tag{2.12}$$

ANSYS FLUENT provides a turbulence-chemistry interaction model, based on the work of Magnussen and Hjertager (21), called the eddy-dissipation model. The model assumes that in the limit of high Reynolds and Damkohler numbers the mean reaction rate is mainly controlled by turbulent mixing time or the rate of dissipation of the eddies. The mean rate of production of species (R_p) is estimated by the smaller (i.e., limiting value) of the two values of mass fractions for reactants ($Y_{reactants}$) or products ($Y_{products}$), as given below:

$$R_p = A\rho\frac{\varepsilon}{k}\min\left(\frac{Y_{reactants}}{s}, B\frac{Y_{products}}{s}\right) \tag{2.13}$$

where, A and B are empirical constants with values 4.0 and 0.5, respectively, and s is the stoichiometric coefficient. In Equation 2.13, the chemical reaction rate is governed by the large-eddy mixing time scale, k/ε. Combustion proceeds whenever turbulence is present ($k/\varepsilon > 0$), and an ignition source is not required to initiate combustion. The combustion is initiated with a high temperature patch over the entire computational domain. This is usually acceptable for non-premixed flames, but in premixed flames, the reactants will burn as soon as they enter the computational domain, upstream of the flame stabilizer. To remedy this, ANSYS

FLUENT provides the finite-rate/eddy-dissipation model, where reaction rates are calculated by the eddy-dissipation model (Equation 2.13) and the Arrhenius law as given below.

$$R_p = AT^{\beta} e^{-E/RT} \tag{2.14}$$

where, A is the pre-exponential factor, β is the temperature exponent, E is the activation energy for the reaction, R is the universal gas constant, and T is the mean temperature.

The net reaction rate is taken as the minimum of these two rates. In practice, the Arrhenius rate acts as a kinetic "switch", preventing reaction before the flame holder. Once the flame is ignited, the eddy-dissipation rate is generally smaller than the Arrhenius rate, and reactions are mixing-limited. Finally, the density is related to the temperature through a modified equation of state for incompressible flow. This model is called the "incompressible ideal gas" model in ANSYS FLUENT.

$$\rho = \frac{P_{op}}{RT} \tag{2.15}$$

where, P_{op} is the operating pressure.

2.2.1 Combustor geometry

The schematic of the round combustor geometry with microjets is shown in Figure 3. The geometry for this combustor is taken from Gould et al. (13) who examined the reacting flow without any microjets. The combustor has a step height of $H = 38.1$ mm and an inlet radius equal to H. The radius, R, of the combustor is $2H$ and its length is $20H$. Premixed propane-air mixture enters the combustor at an axial velocity of $U_o = 22$ m/s with an equivalence

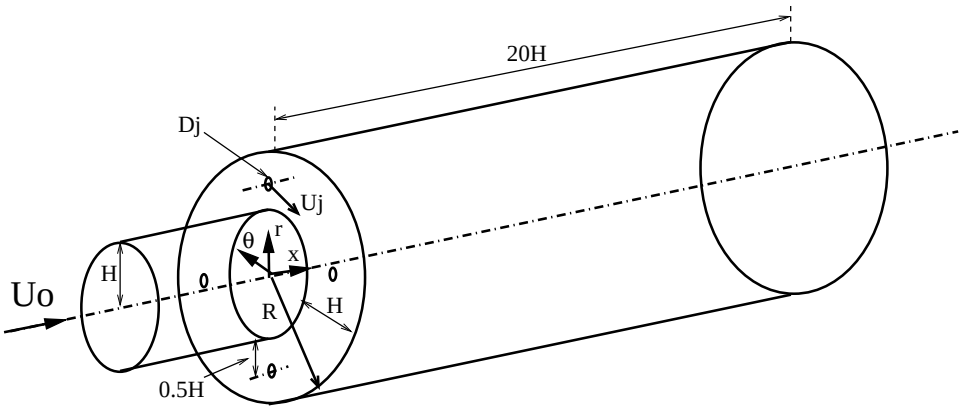

Figure 3. Round combustor design for implementation of microjets. The origin is located as shown in the figure.

ratio of $\phi = 0.5$, temperature $T_o = 298$ K and a turbulence intensity is 5%. Four microjets, with diameter $D_j = 1$ mm, are placed symmetrically at a distance of $1.5H$ from the axis. Air enters through the microjets at an angle of 45^o to the axis with different velocities. The wall temperature is not provided from the experiment; therefore, we assume isothermal walls with temperature of $T_w = 300$ K. Zero diffusion flux is assumed at the outflow for all the flow variables. The symmetric placement of microjets reduces the full three dimensional (3D) computational domain to just a 3D symmetric sector of the combustor with one microjet. In order to resolve the intense mixing between the microjets and the shear layer, a dense mesh is required around the microjet. Therefore, a careful grid resolution study (not shown) was conducted to determine the appropriate grid. We found that a grid with approximately 1.58 million hexahedral cells provide a converged solution.

The schematic of the planar dump combustor with multiple microjets is shown in Figure 4. The step height (H) is 20 mm. The length of the combustor before the step edge is 2H and the length after the step is 10H. For our 3D simulations, only half of the combustor width is modeled at 4H wide, and symmetry and wall boundary conditions are applied in the spanwise direction. Four microjets of diameter $D_j = 1$ mm are located at a distance of 0.5H from the combustor floor. The center-to-center spacing of microjets is H. Spacing from the center of the microjets to the wall or symmetry boundary is 0.5H. Air enters through the microjets at a 45^o angle to the x-axis in the x-z plane. The velocity profile for the premixed propane-air mixture at the main inlet was taken from previous experiments (1) (without microjets) and has a centerline velocity of $U_o = 12.5$ m/s. Turbulence intensity is 5% of the inlet velocity. The premixed propane-air mixture has an equivalence ratio of 0.5 and a reference temperature $T_o = 298$ K. The walls are assumed isothermal with a temperature of $T_w = 300$ K. A grid with 3.24 million cells is used for simulating the planar dump combustor with microjets.

2.2.2 Validation study

We validate our modeling approach by simulating the baseline flow (without microjets) and comparing the results with the experimental data of Gould et al. (13) for the reacting flow. An axisymmetric flow is considered for the simulation of the baseline flow. Figure 5 shows the normalized axial velocity profiles for the simulation along with the experimental values. There is a good agreement between the predicted and experimental values over the entire length of combustor. The maximum difference is in the shear layer close to the sudden expansion, where large heat release and consequent volumetric expansion occurs.

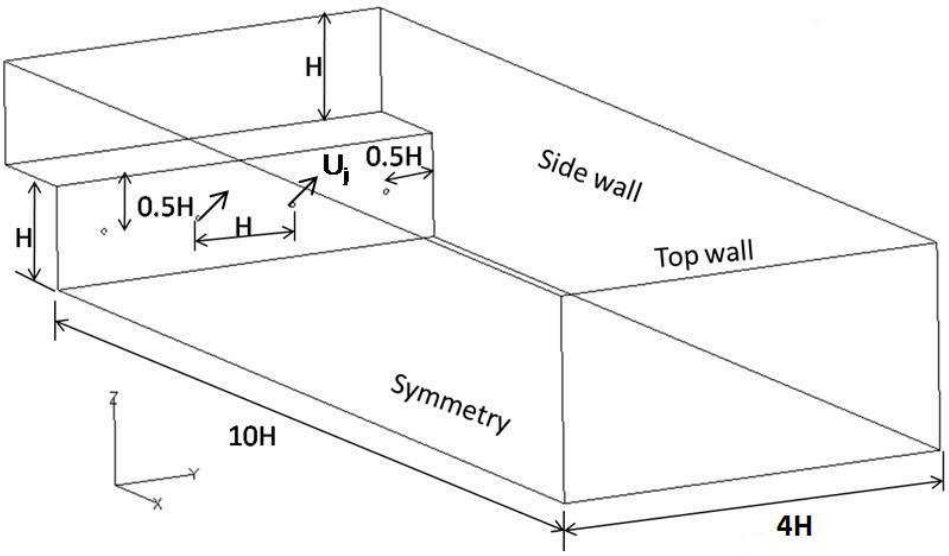

Figure 4. Planar combustor design for implementation of microjets. The origin is located at the trailing edge of the symmetry plane.

An examination of the normalized temperature profiles (not shown here) revealed that the predicted temperatures are in good agreement in the potential core of the flow and in the early part of the flame zone ($x/H \leq 5.0$). However, there are some differences on the product side and near the wall. These discrepancies may be because of the heat loss through the wall during the experiment. Also, as the wall boundary condition was not outlined in the experiment an isothermal wall approximation in the simulations may be inadequate to predict the exact values. Moreover, a single-step mechanism is an overly simplistic approximation of the flame chemistry and therefore is probably responsible for overpredicting the temperature. Overall,

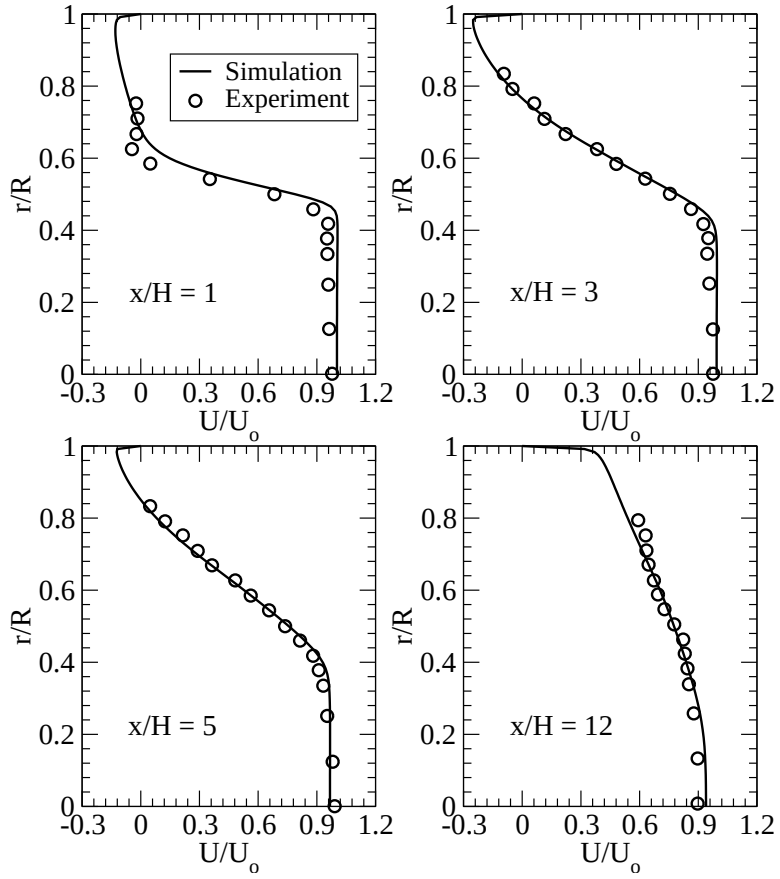

Figure 5. Comparison of simulated axial velocity values with experimental values.

the validation study indicates that the mean velocities match well with the experiment while there are differences in the mean temperature on the product side.

2.3 Results and discussions

Different microjet velocities are considered for parametric studies in both combustor geometries, as indicated in Table I along with their corresponding mass ratios. The mass ratio is

defined as the ratio of the total mass flow rate of the microjets to the incoming (primary) mass flow rate in the combustor. Below, the effect of the microjet velocities is discussed with results shown for two representative velocities for each combustor geometry.

Round Combustor	U_j (m/s)	0 (baseline case)	45.5	91. 0	136.5	182.0	227.5
	Mass ratio (%)	—	0.095	0.190	0.286	0.381	0.476
Planar Combustor	U_j (m/s)	0 (baseline case)	25.0	50.0	75.0	100.0	—
	Mass ratio (%)	—	0.26	0.52	0.78	1.04	—

TABLE I

MICROJET AIR VELOCITIES AND RESPECTIVE MASS RATIOS.

2.3.1 Effect on the shear layer

Introducing microjets in the combustor changes the flow structure in the shear layer. Figure 6 shows the axial velocity profiles for two representative microjet velocities, U_j of 91 m/s and 227.5 m/s at six different locations along the length of the round combustor. The results are shown in the plane of the microjet and in a plane at an angle of 45° to the plane of the microjet. Note that for this case, where four microjets are used, the 45° plane is the symmetry plane between two adjacent microjets. This plane serves to indicate the extent of azimuthal

penetration of the microjet. The 91 m/s microjet has a minimal effect in the 45° plane and the effect of the microjet vanishes after x/H = 8, finally resulting in equal axial velocity in both planes at x/H = 16. Once the effect of the microjets diminishes, the axial velocity values approach the baseline case (no microjet) values. The 227.5 m/s case has considerably higher microjet penetration leading to unequal axial velocities in the two planes. This inequality is caused by the greater expansion of the microjet in the azimuthal direction compared to the 91 m/s case.

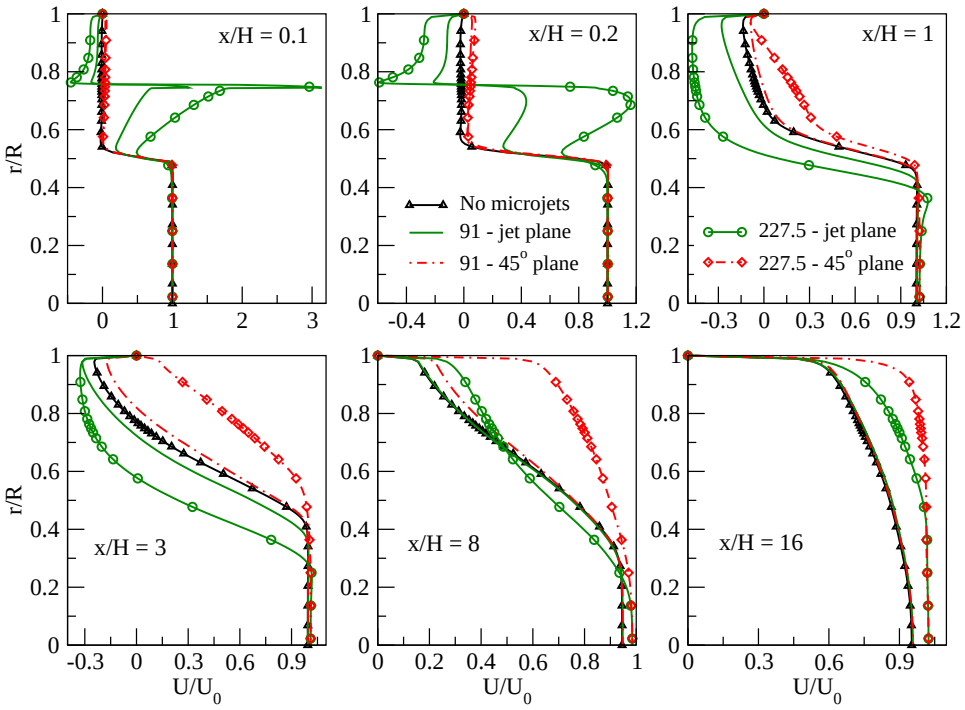

Figure 6. Normalized axial velocity profiles for 91 m/s and 227.5 m/s cases at different x/H locations for two planes in the round combustor.

The normalized x-velocity profiles along the axial direction of the planar combustor are shown in Figure 7. The profiles are studied at two planes. One is in x-z plane containing one of the microjets, henceforth referred to as the "jet" plane. The second plane is in between two microjets, labled on the figure as the "no jet" plane. The microjet plane contains the second microjet from the symmetry boundary ($y/H = 1.5$) to avoid the effects of the wall. For the 50 m/s case, profiles in the microjet plane exhibit penetration of the flow until approximately $x/H = 2.5$, and exhibit higher regions of negative velocities in the shear layer region for $x/H = 1$. When comparing the profiles in the two planes, we observe that there is non-uniformity, especially for the 100 m/s case. The effect of the 50 m/s microjet vanishes at $x/H = 5$ and afterwards the flow behaves similarly to the baseline case. The axial velocity for the 100 m/s case has a more uniform profile compared to the profile in the baseline case at $x/H = 5$. This is a consequence of the higher heat release that leads to a significant expansion of the flow in the reactant (bottom) side of the combustor. Therefore, it is concluded that the strength of the original shear layer is vastly diminished for the 100 m/s case. This is an important finding as the conventional wisdom would suggest not to alter the shear layer. Nevertheless, as we see later in this chapter, this case has the highest increase in heat release rate.

A close inspection of the velocity profiles in Figure 6 and Figure 7 reveals that for both of the combustors, the microjets impinge on the incoming flow and change the flow structure in the combustor, hence affecting the volume of the recirculation zone which is larger for higher microjet velocities. The change in the shape of the shear layer adds three-dimensionality to the flow and increases the mixing of reactants and products. Meanwhile, the higher levels of

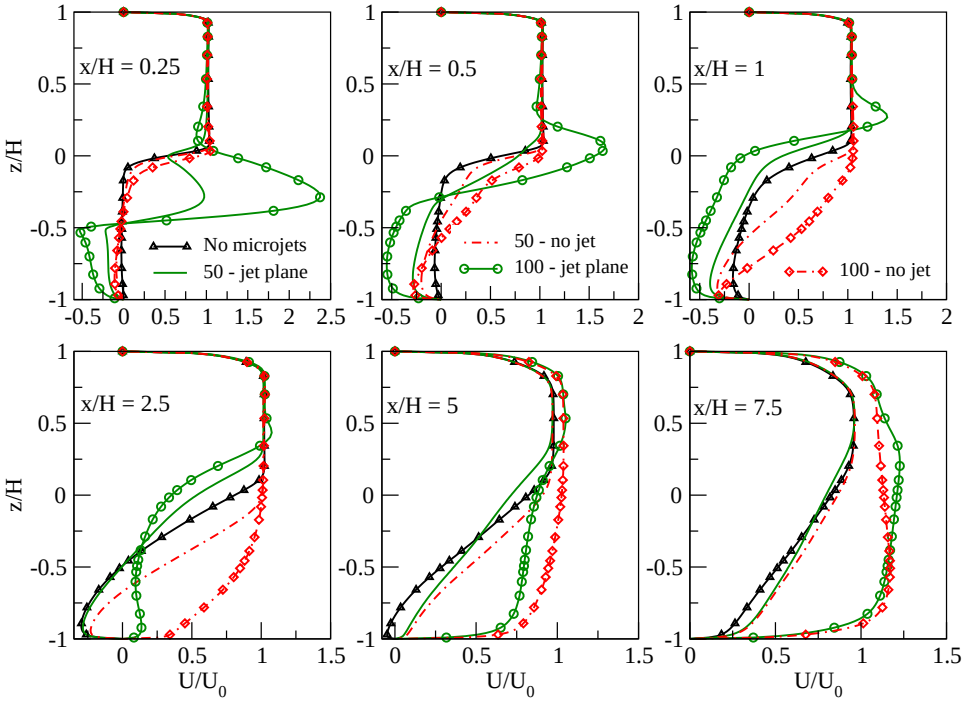

Figure 7. Normalized axial velocity profiles for 50 m/s and 100 m/s cases at different x/H locations for two planes in the planar combustor.

turbulence generated in the reacting shear layer in cases with higher velocity microjets produce a faster and more uniform flame speed near the exit. We elaborate on these below.

2.3.2 Turbulent kinetic energy

The normalized turbulent kinetic energy profiles for the round combustor are shown in Figure 8. For the 91 m/s case, in the near field ($x/H \leq 3$) the microjet plane has higher turbulence than the 45° plane and the baseline case. At $x/H = 3$, the change in flow structure and reaction increases the kinetic energy in the 45° plane, resulting in equal peak kinetic

energy in both planes. Downstream of $x/H = 8$, the 45° plane has higher kinetic energy than the microjet plane and the baseline case. The cross-stream location of the peak kinetic energy changes along the length of the combustor. Close to the dump plane ($x/H = 0.1$ and 0.2) the peak is closer to the microjet. At $x/H = 1$, the peak is in the shear layer and further downstream it is located in the high temperature region between $0.7 \leq r/R \leq 0.8$. The difference in turbulent kinetic energy between the no-microjet case and 91 m/s case is small at locations downstream

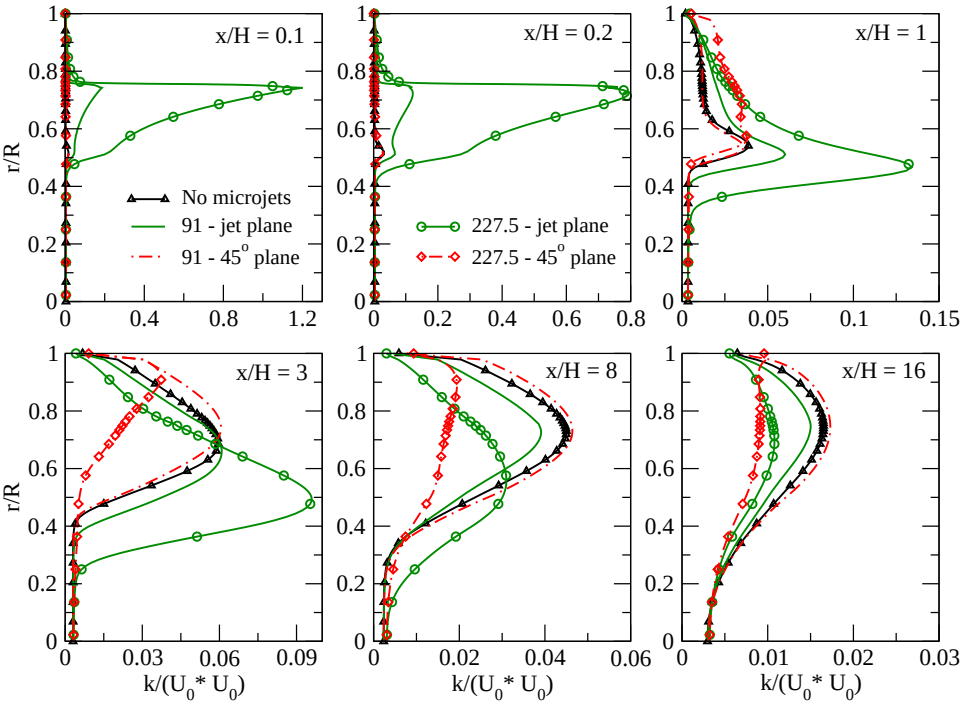

Figure 8. Normalized turbulent kinetic energy profiles for 91 m/s and 227.5 m/s cases at different x/H locations for two planes in the round combustor.

of $z/H = 3$. The 227.5 m/s microjet creates a strong turbulence in the plane of the microjet which has higher kinetic energy than that in 45° plane upstream of $x/H = 16$. In the plane of the microjet, the peak kinetic energy is around the microjet in the near field close to the step. At $x/H = 1$ the peak is in the shear layer, and downstream of $x/H = 1$ the peak starts shifting towards the high temperature region. In contrast, the 45° plane has peak kinetic energy close to the wall. Around $x/H = 8$ and downstream of it the 91 m/s and the baseline cases have higher turbulence levels than in the 227.5 m/s case. This is consistent with the observation of flatter velocity profiles at these locations when the microjet velocity is the highest (see Figure 6). A flatter velocity profile, i.e. smaller radial velocity gradient, leads to a lower production of turbulent kinetic energy.

For the planar combustor, the normalized turbulent kinetic energy profiles at different axial locations are shown in Figure 9. For $x/H = 2.5$, the profiles in the microjet plane show that kinetic energy in this region affects both the shear layer and the main flow. The mixing and non-uniformity that is generated by the microjets causes higher values of turbulent kinetic energy to occupy a larger region of the combustor. This increase in kinetic energy produces higher burning velocities. Profiles taken in-between two microjets show that the kinetic energy in this plane dominates in the shear layer near the bottom wall ($x/H = 2.5$). The mixing that occurs in-between two microjets causes the flow in this region to move downwards producing higher turbulence near the floor of the combustor. Whereas, the flow that is directly in front of the microjets infuses and mixes with the primary flow-field, causing higher turbulence above the shear layer. At $x/H = 5$ and 7.5, the baseline case has higher turbulent kinetic energy in the

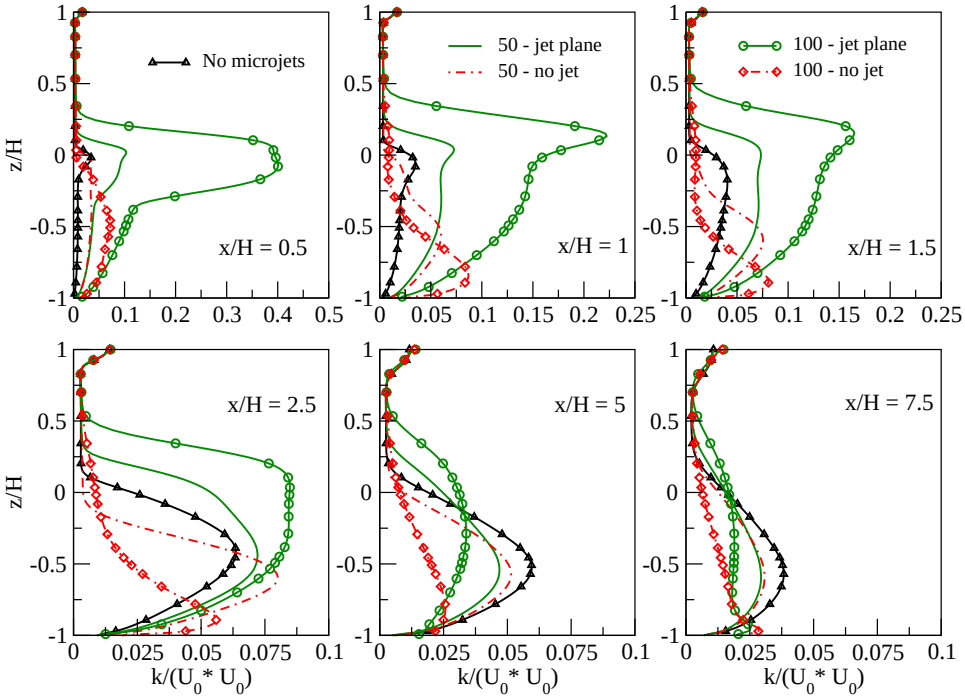

Figure 9. Normalized turbulent kinetic energy profiles for 50 m/s and 100 m/s cases at different x/H locations for two planes in the planar combustor.

lower half of the combustor because of the flatter mean velocity profiles (in cases with higher microjet velocity) leading to lower turbulent kinetic energy production, as also mentioned above for the round combustor.

2.3.3 Flame wrinkling

In the absence of microjets the mean propane mass fraction is uniform in the azimuthal direction for the round combustor and uniform in the wall normal direction for the planar combustor. With the introduction of microjets the shape of the flame is significantly altered.

For the round combustor, the change in propane mass fraction for the 91 m/s and 227.5 m/s microjets in plane $x/H = 2$ are shown in Figure 10. The figure shows the full cross section and sector views. For the planar combustor, the mass fractions for 50 m/s microjet and 100 m/s microjet in plane $x/H = 1$ are shown in Figure 11. The fuel mass fraction distribution is considerably affected by the microjet velocity. The high gradient regions of the fuel mass fraction indicate the flame zone in which the premixed propane-air is consumed. Hence, we conclude that the flame surface area increases with increasing microjet velocity. Furthermore, since there is higher turbulence in the plane of the microjet the flame is thicker at that plane. Flame expands tangentially over the length of the round combustor and in the wall normal direction over the length of the planar combustor.

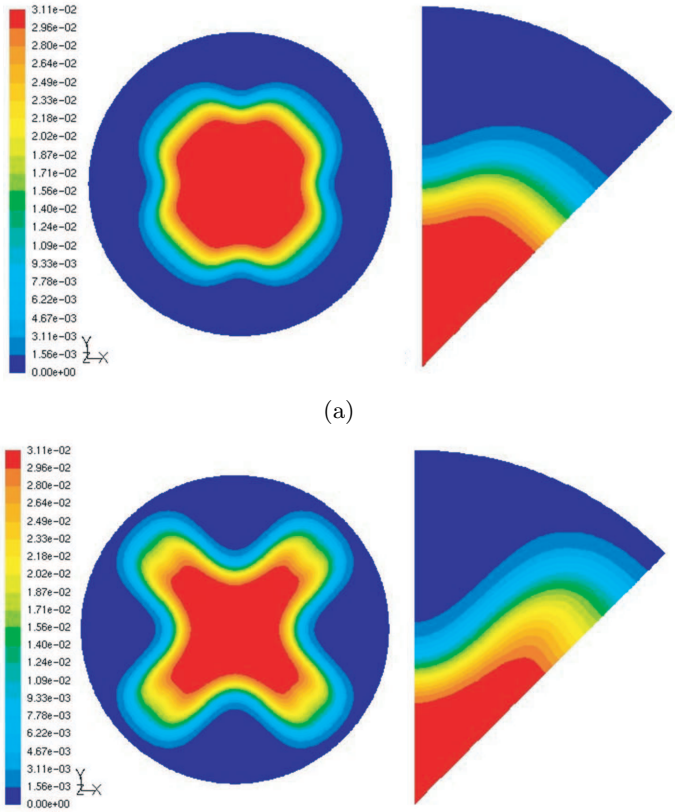

(a)

(b)

Figure 10. Propane mass fraction contours at $x/H = 2$ in round combustor for: (a) 91 m/s and (b) 227.5 m/s.

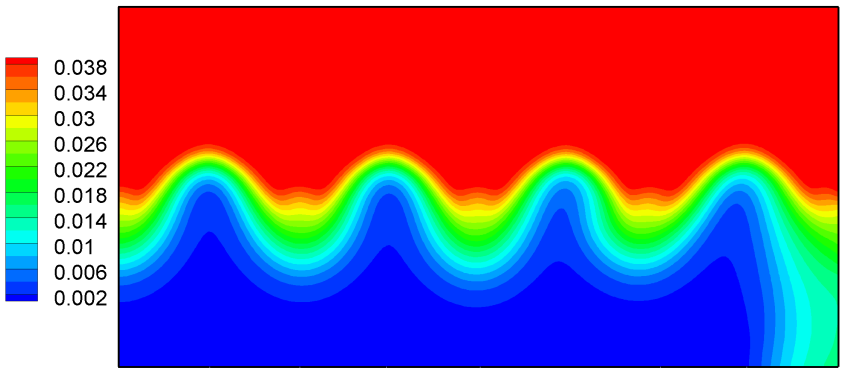

(a)

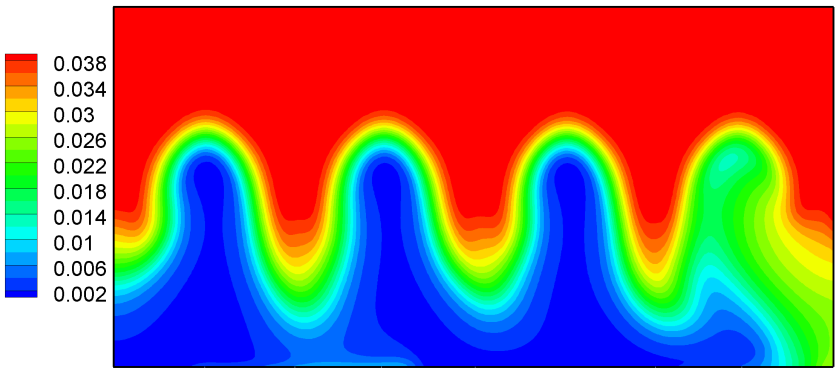

(b)

Figure 11. Propane mass fraction contours at $x/H = 1$ in planar combustor for: (a) 50 m/s and (b) 100 m/s.

2.3.4 Overall combustor performance

The purpose of this study is to control the shear layer in order to increase the heat release using microjets. The effects of microjets on primary flow inside the round and planar combustors were shown in sections 2.3.1, 2.3.2 and 2.3.3. Microjets were shown to change the flow structure, enhance mixing of the burnt and unburnt species, increase turbulent kinetic energy and increase the flame surface area. All these parameters lead to the evaluation of the overall combustor performance in the round and planar combustors.

2.3.4.1 Round combustor

12(a) shows the area weighted heat release rate along the length of the round combustor for different microjet velocities. The higher microjet velocity cases have higher heat release rates closer to the step. This is because of high turbulence in the microjet plane which results in higher reaction rates, as well as larger flame surface area as a result of large scale structures created by the microjets. The heat release rate for the 227.5 m/s case is less than that for the lower velocity cases downstream of $x/H = 12$ due to the less amount of fuel left for burning – a similar trend is observed for 182 m/s and 136.5 m/s cases downstream of $x/H = 10$ and $x/H = 8$, respectively. This is verified by inspecting the fuel mass flow rate at different axial planes along the length of the combustor in 12(b). It is important to note that a significant portion of the fuel leaves the combustor unburnt. At higher microjet velocities there is a lower amount of unburnt fuel leaving the combustor compared to the lower microjet velocity cases.

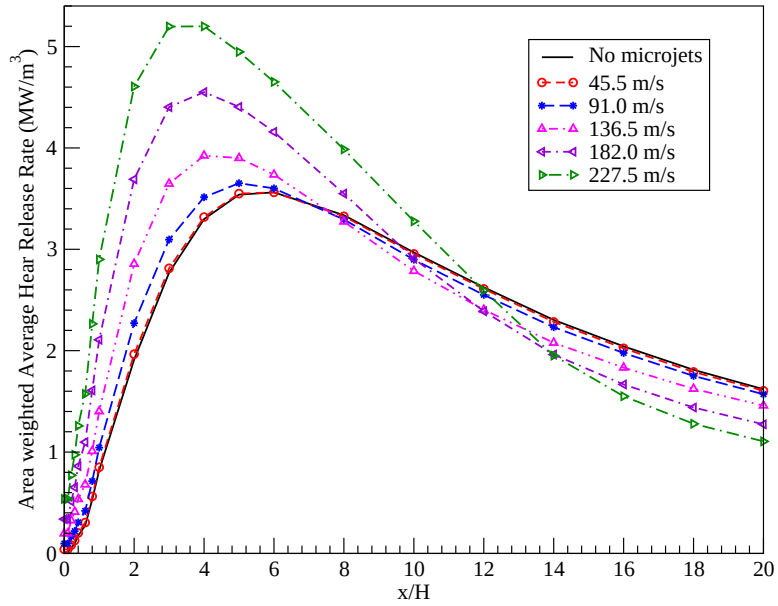

(a)

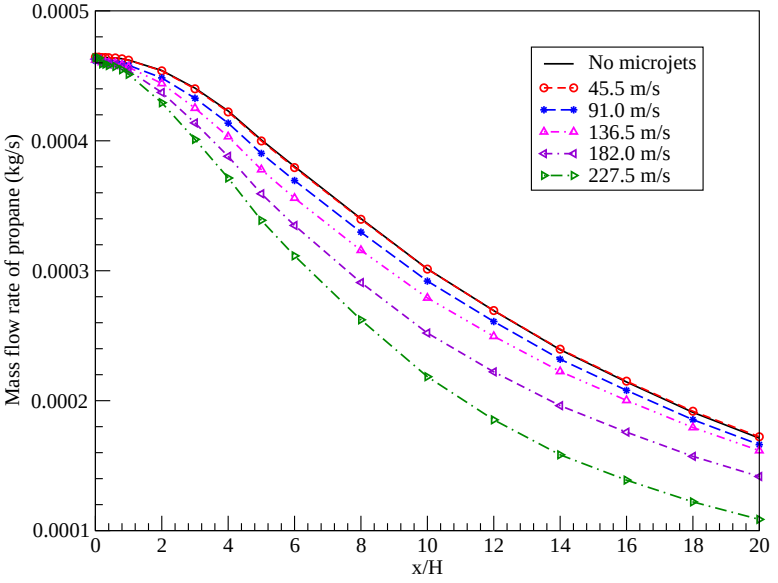

(b)

Figure 12. Variation of (a) area-weighted heat release rate and (b) mass flow rate of propane, along the length of the round combustor for different microjet velocities.

U_j (m/s)	Mass ratio (%)	Total volumetric heat release rate (MW/m^3) and % change	Avg. temperature at the exit (K) and % change
0 (axisym.)	—	2.472 (—)	1146 (—)
45.5	0.095	2.473 (0.05%)	1147 (0.08%)
91.0	0.190	2.497 (1.02%)	1154 (0.7%)
136.5	0.286	2.540 (2.8%)	1167 (1.8%)
182.0	0.381	2.726 (10.3%)	1202 (4.9%)
227.5	0.476	3.014 (21.9%)	1262 (10.1%)

TABLE II

SUMMARY OF TOTAL VOLUMETRIC HEAT RELEASE AND EXIT TEMPERATURE FOR ROUND COMBUSTOR.

Total volumetric heat release rate along with the averaged temperature at the combustor exit are important metrics for determining the overall effect of the microjets. Table II gives the values for the above quantities for different cases. The table also shows the percentage change in values compared to the baseline (no microjet) case. The data reiterate the point that the overall gain in energy conversion with microjets is marginal up to the microjet velocity of 136.5 m/s. However, for velocities 182 m/s and 227.5 m/s there is a significant increase in heat release. The volumetric heat release rate and average temperature appear to grow exponentially with increase in mass ratio. Furthermore, by designing combustors with microjets the length of the combustor can be shortened by $20\% - 40\%$, or the heat release rate can be increased by more than 25%. To summarize, we have demonstrated a significant improvement in combustor performance in terms of heat release rate and better fuel consumption by introducing four symmetrically placed microjets with an additional mass input of only 0.5% of the primary

flow. Nevertheless, as we discuss below, the effect of microjets on heat release is much more pronounced in the planar combustor.

2.3.4.2 Planar combustor

The average heat release rates along the length of the combustor for various microjet velocities are shown in Figure 13(a). Compared to the baseline case, the 50 m/s case has higher heat release closer to the step ($x/H < 3.5$), but the levels fall below the baseline case outside of this region. For low microjet speeds, the fuel does not mix with the products at a high rate beyond this region and is not able to energize the flame for increased burning. Ideally, high heat release values should exist throughout the combustor to maximize burning. The 75 m/s and 100 m/s cases have peak heat release rates at approximately $x/H = 2$ and $x/H = 1.5$, respectively. For the 75 m/s case, the heat release rate decreases in the regions $2 < x/H < 3.8$ and $x/H > 4.2$; however, between these two regions heat release rate is almost constant. The same trend of almost constant heat release rate is observed between $x/H = 5.5$ and $x/H = 6.5$ for 100 m/s case. This trend in heat release rate is a result of the secondary burning of the fuel in the planes between the microjets.

Figure 13(b) shows the mass flow rate of propane along the axial direction of the combustor for various microjet velocities. For the 25 m/s case, the species burning rate is similar to that in the baseline case because of the low levels of mixing generated by the microjets. The 50 m/s case has slightly better species burning rate compared to baseline case. However, the 75 m/s and 100 m/s cases have significantly high burning rates compared to the baseline case.

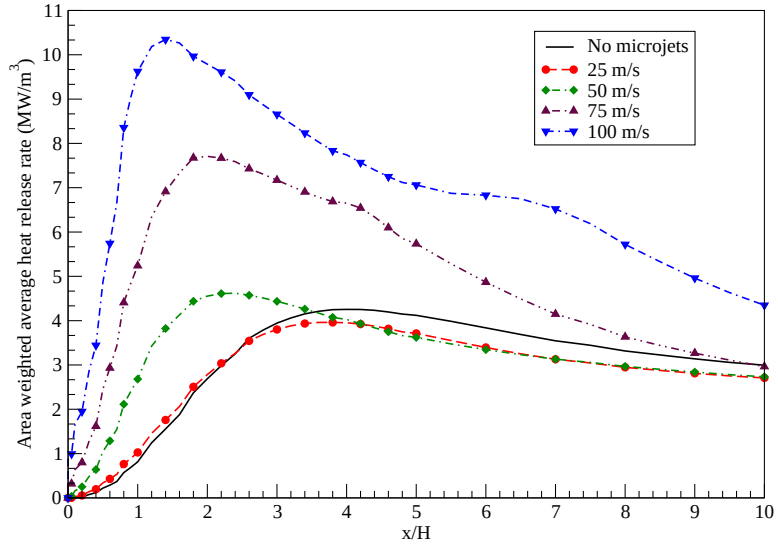

(a)

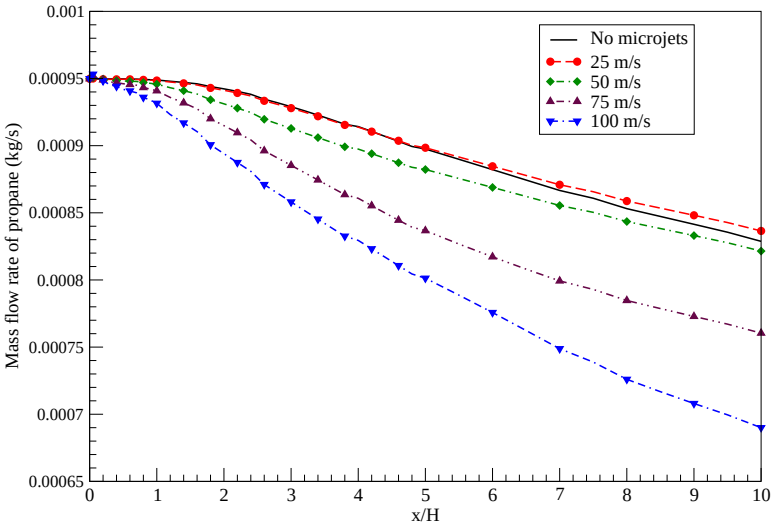

(b)

Figure 13. Variation of (a) area-weighted heat release rate and (b) mass flow rate of propane, along the length of the planar combustor for different microjet velocities.

The volumetric heat release and the average exit temperature for various microjet velocities are listed in Table III. For the 100 m/s case, the mass contribution of the four microjets is ~ 1% of the mass of the primary flow. In this case, the volumetric heat release rate increases by approximately 140% over that of the baseline case. At the combustor exit, the average temperatures for microjet speeds of 25 m/s and 50 m/s show slight decrease compared to the baseline case. These cases do not have a significant increase in heat release along the length of the combustor after the initial increase close to the step. The average exit temperature for these cases decreases due to heat transfer with the isothermal walls along the length of the combustor. For the 75 m/s and 100 m/s cases, the average exit temperature significantly increases because of the additional heat release along the length of the combustor as compared to the baseline combustor.

U_j (m/s)	Mass ratio (%)	Total volumetric heat release rate (MW/m^3) and % change	Avg. temperature at the exit (K) and % change
0 (base case)	—	2.752 (—)	683 (—)
25.0	0.26	2.965 (7.8%)	639 (-6.4%)
50.0	0.52	3.144 (14.2%)	676 (-1.0%)
75.0	0.78	4.776 (73.5%)	821 (20.2%)
100.0	1.04	6.615 (140.8%)	955 (39.8%)

TABLE III

SUMMARY OF TOTAL VOLUMETRIC HEAT RELEASE RATE AND EXIT TEMPERATURE FOR PLANAR COMBUSTOR.

The percentage increase in the heat release rate at highest microjet velocity, relative to the baseline case, is large in the planar combustor compared to the round combustor. This is because of the poor fuel burning efficiency of the planar combustor without microjets as compared to the round combustor without microjets. 13(b) shows that in the round combustor without microjets, approximately 37% of unburnt fuel leaves the combustor. While in the planar combustor without microjets, ~ 85% of the fuel remains unburnt. Adding microjets decreases the amount of unburnt fuel leaving the dump combustor. At the highest microjet velocity, ~ 23% of the unburnt fuel leaves the round combustor compared to ~ 73% in the planar combustor. In spite of the large heat release rate in the planar combustor, still the majority of the fuel exits the combustor without participating in chemical reaction. It is also worth mentioning that in terms of absolute changes, microjets appear to have similar level of efficiency in both combustors. Approximately 14% and 12% of the total incoming fuel is consumed additionally due to microjets in round and planar combustors, respectively.

2.4 Experimental validation

Considering the limitations of RANS, it is important to obtain some preliminary validations from experiments before we commit our efforts to more accurate, but expensive, LES investigation. We emphasize that the purpose of the comparison at this stage of our study is to primarily confirm the "trend" of drastic increase in heat release as predicted by our RANS simulations. We do not intend to conduct a point by point comparison with experiments here and postpone that comparison for our future LES results. We should also emphasize that there are several

differences between the conditions considered in the experiments and those in the simulations. This includes differences in fuel type and number of microjets.

The experiments were conducted by introducing 4 microjets of 1 mm diameter in the step of a planar dump combustor (22). It should be noted that the number of microjets used in the experiments is half the number of microjets used in the simulations. The combustor geometry for the experiment has the same step height as in the computational study, but different spanwise width (8H). The microjets were spaced 2H apart. The fuel used in the experiment was methane premixed with air at an equivalence ratio of 0.64 ± 0.02 and pure air entered through the microjets. The incoming velocity was 10 m/s and microjet velocities varied from 0 to 200 m/s. The planar facility was redesigned to accommodate microjets located in the center of the dump plane at 45^{o} to the reactant stream; the facility also allowed optical access through side and bottom walls. Microjets positioned at the lateral center of the dump plane and in the spanwise direction at y/H = -3, -1, 1, and 3, were supplied with compressed air. Microjet flow rates up to approximately 2.5% of the primary flow rate were investigated.

Heat release rate in the combustor was quantified using chemiluminescence. The results showed a nearly linear relationship between heat release and radiation emitted by C_2 radicals. Heat release rates are shown in Figure 14 normalized by the heat release measured for the baseline combustor. It is seen that the heat release rate increases monotonically with the increase of the microjet mass ratio. This trend was observed over the range of equivalence ratios studied, though only equivalence ratio of 0.64 is reported here. The significant increase

of heat release rate observed in the experiments is in good qualitative agreement with the predictions of RANS.

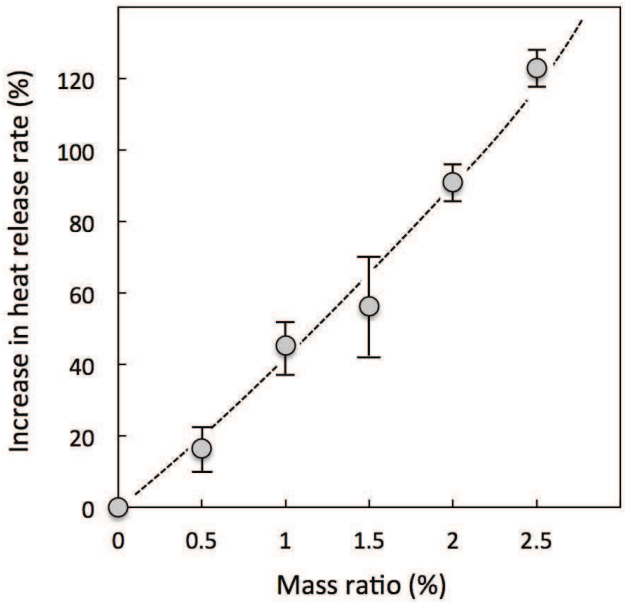

Figure 14. Experimentally measured heat release rate as a function of microjet mass flow rate in the round combustor.

2.5 Conclusions

This work investigates possible means to enhance the performance of dump combustors. The main focus is on the use of microjets in round and planar dump combustors. Previous studies have indicated that installing microjets before the step with a flow direction perpendicular to

the the direction of the main inlet flow leads to somewhat minimal gains. In this present study, microjets are placed inside the step with their axes aligned at 45^o angle with respect to the main flow direction. For this configuration, a significant (up to 140%) increase in heat release rate is observed for modest microjet flow rates of up to 1% of the main flow rate.

A careful examination of the results has identified three primary mechanisms responsible for the significant increase in the heat release rate when microjets are introduced. First, the strong shear introduced by the microjets generates high levels of turbulent kinetic energy, hence increasing the flame speed. This is accompanied by high-amplitude wrinkling of the surface of the flame around the locations where microjets impact the flame. As long as the strain rates around the microjets are not large enough to break up the flame, this wrinkling effect leads to an increase of the flame surface area. The third mechanism is a result of the interaction of the microjets with the wall of the combustor where strong return flows are formed. This significantly enhances the mixing of the reactants with the products, thus exposing the reactants to high temperatures that are essential for combustion. The third mechanism is much more effective in the planar combustor, explaining why the overall increase in heat release is substantially larger for this combustor as compared to that for the round combustor.

A finalized design for the implementation of microjets in planar dump combustor was provided to the experimental group for validation. Experimental results qualitatively confirm the increasing heat release trends observed in the simulations of planar combustor with microjets. With this qualitative validation, the next step is to perform LES on the final design of the com-

bustor to develop a more fundamental understanding of the flow dynamics. The LES results are closely validated with experiments at each step.

CHAPTER 3

NUMERICAL METHODOLOGY FOR LES STUDIES

3.1 Introduction

LES provides a more accurate representation of the turbulent flow field compared to RANS simulations, where all the turbulent scales are modeled. In LES, the large scale eddies that are affected by the geometry of the problem are resolved. Hence, LES is as accurate as DNS in resolving the large scales. However, the treatment of small scales varies in DNS and LES. The isotropic small scales are resolved in DNS and the grid requirement to resolve these small scales in the flow increases with Reynolds numbers. This imposes severe restrictions on the geometry and the Reynolds numbers that can be simulated. However, in LES the small scales are filtered and their effect is captured with a sub-grid scale model. Hence, LES is computationally less expensive compared to DNS and can be utilized for simulating complex geometries. This makes LES the perfect choice for simulating the effect of a microjet in a backward-facing step flow, where both the microjet flow and backward-facing step flow are turbulent in nature.

The objective of this chapter is to provide a brief description of the numerical approach utilized in this thesis for performing LES.

3.2 Legendre spectral element method

Numerical schemes can crucially affect the fidelity of LES. Numerical errors in space and time can smear the solutions, overly disperse the waves, and result in an inaccurate computation

of the turbulent flow. Among the errors related to the numerical scheme, the diffusion and dispersion errors have the most serious consequences on the accuracy of the solution. High-order methods, which have low dispersion and diffusive errors are therefore necessary for accurate and reliable simulations.

Spectral element methods (SEM), first introduced by Patera (23), offer several attractive features that make them excellent candidates for LES of practical flows. They combine the accuracy of the spectral schemes with the flexibility of the finite element method, thereby allowing high-order discretization of complex geometries. The spatial resolution can be conveniently altered either by increasing the number of elements (h-refinement) or by increasing the polynomial order within the elements (p-refinement). In smooth solution spaces, the method provides asymptotically exponential rate of spatial convergence with p-refinement. Low dispersion errors in these methods lead to high temporal accuracy, making them suitable for wave dominated, unsteady problems. Moreover, low degree of data connectivity between elements facilitates efficient parallel implementation.

Nek5000, the code based on Legendre spectral/hp element method, is developed by Fischer et al. (24). It solves the non-dimensional unsteady incompressible Navier-Stokes equations, subject to appropriate boundary conditions and initial conditions. The filtered incompressible Navier-Stokes equations solved are,

$$\frac{\partial \tilde{u}_i}{\partial x_i} = 0, \tag{3.1}$$

$$\frac{\partial \tilde{u}_i}{\partial t} + \tilde{u}_j \frac{\partial \tilde{u}_i}{\partial x_j} = -\frac{\partial \tilde{p}}{\partial x_i} + \frac{1}{Re} \frac{\partial^2 \tilde{u}_i}{\partial x_j^2} - \frac{\partial \tau_{ij}}{\partial x_j} \tag{3.2}$$

where the tilde sign is used to specify filtered quantities; $\tilde{u}_i$ and $\tilde{p}$ are the filtered velocity and pressure, respectively. In addition to the above equations, the filtered equation solved for the passive scalar (mass fraction, $\tilde{Y}$) is,

$$\frac{\partial \tilde{Y}}{\partial t} + \tilde{u}_j \frac{\partial \tilde{Y}}{\partial x_j} = \frac{1}{ReSc} \frac{\partial^2 \tilde{Y}}{\partial x_j^2} - \frac{\partial q_{j,Y}}{\partial x_j} \tag{3.3}$$

The non-dimensional numbers Re and Sc in Equation 3.2 and Equation 3.3 are the Reynolds number and Schmidt number, respectively. The term τ_{ij} and q_{ij} in Equation 3.2 and Equation 3.3, respectively, are the sub-grid stress terms that need to be modeled and are given by,

$$\tau_{ij} = \widetilde{u_i u_j} - \tilde{u}_i \tilde{u}_j \tag{3.4}$$

$$q_{j,Y} = \widetilde{u_j Y} - \tilde{u}_j \tilde{Y} \tag{3.5}$$

The filtered Navier-Stokes equations are discretized in time using the operation-integration-factor scheme (OIFS) developed by Maday et al. (25). This approach decouples the nonlinear convective term from the linear viscous term. The convective terms are treated explicitly and diffusion terms are treated implicitly using a second-order backward differentiation multistep

scheme. The advantage of this splitting approach is that a larger time step size ($\triangle t$) corresponding to convective Courant numbers of two to ten can be used for the LES simulations.

The spatial discretization in Nek5000 is based on spectral element method. The computational domain is represented as a set of (disjoint) macro-elements with the solution and geometry being approximated by higher-order polynomial expansions within each macro-element. Three-dimensional domains are broken up into hexahedral elements. Within each element, a local Cartesian mesh is constructed corresponding to a $(N+1) \times (N+1) \times (N+1)$ tensor-product Gauss-Lobatto Legendre (GLL) collocation points. The dependent variables are expanded in terms of N^{th}-order tensor-product (polynomial) Lagrangian interpolants through GLL collocation points. A more complete description of the method is provided in the book by Deville et al. (26).

3.3 LES methodology

Modeling of only the small scale flow physics as opposed to the entire spectrum of turbulence, as done in Reynolds averaged Navier-Stokes simulations, reduces the complexity of modeling in LES. The most common approach for modeling the sub-grid terms, to close the filterd Navier-Stokes equations, are Smagorinsky model and dynamic Smagorinsky model. In topologically complex flows, the computational overhead of the sub-grid model could be substantial to offset the gain in using a coarse resolution over direct numerical simulations. Further, stability constrains demand ad hoc averaging of the Smagorinsky constant along the homogenous directions in the dynamic procedure. For the above averaging, data has to be collected from multiple sub-domains spread over numerous processors, leading to large bandwith mes-

sage passing. This naturally leads to large computational overhead that substantially reduces parallel scale up efficiency of the LES code. Spectral element filtering strategies for LES was studied by Blackburn and Schmidt (27). They investigated three different filtering techniques within two-dimensional spectral elements for the simulation of incompressible turbulent channel flow with a dynamic sub-grid model. Fischer and Mullen (28) introduced a spectral element filtering technique to stabilize their direct numerical simulation. Levin et al. (29) applied a two-step filtering procedure to control the growth of non-linear instabilities in their eddy resolving spectral element ocean model. A combined spectral element-Fourier method was used by Karamanos (30) for LES with an explicit sub-grid model. Karamanos and Karniadakis (31) introduced spectral vanishing viscosity concept for LES. The implementation was tested for turbulent channel flow using Fourier discretization in the streamwise direction and spectral/hp quadrilateral elements in the cross flow and wall-normal directions.

Use of explicit filtering of the solution without any sub-grid modeling, has been proposed in (32; 33; 34; 35). The sub-grid dissipation is accomplished with the computational grid for LES. The grid acts as an implicit low-pass filter. Explicit filtering is performed to remove high wave number oscillations and smoothen the solution variables. This approach is employed in the present study. Sengupta (36) performed LES studies in a backward-facing step flow using a Discontinuous Spectral Element Method (DSEM) at $\mathtt{Re} = 5000$. In one of the studies, results from the dynamic Smagorinsky model were compared to those obtained from implicit LES (no sub-grid model). The results for averged streamwise velocity data and streamwise normal fluctuations data matched very well for the two approaches. The implicit LES approach was

found to be computationally less expensive compared to the sub-grid modeling approach. The idea of implicit LES is explored for the LES cases presented here.

Explicitly filtered ("no model") LES acts to control the numerical noise at the grid cut-off and creates an implicit sub-grid dissipation mechanism in the flow. The filter is designed to eliminate grid-to-grid oscillations without affecting the resolved scales. Interpolant-projection filtering procedure is used to filter the solution variables.

In Nek5000, the filter interpolation polynomial, ϕ_j, is constructed using the Legendre polynomial basis as given by Boyd (37). A discussion on the choice of the filter transfer functions is given in Mullen et al. (38). For smooth filtering of the low energy modes, a quadratic one-dimensional filter transfer function is constructed as,

$$d_\kappa = 1 - \alpha \left(\frac{\kappa}{\kappa_c}\right)^2, \quad \alpha = \begin{cases} 0.0 & \text{for } \alpha = \kappa < \kappa_c \\ 0.05 & \text{for } \alpha = \kappa \geqslant \kappa_c \end{cases} \tag{3.6}$$

Here, α is the filter weight, κ_c is the cut-off mode and d_κ is the unfiltered amount at mode κ. The filter weight determines the amount of energy to be removed from the mode $\kappa \geqslant \kappa_c$, at each time step. For the cases studied with Nek5000 in this work, $\kappa_c = N - 2$ is utilized for determining the filter interpolation polynomial.

CHAPTER 4

EFFECT OF TURBULENT INFLOW BOUNDARY CONDITION IN LES OF FLOW OVER A BACKWARD-FACING STEP

4.1 Introduction

The objective of this chapter is to validate the utilization of the implicit LES technique in Nek5000. The validation studies are performed in a backward-facing step geometry at Reynolds numbers 5000 and $28,000$, respectively. In addition to the validation studies, the effect of turbulent inflow boundary condition in LES of flow over a backward-facing step is analyzed at the two Reynolds numbers.

An important issue in the simulation of spatially developing flow with turbulent inflow boundary condition (where periodic boundary condition does not apply), is the prescription of inlet turbulence. Both experimental and numerical studies indicate a strong sensitivity of the results to the inlet turbulence. Many different approaches have been adopted, which can broadly be classified as deterministic and synthetic. In the deterministic approach, the data at the inlet is extracted directly from an auxiliary numerical simulation (39; 40) or from a plane downstream of the inlet as proposed by Lund et al. (41) as the rescaling/recycling method. This approach requires additional computing effort together with handling of huge amount of data and is not practical for arbitrarily complex configurations. Synthetic methods provide an

ideal approach for generating inflow turbulence by avoiding the complications of deterministic approach.

The simplest way to generate inflow turbulence is to superimpose random fluctuations with uniform distribution or white noise on the mean velocity profile. The time series generated by random numbers mainly consists of high-frequency components, which could be damped out by the numerical method when coarse grids are used in the vicinity of the inflow as is often the case. Moreover, the method does not account for any spatial or temporal correlation thereby having little resemblance to the actual physics of the flow. Stochastic techniques that try to mimic spatial and temporal correlations of real turbulence have met with reasonable success. The general approach is to produce inflow data that reproduce certain statistical properties of the flow such as the variance, cross correlations, higher-order moments, length and time scales, or energy spectra. Lee et al. (42) described a method based on stochastic fluctuation with a prescribed energy spectrum. However, their method was not readily applicable to simulation of backward-facing step (43). Some methods have drawn heavily from simulation techniques for correlated stochastic fields in structural analysis, e.g. the constant and weighted amplitude wave superposition spectral representation (44; 45; 46). Glaze and Frankel (47) proposed a version of the above technique for generating inlet condition in LES of turbulent jet. A digital filter based technique was developed by Klein et al. (48). A synthetic-eddy-method was proposed by Jarrin et al. (49) that is able to reproduce prescribed first and second order one-point statistics, characteristics length and time scales, and the shape of coherent structures.

This chapter utilizes a stochastic model for generating inflow turbulence for LES using a Legendre spectral element method. A comparison of the two methods of generating inflow turbulent boundary condition are analyzed, namely the stochastic model and the random method. The power spectra of the instantaneous velocity fluctuations generated by the two methods are analyzed and the effects of inflow boundary conditions on the flow are enumerated. In Section 4.2, we describe our numerical modeling approach and present the computational domain employed for the LES studies. This is followed by the description of the stochastic model of generating inflow turbulence in Section 4.3. In Section 4.4, the results are presented and discussed for $Re = 5000$ and $Re = 28,000$ cases. Finally, concluding remarks are provided in Section 5.7.

4.2 Numerical methodology and computational domain

The Nek5000 code is utilized for the LES studies. The filtered Navier-Stokes equations (Equation 3.1 and Equation 3.2) are solved utilizing the implicit LES technique discussed in 3.3.

The backward-facing step domain for LES studies is shown in Figure 15. The origin of the coordinate system is located at the base of the step. All variables are normalized by the step height (H) and mean inlet velocity (U_0). Reynolds numbers for the two LES cases, based on H and U_0, are 5000 and $28,000$. The dimensions of the computational domain for both the Reynolds numbers are given in Table IV, where L_i is the inlet section length; L_e is the post step expansion length; L_y is the wall normal length; L_z is the spanwise length; E is the number of spectral elements, and N is the polynomial order.

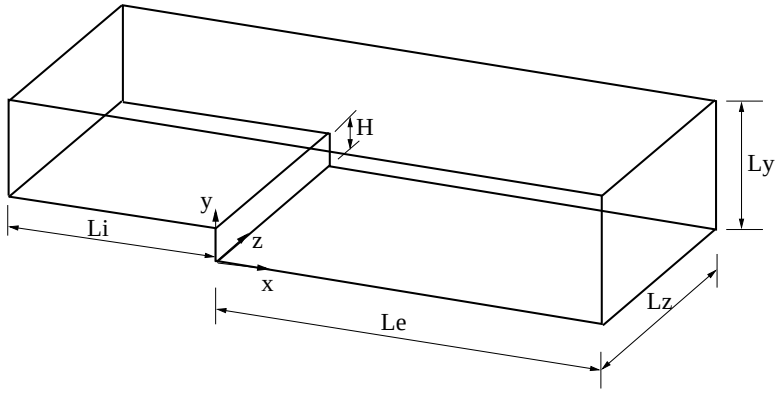

Figure 15. Schematic of backward-facing step geometry for LES studies at $Re = 5000$ and $Re = 28,000$.

Jovic and Driver (50) performed studies at $Re = 5000$ utilizing an open backward-facing step flow configuration. Later, Le et al. (43) and Akselvoll and Moin (51) performed DNS and LES, respectively, of the flow. The inflow has a fully developed flat plate boundary layer profile. The mean inflow velocity, $U(y)$, is obtained from Spalart's (52) boundary layer simulation at $Re_\theta = 670$, where θ is the momentum thickness. The boundary layer thickness is $\delta_{99} = 1.2H$. The simulation results for Nek5000 at $Re = 5000$ are compared with experimental results and DNS results. Akselvoll and Moin (51) investigated the $Re = 28,000$ case in their "high Reynolds number" study. The Nek5000 simulation results at $Re = 28,000$ are validated against the experimental data of Adams et al. (53).

For both Reynolds numbers, periodic boundary conditions are applied in the spanwise direction, no-slip condition is prescribed at the bottom wall and a zero-gradient boundary condition

is assigned at the outflow. However, the boundary condition prescribed at the top in the wall normal direction varies in the two cases and is shown in Table IV.

Re	Top boundary condition	L_i	L_e	L_y	L_z	E	N
5000	free-stream	10.0	20.0	6.0	4.0	980	7
28,000	no-slip wall	10.0	20.0	5.0	3.0	4116	7

TABLE IV

TOP BOUNDARY CONDITION, DIMENSIONS OF THE BACKWARD-FACING STEP GEOMETRY AND MESH SIZES FOR LES STUDIES.

4.3 Stochastic model for generating inlet turbulence

In this work, a stochastic model based on the original work of Gao and Mashayek (54) is utilized for generating inflow turbulence. In their paper, Gao and Mashayek utilized the stochastic model for predicting velocity and temperature fluctuations in Reynolds-averaged modeling of droplet-laden turbulent shear flows. Only a brief description of the method to generate a time series with given rms values and temporal correlation is provided here. A complete description of the stochastic model is provided in reference (54). Using the method

of time series analysis (55), the velocity fluctuations at time t is written in terms of the values at the previous time step, $t - \delta t$,

$$u_t = \beta_{uu} u_{t-\delta t} + \beta_{uv} v_{t-\delta t} + \beta_{uw} w_{t-\delta t} + d_{tu} \tag{4.1}$$

$$v_t = \beta_{vu} u_{t-\delta t} + \beta_{vv} v_{t-\delta t} + \beta_{vw} w_{t-\delta t} + d_{tv} \tag{4.2}$$

$$w_t = \beta_{wu} u_{t-\delta t} + \beta_{wv} v_{t-\delta t} + \beta_{ww} w_{t-\delta t} + d_{tw} \tag{4.3}$$

The above can be cast into matrix form,

$$\mathbf{A}_t = \boldsymbol{\beta} \cdot \mathbf{A}_{t-\delta t} + \mathbf{d}_t, \tag{4.4}$$

with

$$\mathbf{A}_t = \begin{pmatrix} u_t \\ v_t \\ w_t \end{pmatrix}, \ \boldsymbol{\beta} = \begin{pmatrix} \beta_{uu} & \beta_{uv} & \beta_{uw} \\ \beta_{vu} & \beta_{vv} & \beta_{vw} \\ \beta_{wu} & \beta_{wv} & \beta_{ww} \end{pmatrix}, \ \mathbf{d}_t = \begin{pmatrix} d_{tu} \\ d_{tv} \\ d_{tw} \end{pmatrix} \tag{4.5}$$

The main task is now to derive relations for $\boldsymbol{\beta}$ and $\mathbf{d}_t$. We multiply both sides of (Equation 4.4) by $\mathbf{A}^T_{t-\delta t}$ and take the expectation of the resulting equation which after some simple algebraic manipulation (see (54)) reduces to,

$$E[\mathbf{A}_t \cdot \mathbf{A}^T_{t-\delta t}] = \boldsymbol{\beta} \cdot cov(\mathbf{A}_{t-\delta t}, \mathbf{A}^T_{t-\delta t}), \tag{4.6}$$

where $E[\,]$ and $cov(\,)$ denotes the expectation (mean) and the covariance, respectively. The left-hand side can in fact be expressed in terms of a temporal correlation matrix,

$$\mathbf{C} = \begin{pmatrix} \overline{u_t u_{t-\delta t}} & \overline{u_t v_{t-\delta t}} & \overline{u_t w_{t-\delta t}} \\ \overline{v_t u_{t-\delta t}} & \overline{v_t v_{t-\delta t}} & \overline{v_t w_{t-\delta t}} \\ \overline{w_t u_{t-\delta t}} & \overline{w_t v_{t-\delta t}} & \overline{w_t w_{t-\delta t}} \end{pmatrix} \tag{4.7}$$

and when written in terms of correlation function $R_{\alpha\beta}(\delta t)$ is given by,

$$\mathbf{C} = \begin{pmatrix} R_{uu}\overline{u^2} & R_{uv}\sqrt{\overline{u^2}}\sqrt{\overline{v^2}} & R_{uw}\sqrt{\overline{u^2}}\sqrt{\overline{w^2}} \\ R_{vu}\sqrt{\overline{v^2}}\sqrt{\overline{u^2}} & R_{vv}\overline{v^2} & R_{vw}\sqrt{\overline{v^2}}\sqrt{\overline{w^2}} \\ R_{wu}\sqrt{\overline{w^2}}\sqrt{\overline{u^2}} & R_{wv}\sqrt{\overline{w^2}}\sqrt{\overline{v^2}} & R_{ww}\overline{w^2} \end{pmatrix} \tag{4.8}$$

where α and β represent the velocity fluctuations u, v and w and therefore $\boldsymbol{\beta}$ is given as,

$$\boldsymbol{\beta} = \mathbf{C} \cdot cov^{-1}(\mathbf{A}_{t-\delta t}, \mathbf{A}_{t-\delta t}^{T}) \tag{4.9}$$

To obtain $\mathbf{d}_t$, we write (Equation 4.4) as,

$$\mathbf{d}_t = \mathbf{A}_t - \boldsymbol{\beta} \cdot \mathbf{A}_{t-\delta t} \tag{4.10}$$

Multiplying both sides by their respective transpose and then taking the expectation, after simplification using (Equation 4.9), leads to

$$\mathrm{cov}(\mathbf{d}_t, \mathbf{d}_t^T) = \mathrm{cov}(\mathbf{A}_t, \mathbf{A}_t^T) - \boldsymbol{\beta} \cdot \mathbf{C}^T \tag{4.11}$$

Now, $\mathbf{d}_t$ can be written as,

$$\mathbf{d}_t = \mathbf{B} \cdot \mathbf{Z} \tag{4.12}$$

where $\mathbf{Z}$ is a random vector, each component of which is independent and sampled from a standard normal distribution with zero mean and unit variance. Multiplying both sides of (Equation 4.12) by their respective transpose and taking the expectations again leads to,

$$\mathbf{B} \cdot \mathbf{B}^T = \mathrm{cov}(\mathbf{d}_t, \mathbf{d}_t^T) \tag{4.13}$$

Matrix $\mathbf{B}$ can be determined by Cholesky factorization of symmetric, positive definite matrix $\mathrm{cov}(\mathbf{d}_t, \mathbf{d}_t^T)$. For implementing the model, temporal correlation functions for $R_{\alpha\beta}$ in (Equation 4.8) need to be specified. In this work we use the exponential form,

$$\mathbf{R}_{\alpha\beta} = \frac{\overline{\alpha_t \beta_{t-\delta t}}}{\sqrt{\overline{\alpha_t^2}}\sqrt{\overline{\beta_{t-\delta t}^2}}} \exp\left(\frac{-\delta t}{\mathbf{T}_{\alpha\beta}}\right) \tag{4.14}$$

where α and β represent the velocity fluctuations u, v and w; $\mathbf{T}_{\alpha\beta}$ is the integral time scale, and δt is the time step size. Due to symmetry, $\mathbf{T}_{\alpha\beta}$ has six components that need to be specified. As discussed in Gao and Mashayek (54), the normalized fluctuations are nearly isotropic so that the

off-diagonal terms of the Reynolds stress tensor can be neglected. This reduces (Equation 4.14) to only three components in the three directions, which are calculated by providing the integral time scales in each direction.

The input to the stochastic model for generating fluctuations are the velocity root-mean-squared (rms) profiles in the three directions and integral time scales in the three directions that are used to calculate the correlation functions $R_{\alpha\beta}$. For $Re = 5000$, rms profiles are obtained from Spalart's simulation (52). For $Re = 28,000$, the rms profiles are taken from Akselvoll and Moin (51). For both the cases, the values of integral time scales provided to the stochastic model are $T_{uu} = 1.08$, $T_{vv} = 0.394$ and $T_{ww} = 0.366$.

As an example, for $Re = 5000$ case, the input streamwise velocity rms data (u_{rms}) is provided in 16(a). For convenience, the u_{rms} values are shown for $y < 3.0$, because the u_{rms} values for $y > 3.0$ are same as that at $y = 3.0$. The stochastic model utilizes these input rms values to generate the streamwise fluctuations at each inlet point. These fluctuations are added to the mean streamwise velocity at each point to obtain the instantaneous streamwise velocity at the inlet. This procedure is repeated for all the velocity components.

The inlet power spectrum, $\mathbf{P}(f)$, of the steamwise velocity fluctuations at points $y = 1.06$ and $y = 2.0$ are shown in 16(b) and 16(c), respectively, at $x = -10.0$ and $z = 2.0$. The power spectrum of velocity fluctuations at a point are given by,

$$\mathbf{P}(f) = |\mathbf{U}(f)|^2 \tag{4.15}$$

where $U(f)$ are the coefficients of the Fourier transform of the velocity fluctuations data. The point $y = 1.06$ is in the boundary layer with maximum u_{rms} value and point $y = 2.0$ is at the outer edge of the boundary layer. The velocity fluctuations generated by the stochastic method are compared to those generated with the random method using the same inlet rms values. It should be noted that the random fluctuations required by both the methods have a standard normal distribution with zero mean and unit variance. We emphasize that using the standard normal distribution of random fluctuations is critical to correctly recover the input rms values at the end of the simulation.

The velocity fluctuations generated by the random method have uniform energy at all frequencies; however, the energy content of the velocity fluctuations is higher closer to the bottom wall ($y = 1.06$) as compared to those away from the wall ($y = 2.0$). The velocity fluctuations generated by the stochastic method have higher energy at low frequencies as compared to those at higher frequencies. Again, closer to the wall, $y = 1.06$, the energy content of the velocity fluctuations is higher compared to the points away from the wall. Near the wall, the rms values, which are input to the stochastic method, have higher values compared to those away from the wall. At low frequencies, the stochastic method generates fluctuations with higher energy at all points compared to the random method. However, at higher frequencies the random method results in higher energy compared to the stochastic method.

The stochastic model mimics the energy cascade of turbulence more closely as evident from the frequency content of the velocity fluctuations generated. Calculating the autocorrelation function of the signals generated at the inlet, is another way to determine whether the method

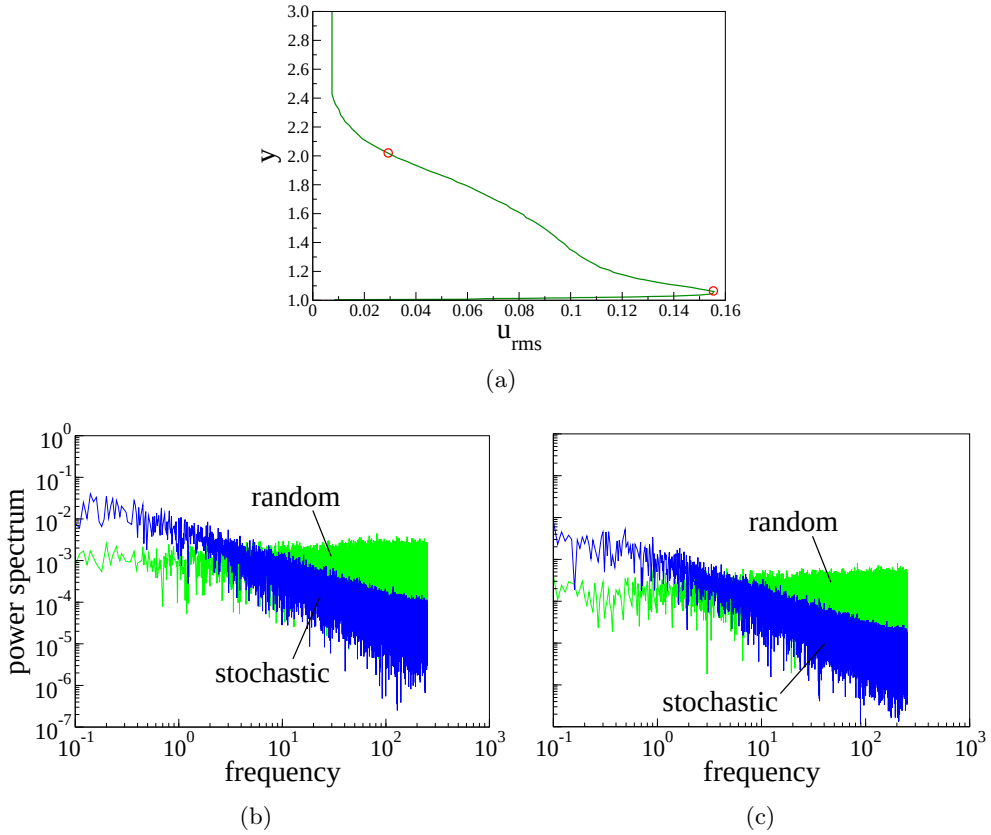

Figure 16. (a) Input u_{rms} data for $Re = 5000$, (b) power spectra comparison for fluctuations generated with the stochastic and random inflow boundary conditions at $x = -10.0, y = 1.06, z = 2.0$ and (c) power spectra comparison at $x = -10.0, y = 2.0, z = 2.0$.

used in generating inlet turbulence mimics real turbulence. Figure 17 compares the autocorrelation function of signals generated by the stochastic and the random methods, at point $y = 1.06$. The autocorrelation function, $R_h(\tau)$, is given by,

$$R_h(\tau) = \frac{\langle u(\tau)u(0)\rangle}{\langle u(0)^2\rangle}. \tag{4.16}$$

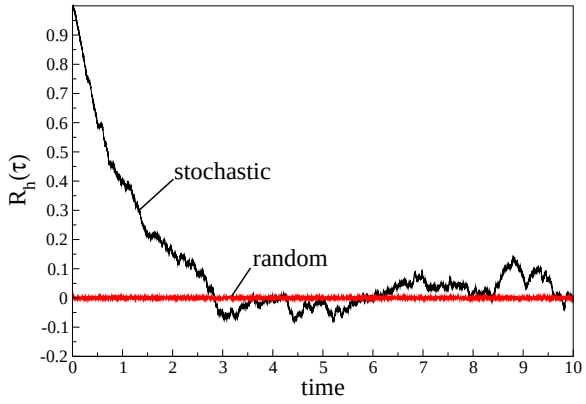

Figure 17. Autocorrelation function of velocity fluctuations for the stochastic and the random inflow boundary conditions.

The value of $R_h(\tau)$ is close to zero for velocity signals generated by the random method, hence the signals have zero correlation, as expected. The value of $R_h(\tau)$ for velocity signals generated with the stochastic method gradually decreases in time after starting from a perfect correlation at $\tau = 0.0$. In real turbulence, the velocity for a point at two different time realizations are correlated. Hence, instantaneous velocity signals generated with the stochastic method mimics real turbulence as compared to those generated with the random method.

The integral time scale in the streamwise direction can be obtained by integrating the autocorrelation function. For the stochastic model in Figure 17 the integral time scale is 1.072. This value is close to the value, $T_{uu} = 1.08$ provided as input to the model and is a validation of the model implementation.

4.4 Results and discussions

The effect of inflow boundary condition is studied in LES of flow over a backward facing step at $Re = 5000$ and $Re = 28,000$. The results obtained from the stochastic method of generating inflow turbulence are compared to those obtained from the random method of generating inflow turbulence. Since Nek5000 is a semi-implicit code and is stable at larger time step sizes, the LES cases were first simulated with a large time step size of $\triangle t = 0.01$.

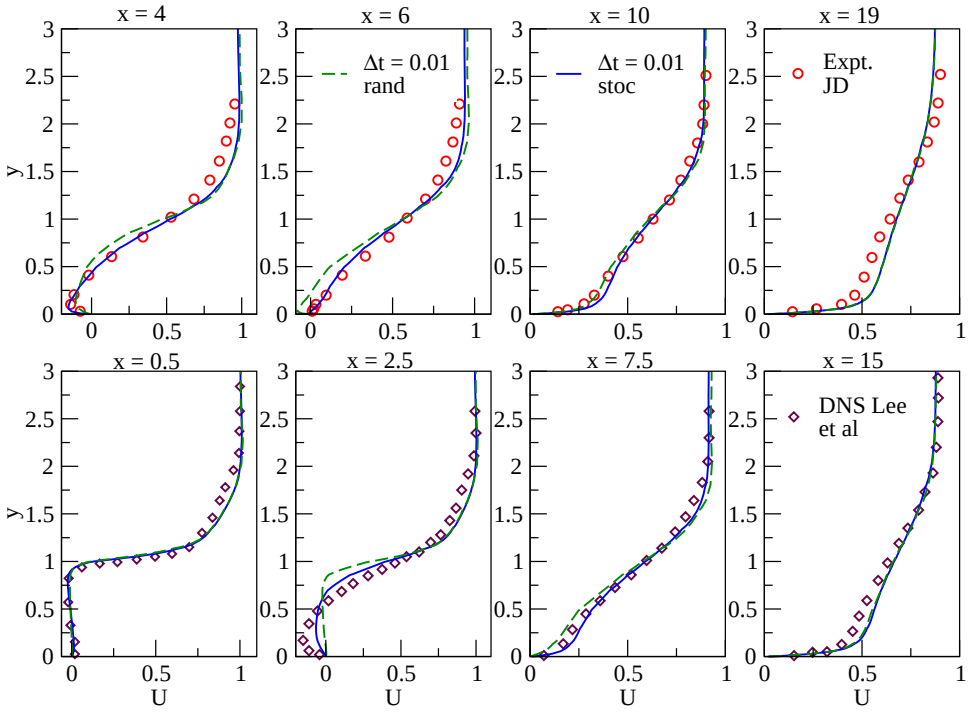

Figure 18. Comparison of the averaged streamwise velocity obtained from LES with stochastic and random methods at $\triangle t = 0.01$ for $Re = 5000$ with DNS and experimental data.

Figure 18 shows the averaged streamwise velocity comparisons of the results obtained by the stochastic and random inflow boundary conditions at $Re = 5000$. The data obtained with the stochastic method (designated by "$\triangle t = 0.01$ stoc") show a good agreement with the experimental data and the DNS results downstream of $x = 4.0$. In the recovery region, results are over-predicted at $x = 15.0$ compared to the DNS results, and at $x = 19.0$ compared to the experimental results. At $x = 2.5$, the stochastic and random methods both fail to predict the transition to turbulence. Below the shear layer ($y = 1.0$), the data from the random method (designated by "$\triangle t = 0.01$ rand") is under predicted at $x = 4.0$ and $x = 6.0$. Downstream of $x = 7.5$ both methods give similar results. The computed average reattachment length (X_r) for the case with stochastic inflow boundary condition is 6.34. The reported value of X_r from the experiment and the DNS is 6.1 and 6.28, respectively. The stochastic model over-predicts the value of X_r by about 4% compared to the experimental value and about 1% compared to the DNS value. The random method of generating inflow boundary condition predicts an average reattachment length of $X_r = 7.35$. This value is overpredicted by about 20.5% compared to the experimental value of X_r and about 17% compared to the DNS value of X_r.

Figure 19 compares the averaged streamwise velocity profile for the two inflow boundary conditions with experimental data at $Re = 28,000$. It is observed that imposing random fluctuations (designated by "random") to generate inflow turbulence results in averaged streamwise velocity values similar to those obtained with the stochastic model (designated by "stochastic") at all streamwise locations, except in the reattachment region. The computed average reattachment length (X_r) with the random inflow boundary condition is 6.49 and with the

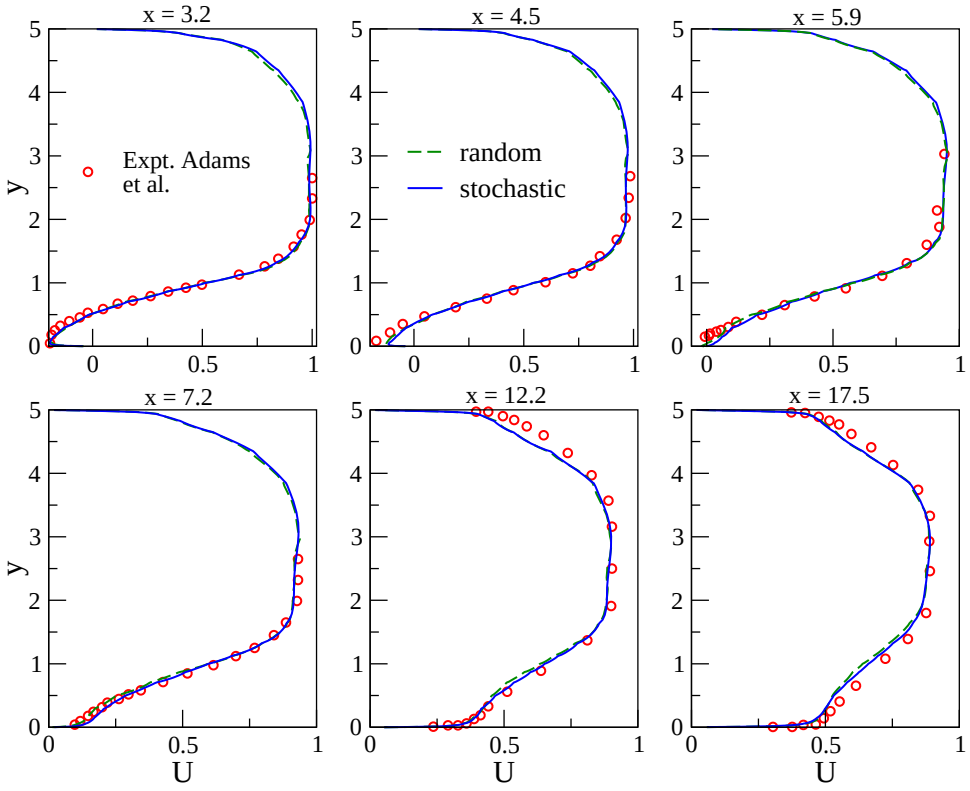

Figure 19. Comparison of the averaged streamwise velocities obtained using random and stochastic inflow boundary conditions at $\mathrm{Re} = 28,000$.

stochastic method is 5.89. The computed value of X_r with the random inflow boundary condition compares well with the experimental value of 6.7. In the recirculation zone at $x = 4.5$, the values are under-predicted by both methods of generating inflow turbulence. For the case with stochastic inflow boundary condition the values are under-predicted around the reattachment region ($x = 5.9$). At $x = 7.2$, the values obtained from the stochastic method under predict the experimental data closer to the bottom wall and the data from the random method provide better comparison with the experimental data. In the recovery region, $x = 12.2$ and 17.5,

the prediction is accurate with both the methods of generating inflow boundary conditions. To improve the prediction in the reattachment zone, a study with smaller time step size (not shown) was conducted. However, this did not change the prediction of the averaged streamwise velocity.

To summarize, with time step size of $\triangle t = 0.01$, the stochastic and random methods for generating inflow turbulence provide similar results at $Re = 28,000$. However, the two methods fail to provide the right predictions at $Re = 5000$. Further studies were performed at $Re = 5000$ to investigate the transition to turbulence. It was observed that time step size affects the transition to turbulence; hence, we first tackle the issue of time step size at $Re = 5000$. The analysis of the effect of the inflow boundary condition at the two Reynolds numbers is left till the end of this section.

4.4.1 Effect of time step size at Re = 5000

Before turning our attention to the time step size, grid resolution studies were conducted with Nek5000 at $\triangle t = 0.01$ to investigate transition to turbulence close to the step ($x = 2.5$). Simulations were performed with more grid points in three regions that affect the flow; the boundary layer in the inlet channel section, bottom wall in the post-expansion section, and the shear layer. Increasing the grid resolution in these regions did not help to predict the transition correctly. A time order accuracy study was conducted by simulating a case with lower order time scheme. However, this case provided the same results as observed in Figure 18. A filter strength (α) study was conducted to check for over-filtering or under-filtering of the solution variables. However, the study could not predict the data at $x = 2.5$. The random method

of generating inflow turbulence failed to predict the transition to turbulence as well; hence, all studies were performed with the stochastic method of generating inflow turbulence. These various studies performed to correctly predict the transition to turbulence are only mentioned here and not discussed.

A simulation was conducted with smaller time step size of $\triangle t = 0.002$, as part of the study to correctly predict the transition to turbulence. From 20(a), the plot for the averaged streamwise velocity at $x = 2.5$, it can be observed that the stochastic method with $\triangle t = 0.002$ correctly predicts the DNS data compared to the large time step size. The computed average reattachment length (X_r) for the case with $\triangle t = 0.002$ is 6.07 and the case with $\triangle t = 0.01$ is 6.34. The value of X_r for smaller time step size varies from the experimental value of 6.1 by about 0.5% and DNS value of 6.28 by about 3.3%. To ensure that the predictions obtained with $\triangle t = 0.002$ are reproducible, a time order accuracy study was conducted (not shown) that provided similar results to those obtained in Figure 21. Hence, the stochastic method with the smaller time step size of $\triangle t = 0.002$ predicts the transition to turbulence accurately and provides more accurate results for X_r as compared to the case simulated with the larger time step size of $\triangle t = 0.01$.

Use of large time step sizes implies that the small scales are not captured accurately, which can corrupt the solution. At low Reynolds numbers, the separation between large and small scales is smaller compared to that at higher Reynolds numbers. Therefore, the contribution from the diffusion term becomes significant at low Reynolds numbers. These results suggest that, although Nek5000 is stable for a larger time step size, to capture the small scales a smaller

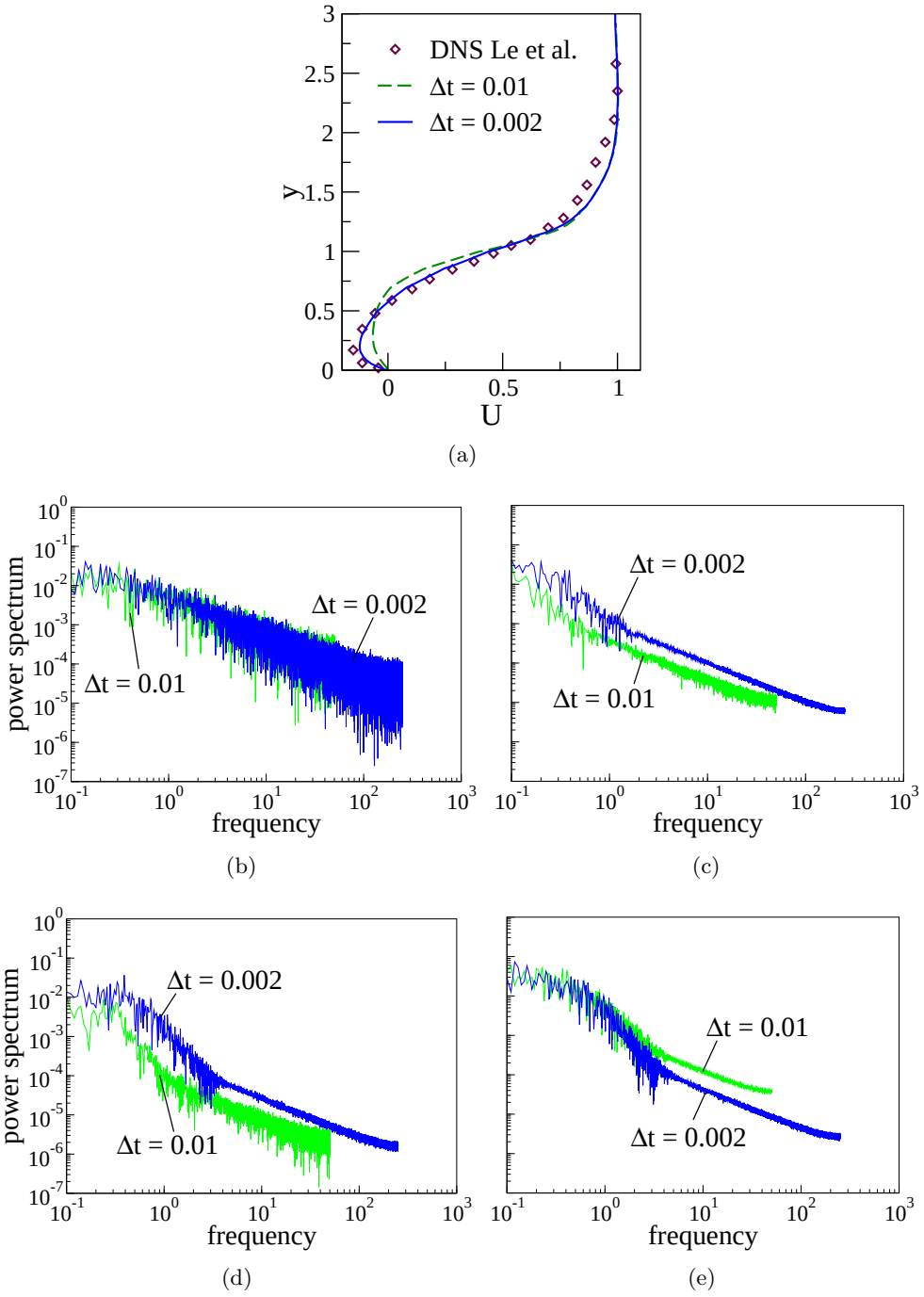

Figure 20. Comparison between two cases with different time step sizes, $\triangle t = 0.01$, and $\triangle t = 0.002$ using the stochastic method: (a) average streamwise velocity profile at $x = 2.5$, (b) power spectra comparison at the inlet point $x = -10.0, y = 1.06, z = 2.0$ near the bottom wall, (c) power spectra comparison at point $x = 0.0, y = 1.06, z = 2.0$ at the step, (d) power spectra comparison at a point in the shear layer $x = 0.5, y = 1.0, z = 2.0$, (e) power spectra comparison at $x = 4.0, y = 1.0, z = 2.0$.

time step size may be required. A similar effect of time step size in DNS of turbulent channel flow using an implicit time stepping was observed by Choi and Moin (56). Their study showed that very large time step sizes cause the turbulence to decay to a laminar state.

Power spectra analysis at various points in the flow domain provides a better understanding of the flow dynamics for the two time step sizes. 20(b) and 20(c) compare the power spectra of velocity fluctuations obtained from the cases with two different time step sizes at point $y = 1.06$ at the inlet ($x = -10.0$) and the step ($x = 0.0$), respectively. At the inlet, the energy content of velocity signals obtained from the two time step sizes are similar. However, at the step the $\triangle t = 0.01$ case has lower energy at all frequencies compared to the $\triangle t = 0.002$ case. 20(d) and 20(e) compare the power spectra of velocity signals obtained from the simulations using the two different time step sizes at points $x = 0.5$ and $x = 4.0$, respectively, in the shear layer ($y = 1.0$). At low frequencies, close to the step ($x = 0.5$), the energy content of the velocity signals at larger time step size of $\triangle t = 0.01$ is lower than the energy content of the velocity signals at smaller time step size of $\triangle t = 0.002$. However, downstream of the step, instabilities in the shear layer increase the energy content of the velocity signals at the larger time step size and it becomes similar to the energy content of the velocity signals at the smaller time step size. Hence, downstream of $x = 4.0$, the two time step sizes give similar results for the averaged streamwise velocity as observed in the plots shown in Figure 18 and Figure 21 for $\triangle t = 0.01$ (designated by "$\triangle t = 0.01$ stoc") and $\triangle t = 0.002$ (designated by "$\triangle t = 0.002$ stoc"), respectively. Therefore, at smaller time step size the boundary layer at the step has more energy and predicts the transition to turbulence accurately. For larger time step size, the

boundary layer is not fully turbulent and this leads to a delayed transition to turbulence in the recirculation zone. This shows that there is re-laminarization of the flow in the inlet channel at larger time step sizes.

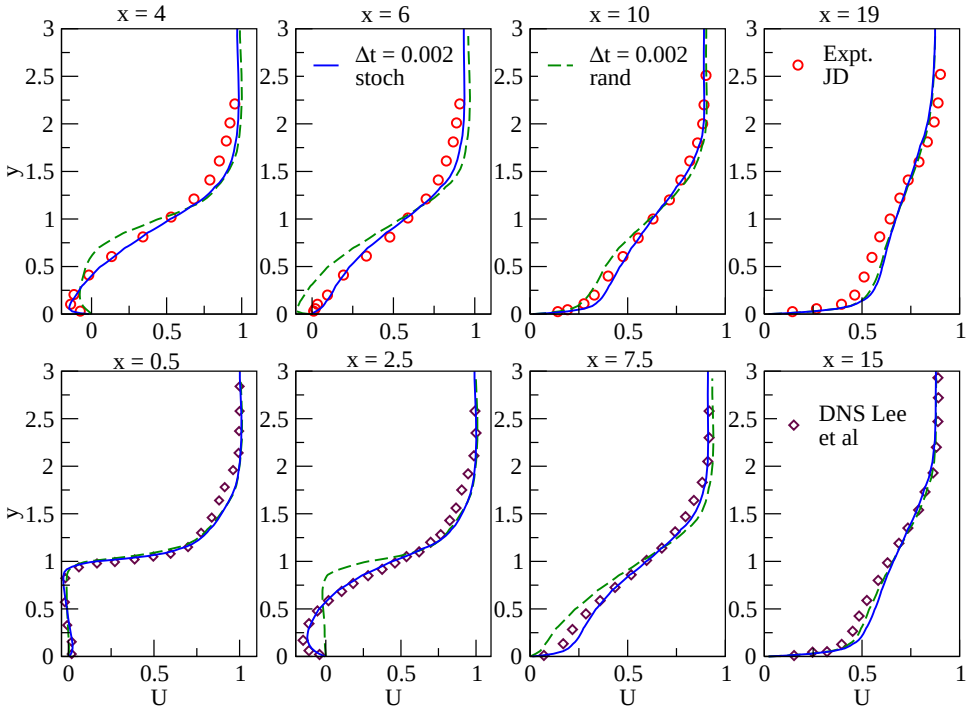

Figure 21. Comparison of the averaged streamwise velocity obtained from the stochastic and random methods at $\triangle t = 0.002$ for $Re = 5000$ with DNS and experimental data.

The above analysis suggests that the long length of the inlet channel, $L_i = 10.0$, leads to laminarization of the flow at larger time step size. Hence, we hypothesize that by reducing

the length of the inlet channel the transition to turbulence should be predicted accurately. To this end, a case with short inlet channel (designated by $\triangle t = 0.01$-SHIL) is simulated with an inlet channel length of $L_i = 1.0$, $E = 608$, $N = 7$ and $\triangle t = 0.01$ with stochastic inflow boundary condition. 22(a) and 22(b) shows the comparison of the power spectra of the velocity fluctuations generated at $x = 1.0$ and $x = 4.0$, respectively, in the shear layer ($y = 1.0$) for the short inlet channel case. At both the points the energy content of the velocity signals for $\triangle t = 0.01$-SHIL case are similar to the energy content of the velocity signals for the $\triangle t = 0.002$ case with long inlet channel. The use of a short inlet channel ($L_i = 1.0$) prevents the decay of the turbulence energy which was observed in the long inlet channel case ($L_i = 10.0$) at the larger time step size of $\triangle t = 0.01$. Hence, the boundary layer at the step remains turbulent for the case with shorter inlet channel and larger time step size. 22(c) shows the comparison of the average streamwise velocity at $x = 2.5$, showing good agreement between the two cases. The predicted average reattachment length is $X_r = 5.8$ which varies by less than 5% compared to the experimental value of X_r. The remaining locations are not shown because the results are similar to those in Figure 21.

By reducing the inlet channel length, the transition to turbulence is predicted accurately. This reiterates the point that the long inlet channel caused the laminarization of the flow at the step. This short inlet channel also reduces the computational time required for the simulations. Hence, with a stochastic method that mimics real turbulence more closely a short inlet channel and larger time step size can be utilized for LES.

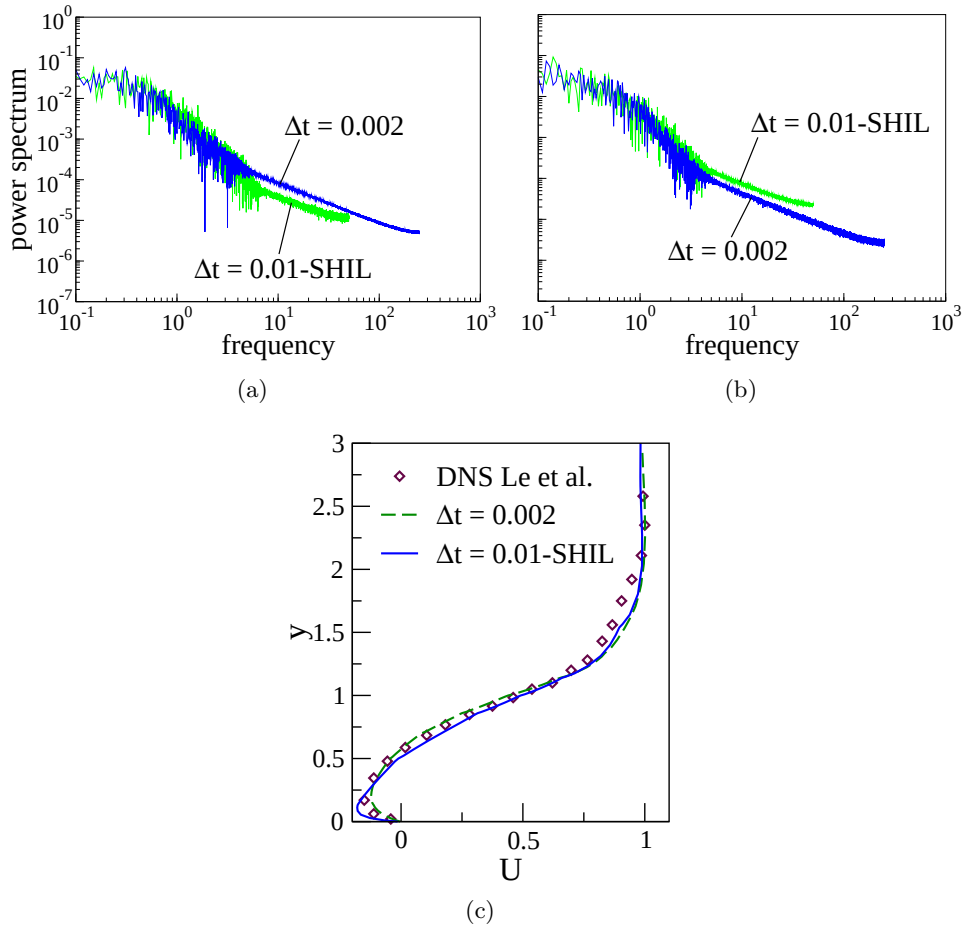

Figure 22. Comparison between short inlet channel case, $\triangle t = 0.01$-SHIL, and $\triangle t = 0.002$ with long inlet channel case: (a) power spectra comparison at a point in the shear layer $x = 1.0, y = 1.0, z = 2.0$, (b) power spectra comparison at $x = 4.0, y = 1.0, z = 2.0$, (c) average streamwise velocity at $x = 2.5$.

4.4.2 Effect of inflow boundary condition

The study of the effect of time step size showed that a stochastic method for generating the inflow boundary condition is needed to predict transition to turbulence at $\triangle t = 0.002$. To compare the two methods of generating inflow turbulence, simulations were performed with $\triangle t = 0.002$ and inflow turbulence generated using the random method at $Re = 5000$. Figure 21 shows the average streamwise velocity comparison of the two methods of generating inlet turbulence at various streamwise locations. The random method (designated by "$\triangle t = 0.002$ rand") does not predict the transition to turbulence at $x = 2.5$, while the stochastic model predicts the transition to turbulence accurately. In case of the random method, the transition to turbulence is delayed as observed from the streamwise velocity data at $x = 4.0$ and $x = 6.0$. The computed average reattachment length for the case with random inflow boundary condition is 7.48, which is over-predicted by about 22.6% compared to the experimental value and about 19.1% compared to the DNS value. The stochastic method predicts the experimental data accurately and compares well with the DNS data.

The power spectra comparison of velocity fluctuations obtained from the simulations using the stochastic and random inflow boundary conditions at point $y = 1.06$ are shown in Figure 23. The comparison is shown at the inlet ($x = -10.0$) and the step ($x = 0.0$). The energy content of the velocity signals generated by the stochastic method stays similar at the inlet and the step. This leads to a turbulent boundary layer which correctly predicts the data at $x = 2.5$.

The random method distributes more energy to higher frequencies which dissipate very quickly. The fluctuations generated with the random method are dissipated downstream of

the inlet and this leads to laminarization of the flow in the inlet channel section. A longer inlet channel is required for the case with random inflow boundary condition to develop real turbulence. Hence, the transition to turbulence is delayed in the case of random inflow boundary condition because of the lower energy at low frequencies compared to the stochastic method.

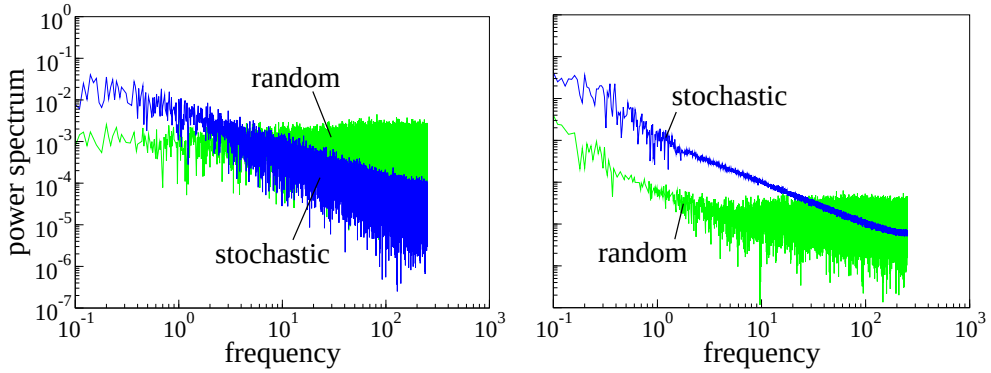

Figure 23. Power spectra comparison of instantaneous velocity signals generated at $Re = 5000$ by the stochastic and random inflow boundary conditions for $y = 1.06, z = 2.0$ at: (a) inlet ($x = -10.0$) and (b) step ($x = 0.0$).

A power spectra comparison of the velocity fluctuations obtained from the simulations with the two different inflow boundary conditions is shown in Figure 24. The comparison is made at points in the shear layer ($y = 1.0$) along the streamwise direction. Close to the step ($x =$

1.0), the velocity fluctuations obatained from the case with random inflow boundary condition has lower energy at low frequencies compared to the velocity fluctuations from the case with stochastic inflow boundary condition. Away from the step, the instabilities in the shear layer increase the energy content of the velocity fluctuations in the case of random inflow boundary condition. At $x = 2.0$ and downstream, the energy content of the velocity fluctuations obtained from the cases with two different inflow boundary conditions are similar at low frequencies.

In the case with random inflow boundary condition, energy is still distributed to higher frequencies at $x = 4.0$, in the shear layer. The energies at high frequencies do not dissipate and take the form of real turbulence as observed in the case with stochastic inflow boundary condition. The use of a longer inlet channel may facilitate the dissipation of energy at high frequencies in the case with random inflow boundary condition. However, the inflow turbulence generated with the stochastic method successfully predicts the transition to turbulence because it closely mimics the real turbulence at the inlet. Hence, at $Re = 5000$, the stochastic method is needed for generating the inflow turbulence.

In the case of $Re = 28,000$, both methods provide similar values for averaged streamwise velocity as observed in Figure 19. This suggests that LES of flow over a backward-facing step at high Reynolds numbers is not sensitive to the method of generating the inflow boundary condition.

At high Reynolds numbers there is a larger cascade of turbulent eddies compared to that at low Reynolds numbers. The large scale coherent structures exist at low frequencies while the small scale structures exist at high frequencies. In LES of these high Reynolds number flows,

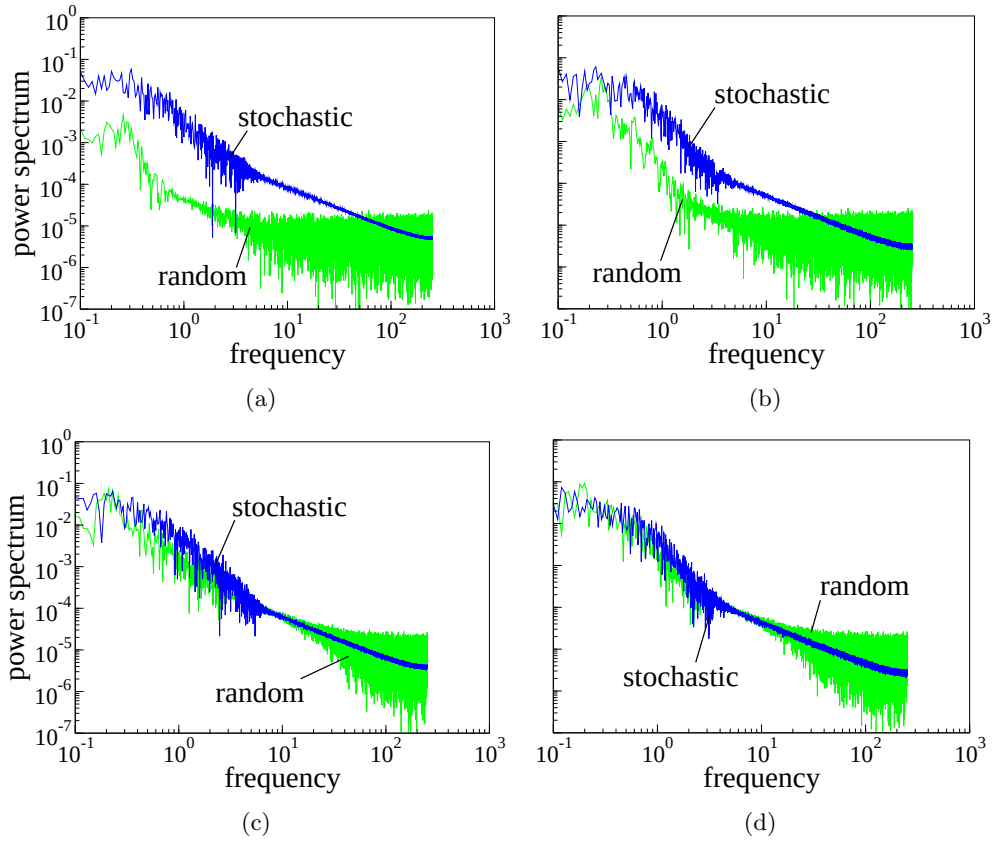

Figure 24. Power spectra comparison of instantaneous velocity fluctuations generated at $Re = 5000$ by the stochastic and random inflow boundary conditions at points in the shear layer ($y = 1.0, z = 2.0$): (a) $x = 1.0$, (b) $x = 2.0$, (c) $x = 3.0$ and (d) $x = 4.0$.

small scales where viscous forces are dominant are filtered and the inertial effects of large scales are captured.

Frequency analysis of the velocity fluctuations obtained from the simulations with the stochastic and random inflow boundary conditions at a point near the wall ($y = 1.01$) for

$Re = 28,000$ are shown in 25(a) and 25(b), at the inlet and the step, respectively. As in the case for $Re = 5000$, the stochastic inflow boundary condition mimics real turbulence at the inlet and the random boundary condition has uniform energy spread over all the frequencies. However, at the step at low frequencies, the energy content of velocity fluctuations for the case with random inflow boundary condition start mimicking real turbulence similar to the stochastic method.

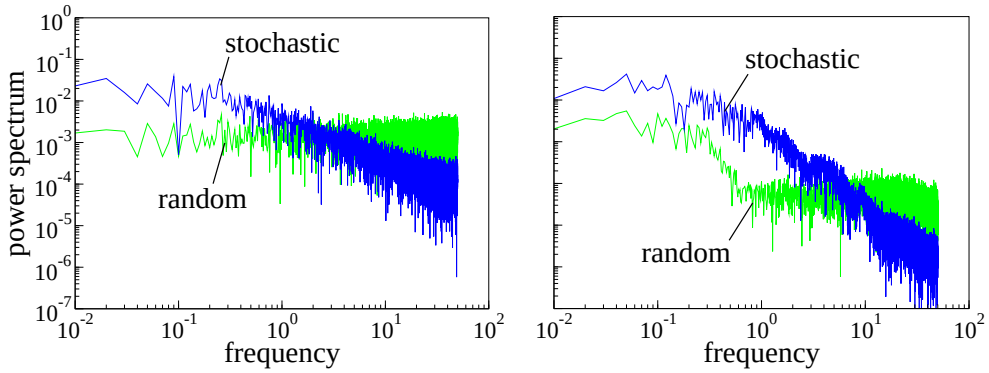

(a) (b)

Figure 25. Power spectra comparison of signals generated at $Re = 28,000$ by stochastic and random inflow boundary conditions for point $(y = 1.01, z = 1.5)$ at: (a) inlet $(x = -10.0)$ and (b) step $(x = 0.0)$.

In the case with random inflow boundary condition, a laminarization of the flow in the inlet channel was observed at $Re = 5000$; while, this effect is absent at $Re = 28,000$. In LES of low

Reynolds number flows, the energy distributed at high frequencies is captured, which causes laminarization of the flow in the inlet channel (23(b)) and hence a delay in the transition to turbulence. However, in LES of high Reynolds number flows the energy at high frequencies is filtered which triggers an earlier transition to turbulence. This leads to the energy content of velocity fluctuations obtained from the two methods of generating inflow boundary condition to have similar energies at the step (25(b)) at low frequencies. Therefore, at $Re = 28,000$, the boundary layer remains turbulent for both methods of generating inflow turbulence.

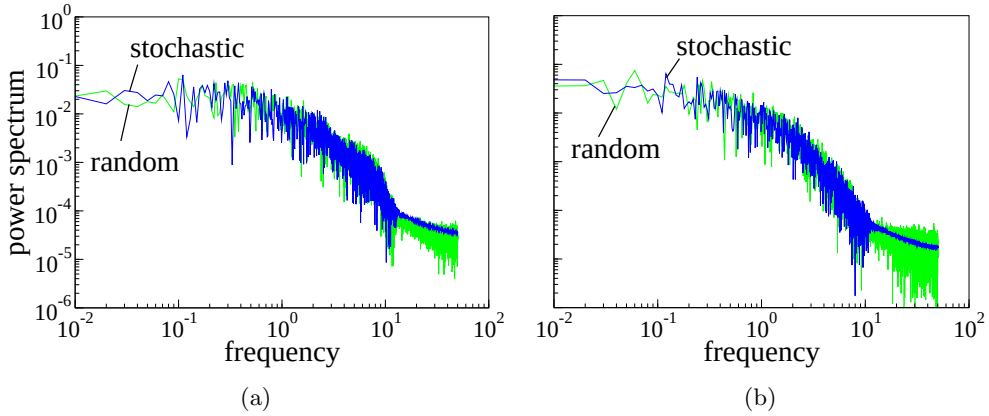

Figure 26. Power spectra comparison of instantaneous velocity signals obtained from stochastic and random inflow boundary conditions at $Re = 28,000$ for two points in the shear layer ($y = 1.0, z = 2.0$): (a) $x = 2.0$ and (b) $x = 4.0$.

A turbulent boundary layer affects the transition to turbulence in the shear layer. From figure Figure 26, it can be observed that the energy content of the velocity fluctuations obtained from the cases with two different inflow boundary conditions are very similar at the two different streamwise points in the shear layer. Hence, at high Reynolds numbers both the methods of generating inflow turbulence, stochastic and random, provide the correct predictions compared to the experimental data.

4.5 Conclusions

The LES studies presented in this paper analyze the effect of turbulent inflow boundary condition in flow over a backward-facing step at two different Reynolds numbers of 5000 and $28,000$. A stochastic model for generating inflow turbulence is implemented and results obtained with this model are compared to the results obtained with the random method. An implicit LES with no sub-grid model is utilized for LES studies in the Legendre spectral element method (Nek5000).

Nek5000 results with implicit LES for averaged streamwise velocity compare well with the experimental data and DNS data. Hence, explicit filtering is a viable choice for sub-grid dissipation mechanism in LES studies using spectral element method.

At $Re = 5000$, Nek5000 requires smaller time step size to accurately capture the transition to turbulence. Frequency analysis of the signals at the inlet and at the step show that at larger time step size the energy content of velocity fluctuations in the boundary layer of the inlet channel is lower compared to that in the case with the smaller time step size. However, a case with a small inlet channel and a larger time step size provides the correct results. At

$Re = 28,000$, larger time step sizes can be utilized for accurately capturing the recirculation zone.

At low Reynolds number ($Re = 5000$), the prescription of a turbulent inflow boundary condition that mimics real turbulence is critical for accurate prediction of transition to turbulence. The stochastic model, that mimics real turbulence, is successful in predicting the transition to turbulence, while the random method does not predict the transition to turbulence accurately. The transition to turbulence is delayed in case of the random method. Frequency analysis at several points in the boundary layer shows that having an inlet turbulent boundary layer with correlated components is critical at low Reynolds numbers. However, at high Reynolds number ($Re = 28,000$), the method used to generate inflow turbulence is not critical as the stochastic and random methods of generating inflow turbulence give similar results for averaged streamwise velocity at different streamwise locations, except in the reattachment region where the random method provides better prediction of the reattachment length.

CHAPTER 5

LES STUDIES OF SINGLE MICROJET IN A BACKWARD-FACING STEP FLOW

5.1 Introduction

The objective of this chapter is to utilize the validated implicit LES technique to perform LES studies in a planar dump combustor with microjets. This LES study to capture the dynamics of the interaction between the microjet and the primary shear layer in a backward-facing step geometry is the first of its kind. Hence, a step by step approach to tackle this problem is adopted. A reacting flow case with multiple microjets in a combustor, as performed in RANS simulations, is too complex and computationally expensive. Hence, as a first step, non-reacting flow cases with only "one" microjet in the backward-facing step geometry are simulated at different microjet velocities.

Validation of LES results with experimental data are important in studies that are conducted for the first time. This helps establishing the validity of LES methodology in solving this problem. The geometry of the backward facing step with single microjet is based on experimental setup available in the laboratory of our experimental collaborators at the University of Minnesota. As in the RANS simulations, the geometric design of the setup is provided by the simulation group and the LES simulation results are validated with the experimental data provided by our collaborators. The LES results are also compared to RANS $k - \varepsilon$ model

simulations, performed on the same geometry. This provides a comparison of computationally expensive and more accurate LES approach with computationally less expensive RANS simulations.

This chapter studying the effect a single microjet in a backward facing step geometry using the spectral element method is presented in the following format: The computational considerations for the LES study are enumerated in Section 5.2. The instantaneous flow field showing the effect of microjet are presented in Section 5.3. The validation of simulation results with experimental data are provided in 5.4. The analysis of the average flow field using average contours and line plots are discussed in Section 5.5. In Section 5.6, the mixing of passive scalar (mass fraction) is quantified using various mixing indicies. And finally, some concluding remarks are presented in Section 5.7.

5.2 Computational considerations

This section enumerates the setup and considerations in simulating cases which involve turbulent primary flow field interacting with turbulent microjet flow.

5.2.1 Physical setup and numerical model

The backward-facing step geometry with single microjet is shown in Figure 27. The origin is located at the trailing edge of inlet section in the $y - z$ plane passing through the center of the microjet. All the dimensions are normalized with step height of $H = 0.02$ m. Reynolds number based on the step height and reference velocity of $U_0 = 10.8$ m/s is $13,872$. The non-dimensional microjet diameter (d_j) is 0.1. The microjet is placed on the step face and enters

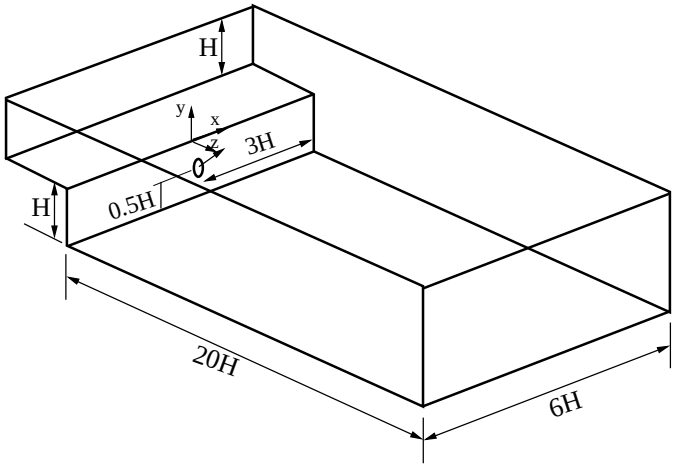

Figure 27. Schematic of backward-facing step geometry with single microjet in the x-y plane.

the geometry at an angle of 45° to the step face. For the flow, the z-direction is the streamwise direction, y-direction is the wall-normal direction and x-direction is the spanwise direction.

The LES studies are performed with a spectral element code, Nek5000. The proven efficiency and accuracy of the implicit LES technique, discussed in Section 3.3, is adopted for these simulations. The filtered Navier-Stokes equations (Equation 3.1 and Equation 3.2) are solved in the domain with prescribed boundary conditions. Outflow boundary is used in the streamwise direction and periodic boundary conditions are prescribed in the spanwise direction. The geometry is confined with walls at the top and bottom in the wall-normal direction. In addition to the filtered Navier-Stokes equations, a filtered transport equation (Equation 3.3) is solved for the mass fraction, $0.0 \leq Y \leq 1.0$, with Schmidt number $Sc = 0.71$. The boundary condition for the mass fraction is set as $Y = 1.0$ for the microjet flow and $Y = 0.0$ in the primary flow.

At the walls zero-gradient boundary condition is applied and periodic boundary conditions are prescribed in the spanwise direction.

As in the first part of this thesis, the RANS simulations are performed with the commercial code ANSYS Fluent using the steady-state RANS equations, described in Section 2.2, within the framework of realizable $k-\varepsilon$ turbulence models. ANSYS Fluent is a dimensional solver, hence, for the RANS studies the non-dimensional geometry shown in Figure 27 is converted to dimensional geometry using the reference step height and reference velocity. Air at standard conditions enters the domain from the primary flow inlet and the 2 mm diameter microjet. The microjet is placed on the step face and enters the domain at an angle of 45^{o} to the step face. Pressure outlet boundary condition is applied in the streamwise direction and periodic boundary conditions are prescribed in the spanwise direction. A no-slip boundary condition is applied at the top and bottom walls. In addition to the momentum equations for the mean flow, a steady-state transport equation for the averaged mass fraction $0.0 \leq \langle Y \rangle \leq 1.0$ is solved. The boundary condition for $\langle Y \rangle$ is set as 1.0 for the microjet flow and 0.0 for the primary flow. Zero-flux boundary condition is specified at the walls and periodic boundary conditions are prescribed in the spanwise direction.

5.2.2 Overview of computations performed

As a start, a case with a relatively low microjet velocity of 20 m/s (normalized velocity is 1.85) is simulated to gain experience in simulating a single microjet case. To resolve all the length scales in the area around the microjet and top and bottom walls, a fine mesh is required in those areas. For the 20 m/s case, a mesh with $E = 16,136$ spectral elements and

polynomial order of $N = 7$ is utilized to accurately resolve the flow field. Figure 28 shows a closeup view of the mesh containing the microjet in y-z plane. The microjet is centered at $(y, z) = (-0.5, 0.0)$. The jet opening is surrounded by a hemispherical mesh enclosed within a square box. This prevents the dense elliptical mesh around the microjet to extend the whole length of the combustor. The experience gained from simulating the 20 m/s case is utilized in simulating the 40 m/s case (normalized velocity is 3.7) with a mesh size of $E = 19,408$ and $N = 7$.

To study the effect of microjet in the backward-facing step geometry, it is important to establish a baseline case without microjets to compare the results. Table V provides the number of elements (E) and the polynomial order (N) utilized for the cases simulated in this study: LES-baseline, 20 m/s (LES-mj20) and 40 m/s (LES-mj40). The velocity ratio is defined as the ratio of the velocity of the microjet to that of the primary flow field.

Case	Microjet velocity	Primary flow Re	Microjet Re	Velocity ratio	E	N
LES-baseline	—	13,872	—	—	9472	7
LES-mj20	20 m/s	13,872	2569	1.85	16,136	7
LES-mj40	40 m/s	13,872	5138	3.7	19,408	7

TABLE V

OVERVIEW OF THE SIMULATED CASES.

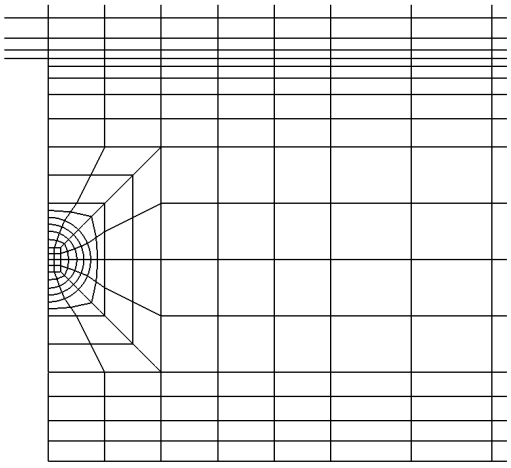

(a)

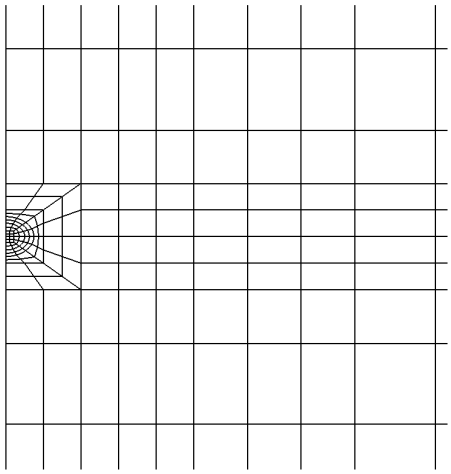

(b)

Figure 28. Mesh resolution around the microjet: (a) front view in the $y - z$ plane (b) top view in the $x - z$ plane.

The prescription of accurate inlet profile for the turbulent primary flow (backward-facing step flow) and the microjet flow are critical for obtaining accurate LES results. The primary flow inlet profile for the mean streamwise velocity and streamwise normal fluctuations are extracted from the experimental data. The streamwise normal fluctuations from the experiments are used in the stochastic model, presented in Section 4.3, to generate the inflow turbulence. Figure 29 shows the mean streamwise velocity profile for the primary flow.

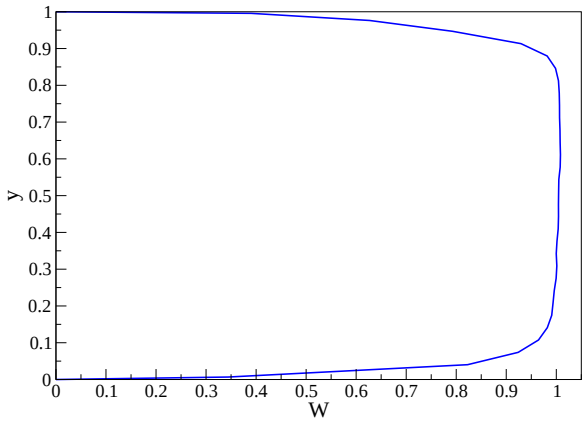

Figure 29. Inlet mean streamwise velocity profile for primary flow.

The inlet profiles for the microjet flow are unavailable from the experiments because the measurement of velocity at the exit of the microjet, near the step wall, are difficult to obtain in experiments. Therefore, different methods were tried to obtain an inlet profile for the microjet. All the trials were conducted for the 20 m/s microjet case. The schematic of the experimental setup for microjet pipe flow, obtained from the experimental group (private communication), is

shown in Figure 30. The microjet pipe setup is attached to the backward-facing step geometry. The large diameter ($d_1 = 5$ mm) pipe is the velocity inlet for the setup and small diameter ($d_2 = 2$ mm) pipe is the microjet velocity outlet that is connected to the backward-facing step geoemtry, at a 45^o angle.

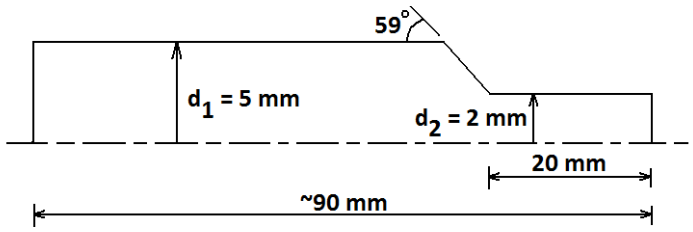

Figure 30. Schematic of experimental setup for microjet pipe flow.

First, a precursor RANS simulation was conducted using ANSYS Fluent within the frame work of realizable $k-\varepsilon$ turbulence models. The microjet pipe flow setup was simulated utilizing an axisymmetric model with a longer pipe length downstream of the nozzle. The velocity profile was extracted from 20 mm downstream of the nozzle and prescribed as the microjet inlet profile in the backward-facing step geometry. The inlet turbulence was generated by imposing random fluctuations on the mean profile. Figure 31(a) shows that the experimental data for average streamwise velocity close to the microjet inlet was well predicted with the microjet inlet profile obtained from the precursor simulation ("Orig"). However, Figure 31(b) shows that the the root mean square (rms) values close to the microjet inlet were not predicted accurately. To

obtain better results, a "Flat" mean inlet profile for the microjet was utilized and the results were compared to the "Orig" mean profile. The change in microjet inlet profile did not affect the rms values close to the microjet. Additional simulations were conducted by increasing the inlet turbulent intensity with the "Flat" and "Orig" mean profiles. In these simulations, some increase in the rms values close to the microjet inlet were observed (not shown here). However, the experimental data were still not predicted accurately.

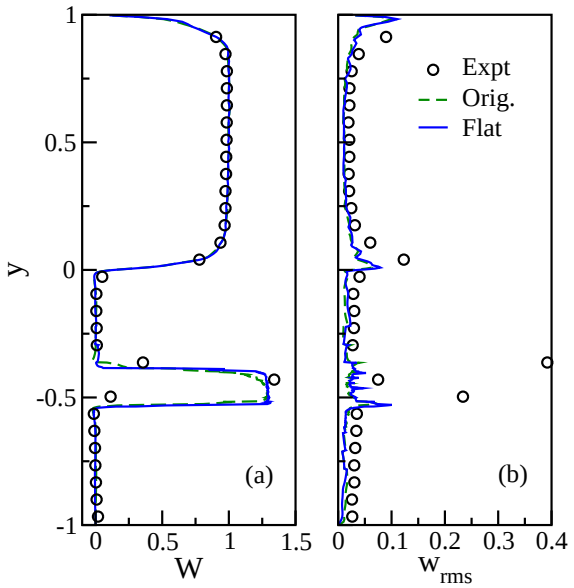

Figure 31. Comparison of velocity profiles close to the microjet inlet at $z = 0.0409$: a) Average streamwise velocity and b) Average streamwise normal fluctuations.

Second, a precursor LES simulation was performed on the microjet pipe setup to obtain accurate mean and rms values for the microjet inlet profile. However, the rms values predicted

by LES simulation was small because the Reynolds number for the 20 m/s microjet velocity ($Re = 2569$) is in the transitional range.

After some discussions with the experimental collaborators, it was concluded that the experimental data close to the microjet was not reliable. The exact flow conditions in the experimental setup of the microjet pipe flow was not known and the measurement of the experimental data inside the microjet was very difficult (personal communication). Hence, to simulate the LES cases as close to experimental setup as possible, a third method was simulated with microjet inlet pipe (Figure 30) attached to the backward-facing step. The modified geometry with the microjet inlet pipe is shown in Figure 32. To keep the spectral element count low, the larger pipe diameter and nozzle section is not included in the computational geometry. The microjet pipe inlet profile is obtained from the RANS precursor simulation, as before, by extracting the profile 8 mm downstream of the nozzle. However, it was observed that this set up lead to laminarization of flow in the pipe section and over prediction of the average streamwise velocity values.

From these studies it was concluded that the 20 mm length of the 2 mm diameter pipe after the contraction is small and hence insufficient to provide a fully developed profile for the microjet cases of 20 m/s and 40 m/s. Hence, on further discussions with our experimental collaborators, it was concluded that using a turbulent profile for the microjet inlet would be a good assumption for these simulations. And that the experimental data for the microjet velocities are reliable three microjet diameters away from the step wall. Hence, for the microjet cases, the inlet mean velocity magnitude profiles utilized are provided in Figure 33.

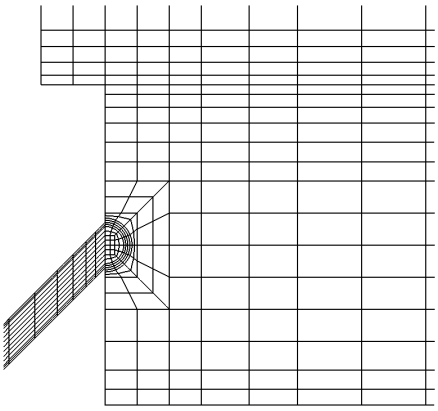

Figure 32. Computational domain with microjet inlet pipe attached to the original mesh.

All the simulations are performed on the HPC resources provided by the Extereme Science and Engineering Discovery Environment (XSEDE) network. The supercomputer TACC Lonestar and SDSC Trestles are utilized for performing the simulations.

The microjet flow puts a constraint on the time step size because of the Courant Fredrich Levy (CFL) condition. Nek5000 utilizes a characteristic scheme which allows for higher CFL number, hence simulations can be performed with larger time step size. However, to capture the small scales of turbulence a small time step size is used for the simulation of the baseline case. In the microjet cases, the microjet velocity dictates the time step size utilized in the simulation. Table VI provides the time step size utilized for the simulations. The microjet cases require a smaller time step size compared to the baseline case. Hence, the microjet cases require longer computational time for simulating the cases as compared to the baseline case. A comparison of

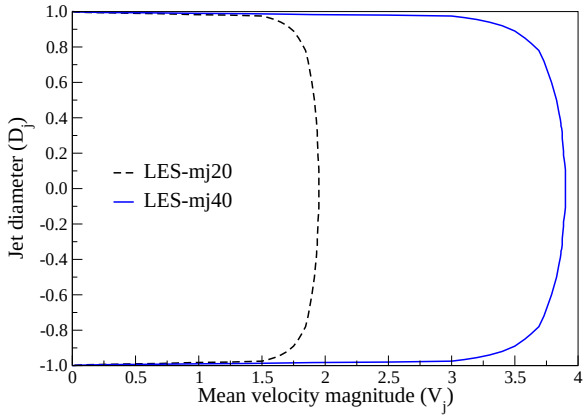

Figure 33. Mean velocity magnitude profile for microjet inlet.

computational time required for one flow through and the total time required for the simulation of the baseline case and the single microjet cases are shown in Table VI. The simulations were run for 10 flow through times to get over initial transients and reach a quasi-stationary state. The simulations were then run for further 15 flow through times for gathering the statistics. The computational times are recorded on TACC Lonestar machine.

Case	E	N	Time step size ($\triangle$t)	Processors	Time per flow through (hrs.)	Total simulation time (hrs.)
LES-baseline	9472	7	2.0×10^{-3}	1032	1.52	30.4
LES-mj20	16,136	7	5.0×10^{-4}	1440	11.12	222.4
LES-mj40	19,408	7	3.0×10^{-4}	1740	17.14	384.34

TABLE VI

COMPARISON OF COMPUTATIONAL TIME BETWEEN THE LES CASES.

The data files generated for post-processing in the microjet cases depend on the size of the mesh utilized. The data file size varies from 0.2 GB to 0.35 GB. The visualization of the data is done with the software package, VisIt, developed at Department of Energy (DOE) Advanced Simulation and Computing Initiative (ASCI) at Lawrence Livermore National Laboratory. A plugin that reads the Nek5000 data files directly was developed by VisIt developer's in collaboration with Nek5000 developer's. The data files generated after the runs on the XSEDE machines are moved to the 40 core cluster in the CMTL laboratory for data visualization. The line plots are generated using the 2D plotting tool, Grace.

The cases simulated for RANS studies are listed in Table VII. The flow details for the cases are similar to the LES cases. In addition, the table provides the number of cells used for the microjet cases and the discretization order utilized for the simulation. The geometry is created using ANSYS SpaceClaim direct modeler and the mesh is created using ANSYS Meshing. A dense tetrahedral mesh is generated in the region around the microjet to resolve the flow. An image showing the mesh around the microjet is given in Figure 34. A hybrid mesh with majority of hexahedral and tetrahedral cells is utilized in the simulation.

Case	Microjet velocity	Primary flow Re	Microjet Re	Velocity ratio	Number of cells	Discretization order
RANS-baseline	—	13,872	—	—	2.8 million	Second
RANS-mj20	20 m/s	13,872	2570	1.85	4.97 million	Second
RANS-mj40	40 m/s	13,872	5140	3.7	4.97 million	Second

TABLE VII

OVERVIEW OF THE CASES SIMULATED WITH RANS.

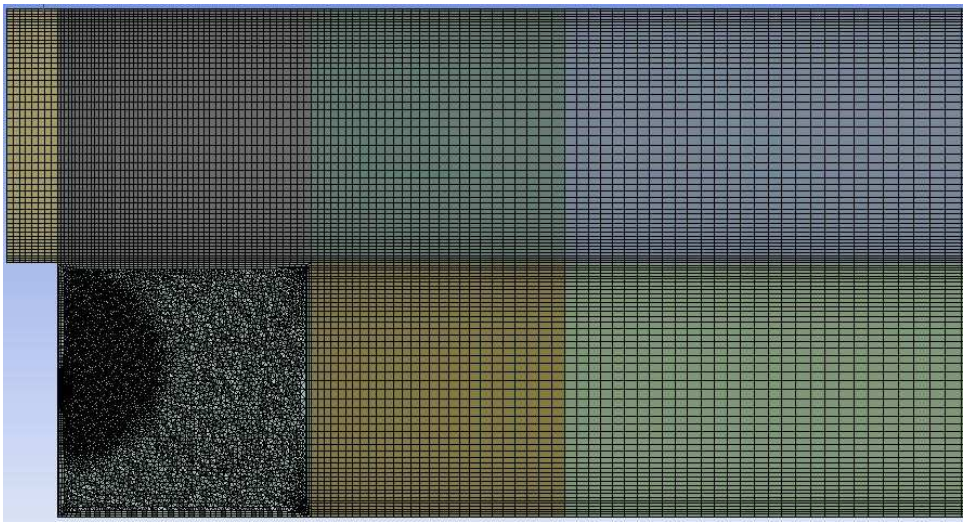

Figure 34. Image of the mesh utilized for microjet cases in RANS studies.

The primary flow inlet profiles for the mean velocity, k and ε are extracted from the experimental data. For the microjet cases, a flat mean velocity profile is specified at the microjet inlet. The cases are simulated using 16 cores on a Windows 2008 Server and the computational time required for simulating the steady-state RANS cases is shown in Table VIII. The data visualization is done using ANSYS Fluent's in built visualization capability and the line plots are generated using Grace.

5.2.3 Simulation of passive scalar

LES studies of passive scalar with spectral element method poses a monotonicity problem, where over- and undershoots are observed in passive scalar values. This problem is absent in direct numerical simulations (DNS) of a passive scalar. However, for our studies DNS will

Case	Number of cells	Solution order	Processors	Total simulation time (hrs.)
RANS-baseline	2.8 million	Second	16	~ 5.0
RANS-mj20	4.97 million	Second	16	~ 8.0
RANS-mj40	4.97 million	Second	16	~ 8.0

TABLE VIII

COMPARISON OF COMPUTATIONAL TIME BETWEEN THE STEADY STATE RANS CASES.

be computationally expensive. One of the remedies to monotonicity problem is to bound the passive scalar values by clipping the over- and undershoots. This technique will be utilized in simulating the microjet cases with a passive scalar.

The technique of clipping the unbounded passive scalar is tested by performing LES studies on the baseline case with different mesh sizes. For these studies the spanwise extent of the domain is reduced from 6H to 3H. The mesh sizes utilized in this study are given in Table IX. The mesh M1 is utilized for simulating two cases, without clipping (w/o clp M1) and with clipping (w/ clp M1).

Mesh	Case	E	N	Clipping
M1	w/o clp M1	4464	7	No
	w/ clp M1	4464	7	Yes
M2	w/o clp M2	10,760	7	No

TABLE IX

MESH SIZES FOR PASSIVE SCALAR STUDIES.

For the case without clipping (w/o clp M1), overshoots ($Y > 1.0$) and undershoots ($Y < 0.0$) are observed in the instantaneous mass fraction values, as seen in Figure 35(a). The maximum overshoot is $Y = 1.471$ at $(x, y, z) = (-1.10207, -0.969768, 10)$ and maximum undershoot is $Y = -0.1151$ at $(x, y, z) = (1, 0.898372, 5.2)$. Figure 35(b) shows contours of instantaneous mass fraction values for the case with clipping, "w/ clp M1." Figure 36(a) and Figure 36(b) show the contours of averaged mass fraction in the spanwise direction for the cases "w/o clp M1" and "w/ clp M1," respectively. After averaging in the "w/o clp M1" case, the undershoots are absent and overshoots are very small. Overall the contours for the two cases are very similar. Therefore, this study explores the use of clipping the overshoots and undershoots by bounding the mass fraction values to $0.0 \leq Y \leq 1.0$.

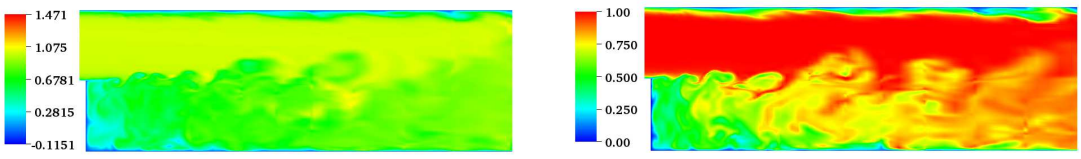

(a) (b)

Figure 35. Instantaneous mass fraction contours in the plane $x = 0.0$: (a) case without clipping (b) case with clipping.

The comparison of line plots of averaged mass fraction for the two M1 cases is shown in Figure 37, at different streamwise locations. At $z = 0.209$, there are minor differences in the values below the shear layer. Downstream of $z = 0.209$, the two cases without and with

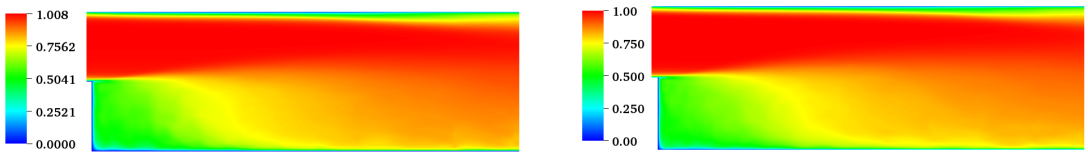

(a) (b)

Figure 36. Averaged mass fraction contours: (a) case without clipping (b) case with clipping.

clipping have similar values. This is an interesting result which leads to an investigation and quantification of the unbounded passive scalar values. For this, a mesh M2 is simulated with more than twice the size of mesh M1, as observed in Table IX. This mesh M2 is simulated without clipping (w/o clp M2) of mass fraction values. The line plots of averaged mass fraction values for mesh M2 compared with mesh M1 are shown in Figure 37. In the region close to the step ($z \leq 2.02$), the three cases have differences in values close to the bottom wall. However, in the downstream sections the results for all the three cases are similar.

The overshoots and undershoots are noticed in the instantaneous mass fraction values and not noticed in the averaged values. In addition, the line plots of averaged mass fraction values suggest that the overshoots and undershoots are very small. To quantify this the volumes of overshoots and undershoots are compared to the total volume of the geometry. The total volume of the geometry is 160 cubic units. The undershoots in mass fraction values are very small (of the order 10^{-8} cubic units) and hence negligible. Table X and Table XI provide the volumes of mass fraction overshoots for mesh M1 and mesh M2 respectively. The tables also provide the ratio of overshoot volume to the total volume. For both meshes, overshoot volumes

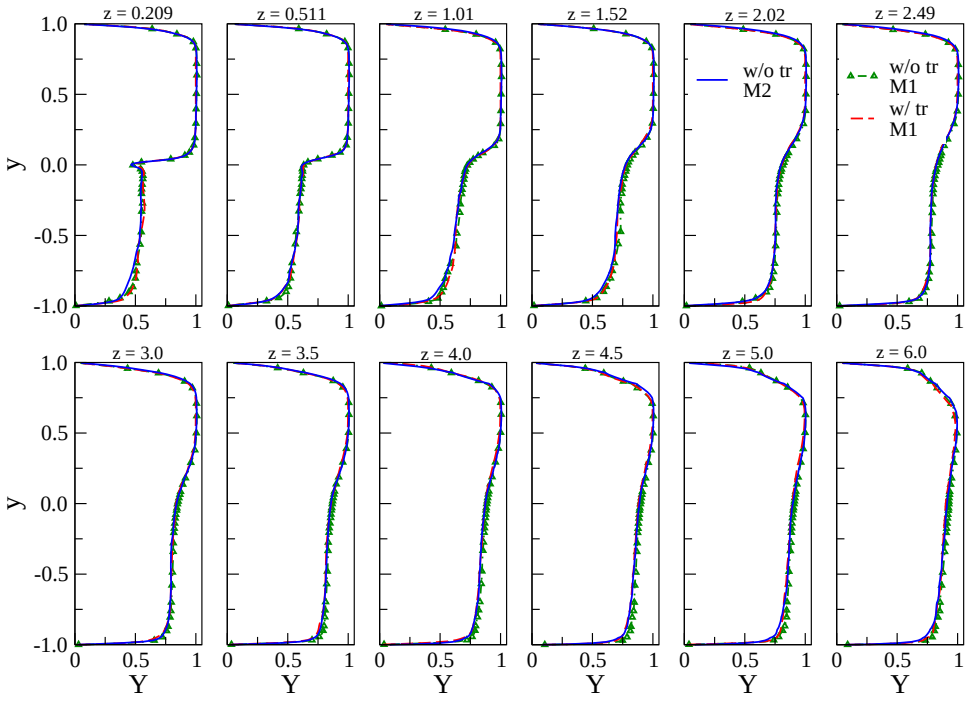

Figure 37. Comparison of averaged mass fraction for without microjet cases M1 and M2.

are only about 10% of the total volume and most of the overshoot is in the range of $1.0 - 1.01$. The values provided in the tables are for a single time step. However, similar percentage for the ratio of overshoot volume to total volume is observed for other time steps as well.

The case without clipping and with clipping give similar results because most of the overshoots are in a small range around $Y = 1.0$ and the undershoots occupy a very small volume. This justifies the technique of clipping the mass fraction values for the LES studies.

In RANS studies, the steady-state transport equation for the mass fraction $\langle Y \rangle$ is solved as a post-processing step with appropriate boundary conditions for the scalar.

Overshoot Values	Vol.	% of total vol.
1.0 - 1.01	13.11	8.15%
1.01 - 1.1	2.28	1.42%
1.1 - 1.2	5.976×10^{-3}	3.72×10^{-3}%
1.2 - 1.3	1.78×10^{-4}	1.11×10^{-4}%
1.3 - 1.471	3.114×10^{-5}	1.94×10^{-5}%
Total	15.39	9.67%

TABLE X

OVERSHOOT VOLUMES OF MASS FRACTION FOR MESH M1.

Overshoot Values	Vol.	% of total vol.
1.0 - 1.01	15.17	9.43%
1.01 - 1.1	1.44	0.89%
1.1 - 1.2	1.92×10^{-3}	1.19×10^{-3}%
1.2 - 1.3	6.80×10^{-5}	4.23×10^{-5}%
1.3 - 1.457	1.64×10^{-5}	1.02×10^{-5}%
Total	16.71	10.39%

TABLE XI

OVERSHOOT VOLUMES OF MASS FRACTION FOR MESH M2.

5.3 Instantaneous flow field

Introducing a microjet in the geometry changes the flow field and produces large shear in the plane with microjet. This can be observed from the comparison of the instantaneous streamwise velocity contours, shown in Figure 38 in the plane $x = 0.0$ passing through the center of the microjet. The velocity contours show the shear generated by the interaction of the jet and the primary flow.

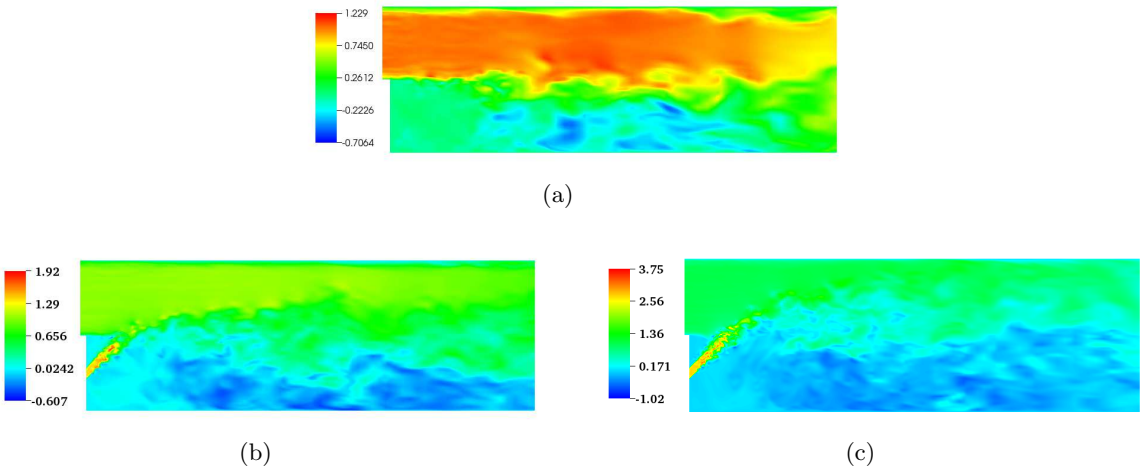

Figure 38. Instantaneous streamwise velocity contours: (a) baseline case without microjet, (b) 20 m/s microjet case and (c) 40 m/s microjet case.

Figure 39 shows the interaction of the jet with the shear layer using the streamwise velocity contours and uniformly scaled vectors in different streamwise planes, for the two microjet cases. For clarity, only some of the velocity vectors are plotted to show the effect of the microjet.

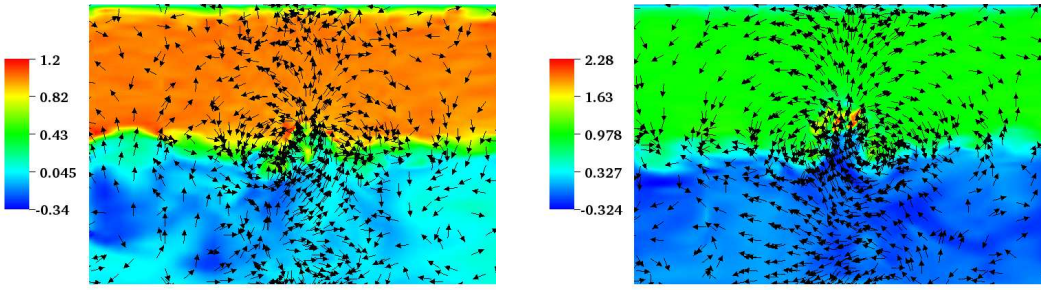

(a) LES-mj20; z = 0.75

(b) LES-mj40; z = 0.75

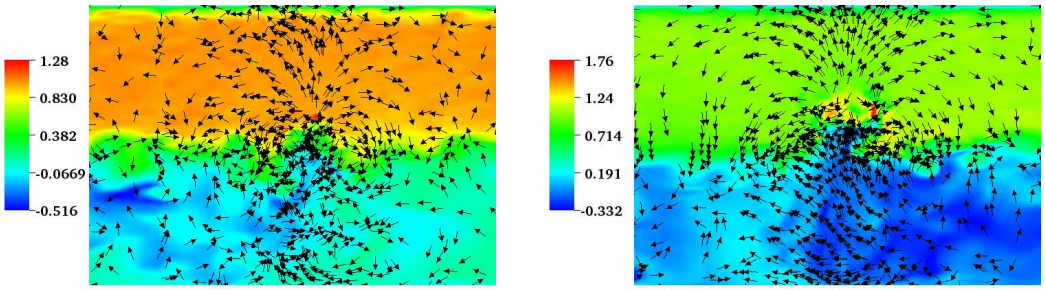

(c) LES-mj20; z = 1.0

(d) LES-mj40; z = 1.0

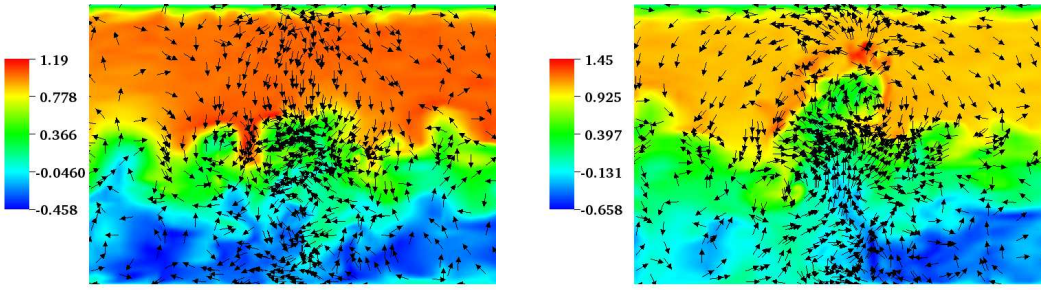

(e) LES-mj20; z = 2.0

(f) LES-mj40; z = 2.0

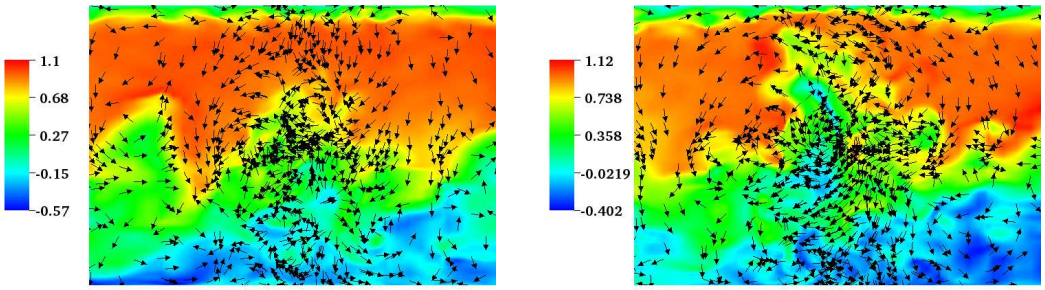

(g) LES-mj20; z = 4.0

(h) LES-mj40; z = 4.0

Figure 39. Instantaneous streamwise velocity contours and uniformly scaled vectors of velocity magnitude in different streamwise planes for the two microjet cases: (a),(c),(e),(g) LES-mj20 case and (b),(d),(f),(h) LES-mj40 case .

The streamwise velocity contours show the strong upward flow that is generated by the impact of the jet on the shear layer, near the centerplane $x = 0.0$. The 40 m/s jet has a higher impact on the shear layer and penetrates more in the wall normal direction as compared to the 20 m/s case. The pattern of the velocity vectors shows that the jet impacts the shear layer and gives rise to the counter-rotating motion in the shear layer around the centerplane. The counter-rotating motion is the main cause of entrainment of the primary flow into the jet. There are also recognizable small instantaneous eddies near the centerplane and away from it.

The passive scalar, utilized for quantifying the mixing due to microjet, is introduced into the microjet flow after the flow field has reached a quasi-stationary state. Considering the time of injection (t_{ps}) of the passive scalar as zero, Figure 40 shows the instantaneous contours of mass fraction in the plane $x = 0.0$ for different convective times. The 40 m/s jet with its higher momentum penetrates the shear layer and entrains the primary flow which leads to greater spreading of the passive scalar, as compared to the 20 m/s case.

The isosurfaces of mass fraction provide a representation of the large scale mixing due to the interaction of the jet with the primary flow. Figure 41 and Figure 42 show the isosurfaces of mass fraction, $Y = 0.05$, for the 20 m/s and 40 m/s cases in the front view and top view, respectively. In the front view, a clear bending of the 20 m/s jet is observed because of the interaction with the primary flow. The overall character of the flow becomes more corrugated with increasing jet velocity. In the 40 m/s case, further downstream large pockets of the primary flow tend to enter the jet to a higher degree than the 20 m/s case. This qualitatively shows

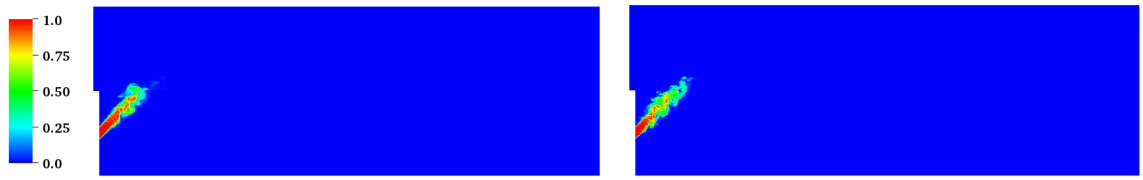

(a) LES-mj20; $t_{ps} = 0.9$ (b) LES-mj40; $t_{ps} = 0.9$

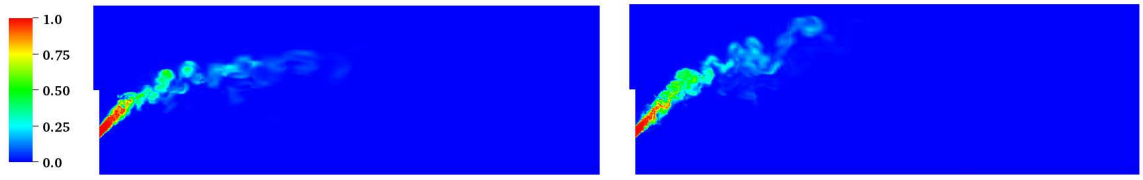

(c) LES-mj20; $t_{ps} = 3.0$ (d) LES-mj40; $t_{ps} = 3.0$

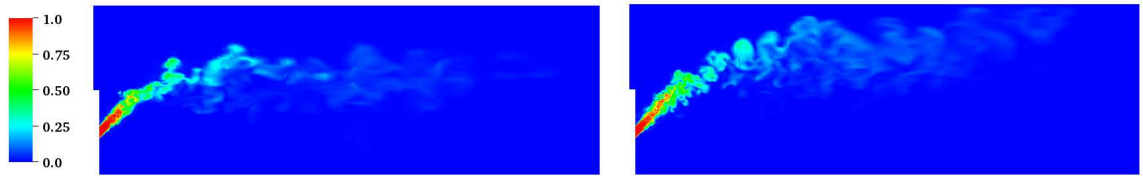

(e) LES-mj20; $t_{ps} = 6.0$ (f) LES-mj40; $t_{ps} = 6.0$

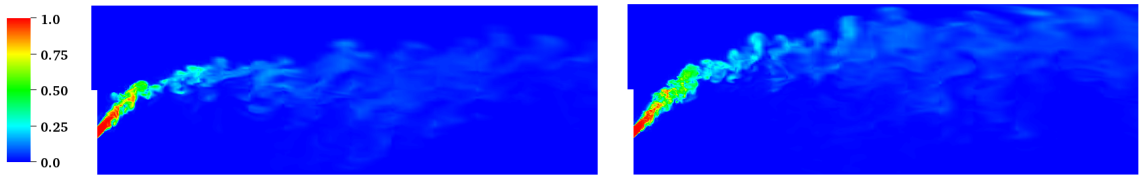

(g) LES-mj20; $t_{ps} = 9.8$ (h) LES-mj40; $t_{ps} = 9.8$

Figure 40. Instantaneous passive scalar (mass fraction) contours at different convective times: (a),(c),(e),(g) LES-mj20 case and (b),(d),(f),(h) LES-mj40 case.

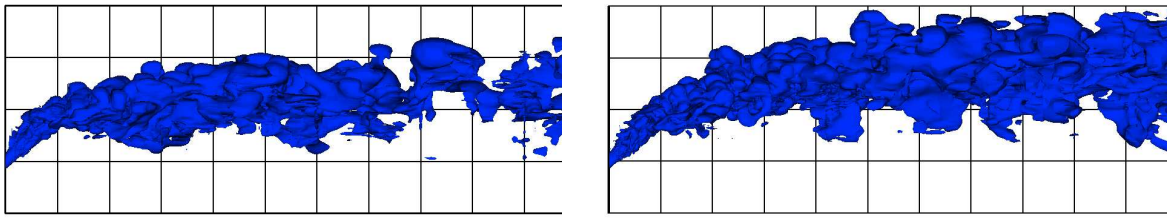

(a) (b)

Figure 41. Front view of instantaneous isosurfaces of mass fraction, $Y = 0.05$, for: (a) LES-mj20 case and (b) LES-mj40 case.

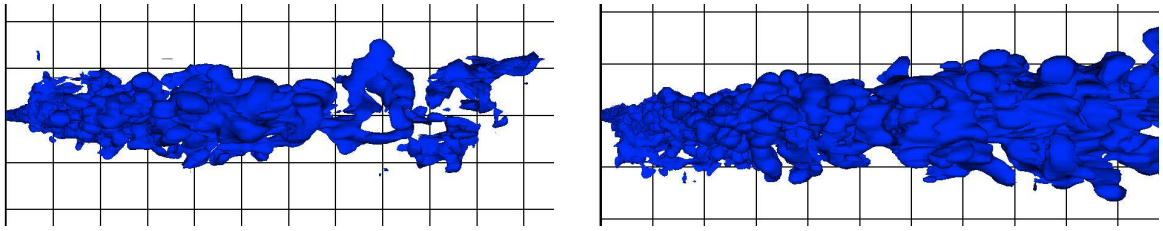

(a) (b)

Figure 42. Top view of instantaneous isosurfaces of mass fraction, $Y = 0.05$, for: (a) LES-mj20 case and (b) LES-mj40 case.

that there is higher degree of spatial mixing in the 40 m/s case as compared to the 20 m/s case.

5.4 Validation studies

To study the effect of microjet in backward facing step geometry, a baseline case without microjet needs to be established. Figure 43 shows the validation of the LES results for averaged streamwise velocity profiles (W) and averaged root mean squared streamwise velocity profiles (w_{rms}) with the experimental data. The simulations predict the averaged streamwise velocities in the shear layer accurately. Below the shear layer in the recirculation zone there is some over

prediction at $z = 1.52$ and 2.02. The primary flow region is very well predicted by the simulation results. The experimental data is available only close ($X/h = 3.16$) to the step and hence no validation is shown for further downstream locations. The values for w_{rms} are over predicted in the shear layer region, close to the step. The values close to the top wall are predicted well with the stochastic model. Near the step the values at bottom wall are well predicted.

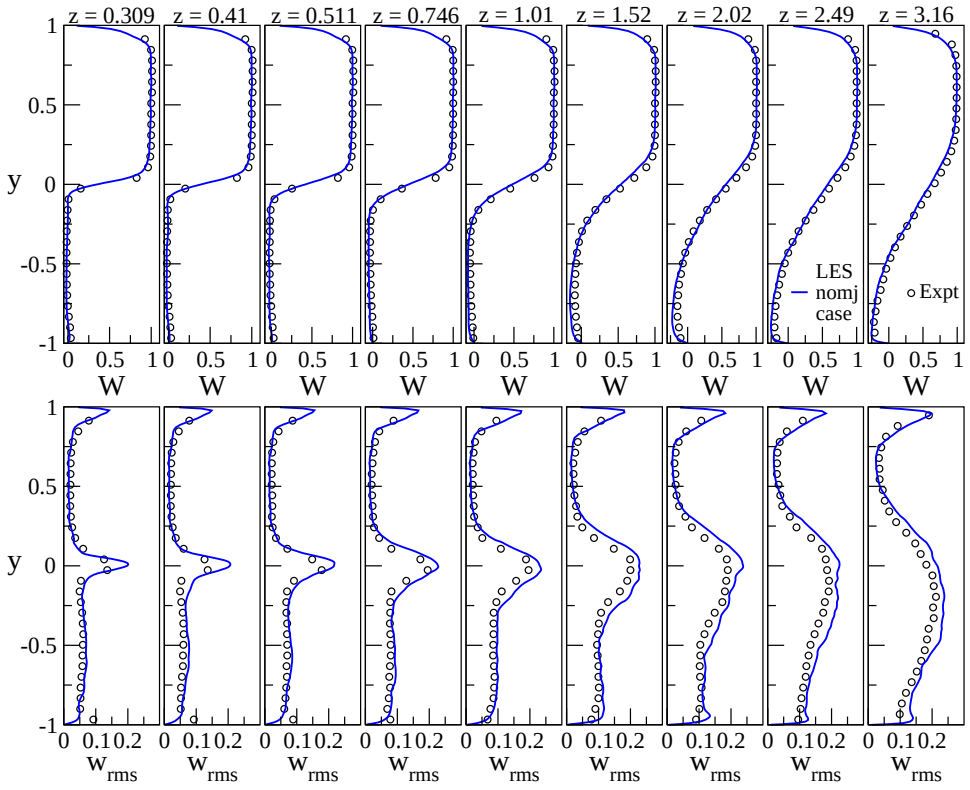

Figure 43. Validation of the simulation results with experimental data for baseline case without microjet.

For the 20 m/s case, the LES data comparison of average streamwise velocity (W) and averaged root mean squared streamwise velocity (w_{rms}) with experimental data at various axial locations is shown in Figure 44. The experimental data for average streamwise velocity is predicted very well at all the axial locations. At $z < 0.511$, there are some differences in the microjet velocity values for the simulation and experimental data. This difference can be because of the absence of the exact microjet inlet profile from the experiments. There is a good comparison of average streamwise velocity values near the top and bottom walls. The w_{rms} data from the microjet in predicted very well. There is good agreement between the simulation data and experimental data at the bottom wall, while the values at the top wall are under-predicted. Overall there is a good agreement between the experimental and simulation values of w_{rms}.

Figure 45 shows the comparison of LES results for averaged streamwise velocity (W) and streamwise normal fluctuations (w_{rms}) with the experimental data for the 40 m/s case. At axial locations $z \leq 1.01$, the predictions of W and w_{rms} values for the microjet are over-predicted. This over-prediction can be attributed to the lack of correct inlet profile for the microjet from the experiments. Overall the experimental data for the averaged streamwise velocity is well predicted by the simulations. The w_{rms} data shows good agreement between the simulation data and experimental data at the bottom wall, while the values at the top wall are under-predicted.

A comparison of averaged streamwise velocity profiles obtained from RANS simulations is provided in Figure 46. For the RANS-baseline case, Figure 46(a), the RANS results predict the

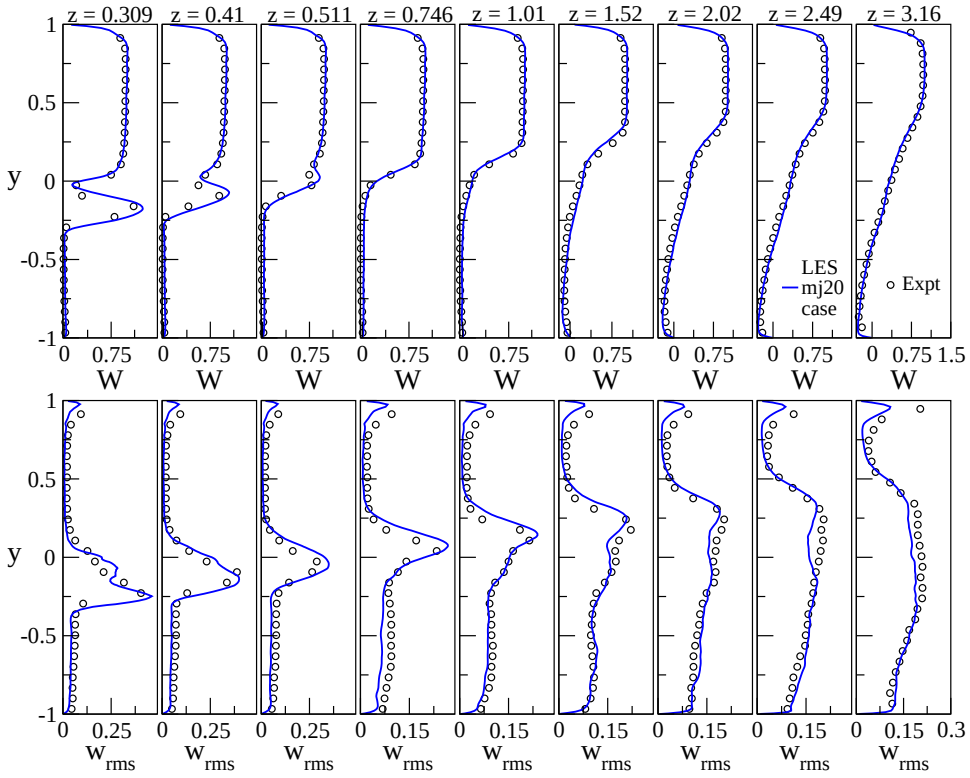

Figure 44. Validation of the simulation results with experimental data for the 20 m/s microjet case.

averaged values of streamwise velocity quite accurately. The values in the shear layer are over predicted in the upstream region closer to the step and there is some over prediction closer to the bottom wall at $z = 1.01, 1.52$ and 2.02.

Figure 46(b) shows a comparison of results from RANS-mj20 case for averaged streamwise velocity (W) profiles with experimental data at different streamwise locations. Close to the step, $z = 0.309, 0.41$ and 0.511, RANS under predicts the values for the microjet velocity. This also affects the prediction of velocity data at other streamwise locations in the recirculation region.

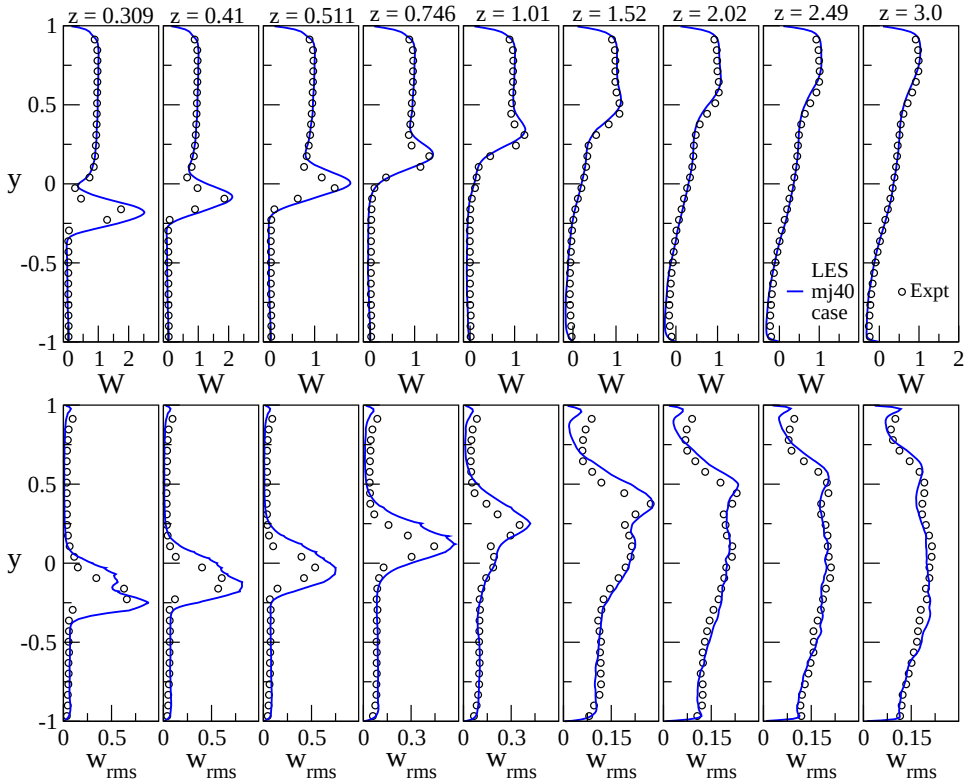

Figure 45. Validation of the simulation results with experimental data for the 40 m/s microjet case.

As the effect of the 20 m/s jet diminishes, the RANS prediction is quite accurate downstream of $z = 1.52$. To eliminate the possibility of mesh resolution around the microjet, a case with dense mesh (~ 10 million cells) was simulated. The mesh resolution did not improve the prediction of the microjet velocity and the results at other locations are similar to the current mesh (not reported here).

The validation plot comparing results of averaged streamwise velocity (W) for RANS-mj40 case with experimental data is shown in Figure 46(c). RANS predicts the penetration of the

microjet quite accurately, this behavior is contrary to that observed for the RANS-mj20 case. The values are well predicted at all the locations, except at $z = 0.746, 1.01$ and 1.52 the values of streamwise velocity are over predicted in the recirculation zone close to the bottom wall.

Overall, the LES results for the mean flow as well as the fluctuations show good agreement with the experimental data for the baseline case, 20 m/s microjet case and the 40 m/s microjet case. The RANS results for the 20 m/s microjet case underpredict the values of averaged streamwise velocity close to the microjet exit. However, RANS results for the baseline case and 40 m/s microjet case compare well with the experimental data.

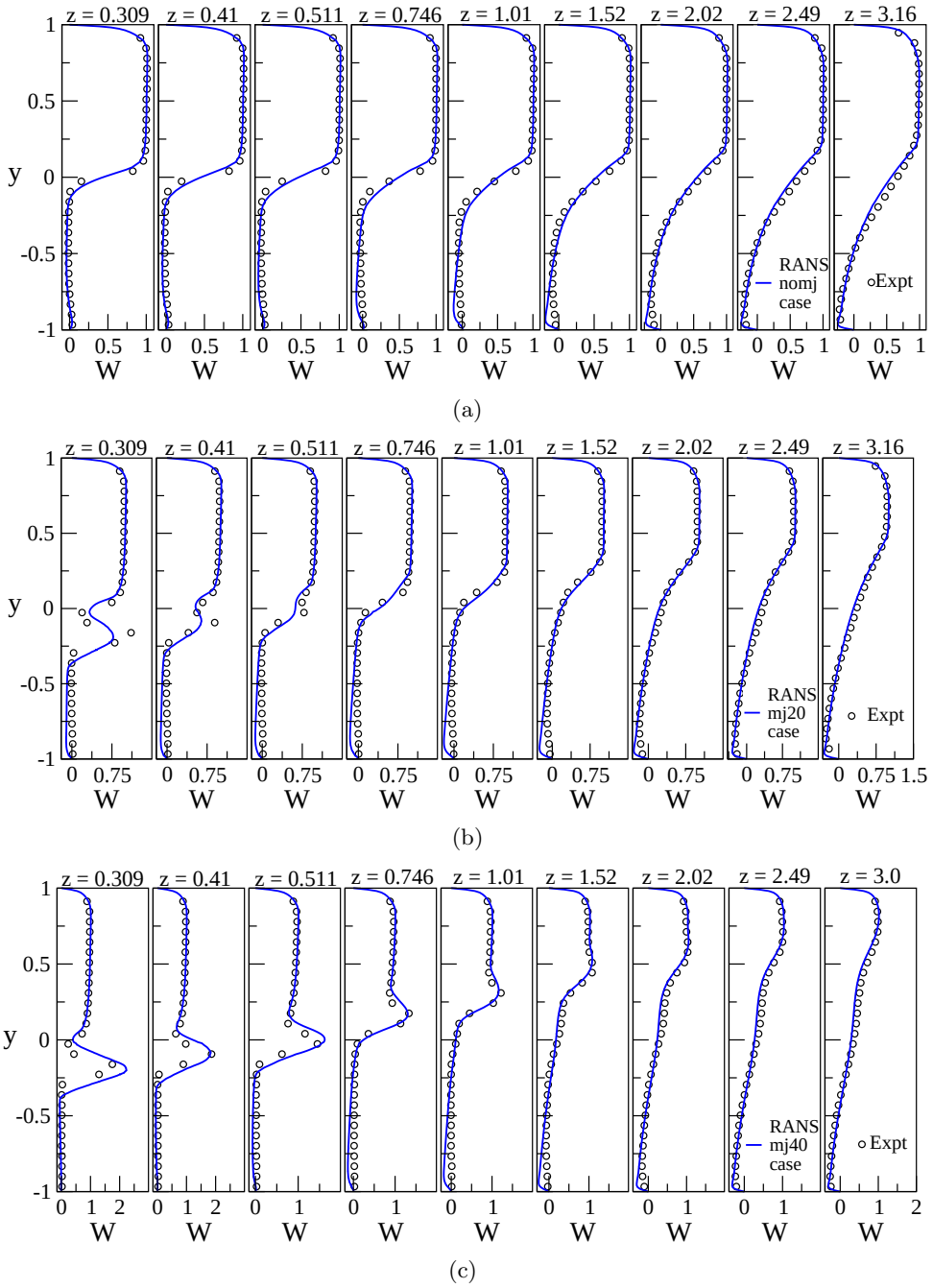

Figure 46. Validation of the simulation results with experimental data for RANS cases: (a) RANS-baseline case without microjet, (b) RANS-mj20 case and (c) RANS-mj40 case.

5.5 Interaction of microjet with shear layer

5.5.1 Velocity field

The contours of averaged streamwise velocity in the plane, $x = 0.0$, passing through the center of the microjet, are shown in Figure 47. The microjet impacts the shear layer and changes the flow field as compared to the baseline case without microjet.

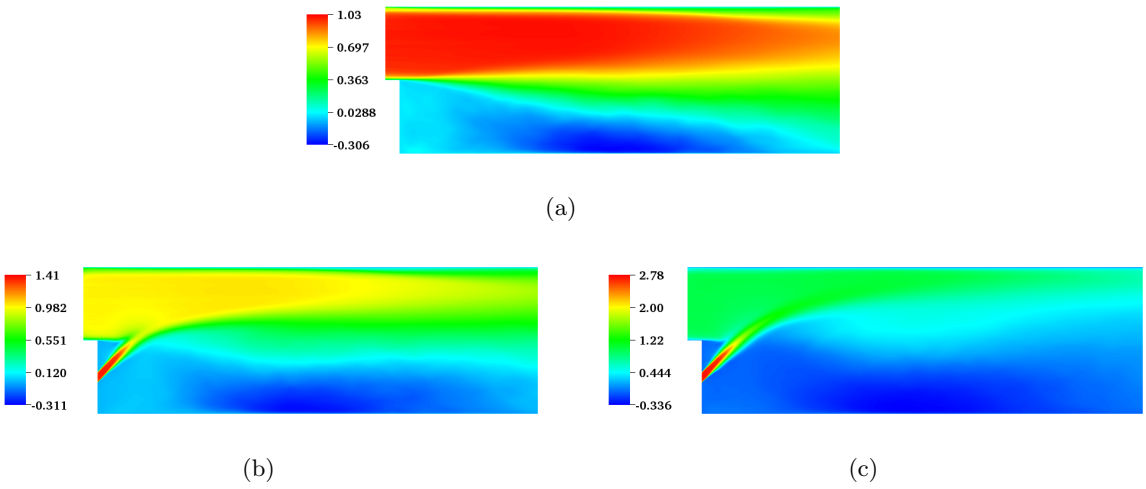

Figure 47. Averaged streamwise velocity contours: (a) LES-baseline case, (b) LES-mj20 case and (c) LES-mj40 case.

Figure 48 shows a comparison of the jet trajectory for the two LES microjet cases. The jet trajectory is plotted using the streamline of the average flow field passing through the center of the microjet. The trajectory of the 40 m/s jet is higher as compared to that of the 20 m/s jet. This shows that the 40 m/s jet penetrates the flow field more as compared to the 20 m/s jet. The jet trajectory also shows the interaction of microjet with the shear layer and the effect

of the primary flow on the jet trajectory. The penetration of the 20 m/s jet into the flow field reduces due to the bending of the jet trajectory from the interaction with the primary flow field. The bending of the 40 m/s jet trajectory is lower than the 20 m/s jet trajectory and hence the 40 m/s jet has a higher impact on the flow field.

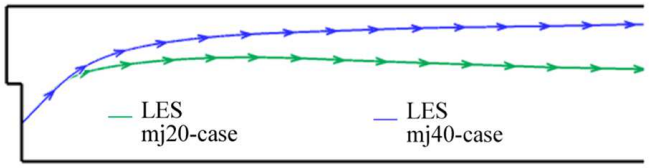

Figure 48. Jet trajectory comparison for LES-mj20 case and LES-mj40 case.

The change in the flow field due to the interaction of the shear layer and the microjet is illustrated in Figure 49. The figure compares the effect of 20 m/s and 40 m/s microjet on the streamwise velocity contours in different streamwise planes (z-direction). In the baseline case, the shear layer is primarily two dimensional. The microjet impacts the uniform two dimensional shear layer at $(x, y, z) = (0.0, 0.0, 0.5)$ and changes the flow structure. The primary flow is displaced in the wall-normal and spanwise directions causing a change in the shape of the shear layer. The height of the shear layer increases in the wall-normal directions with increasing microjet velocity. In the spanwise plane, the effect of the microjet extends up to $x = \pm 0.5$ for the 20 m/s case and $x = \pm 0.75$ for the 40 m/s case (figure not shown).

A comparison of line plots for the baseline case and the two microjet cases, LES-mj20 and LES-mj40, is shown in Figure 50. The line plots are extracted from the plane passing through

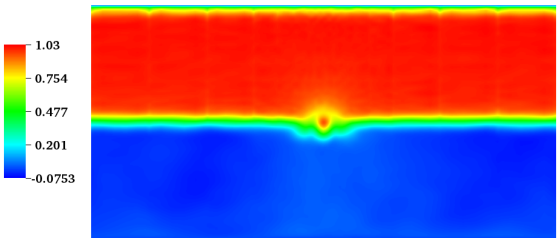

(a) LES-mj20: z = 0.5

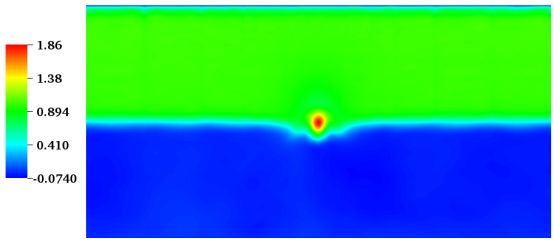

(b) LES-mj40: z = 0.5

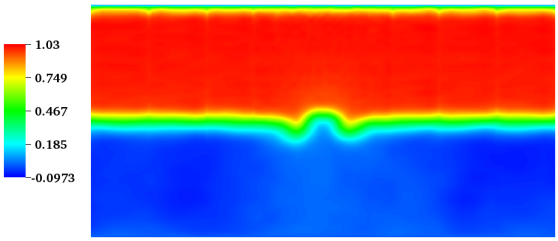

(c) LES-mj20: z = 0.75

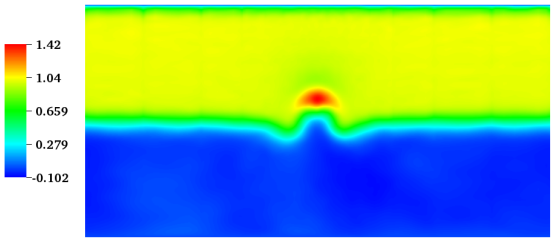

(d) LES-mj40: z = 0.75

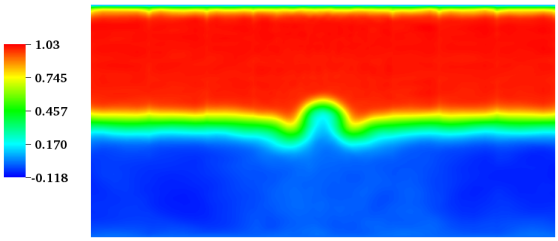

(e) LES-mj20: z = 1.0

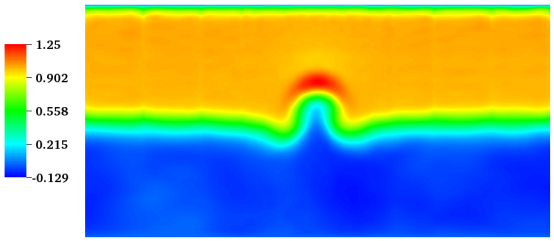

(f) LES-mj40: z = 1.0

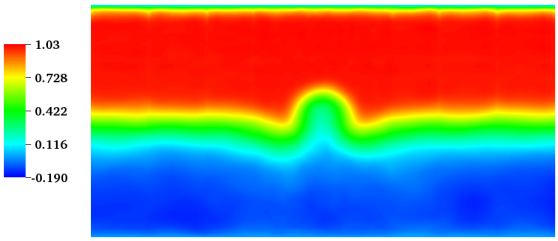

(g) LES-mj20: z = 1.5

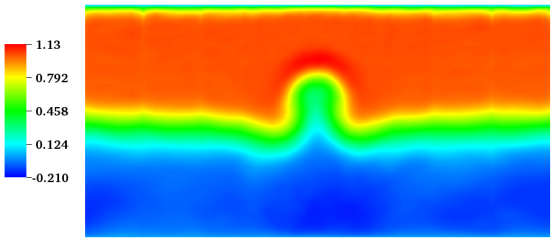

(h) LES-mj40: z = 1.5

Figure 49. Effect of 20 m/s and 40 m/s microjet cases in the streamwise planes.

the center of the microjet ($x = 0.0$) to show the effect of the microjet through comparison with the baseline case without microjet.

Comparison of average streamwise velocity in Figure 50(a) show that the 20 m/s jet penetrates in the streamwise direction to a distance of about $z = 0.511$ and in the wall normal direction to a distance of about $y = 0.05$. The 40 m/s jet penetrates to a distance of $z = 1.52$ and $y = 0.5$ in the streamwise direction and the wall normal direction, respectively. The negative velocities exhibited by all the three cases are very similar. However, the microjet increases the size of the shear layer in the wall-normal direction as compared to the baseline case. This effect is noticed more in the 40 m/s case as compared to the 20 m/s case. A close inspection of the figure reveals that the microjet creates significant three-dimensionality in the flow. In the plane of the microjet, with an increase in microjet velocity the fluid in this region gets displaced to other spanwise planes and hence exhibits reduced streamwise velocities as compared to the baseline case. The effect of the microjets on the length of the recirculation zone, Z_r, is not significant. Compared to the baseline case with $Z_r = 6.38$, the LES-mj20 case has a higher Z_r of 6.42, while, the LES-mj40 case has a lower $Z_r = 6.22$.

Figure 50(b) shows the line plot comparison of averaged wall-normal velocity. The 20 m/s jet penetrates to a distance of $z = 0.746$ and $y = 0.15$ in the streamwise and wall-normal distance, respectively. The 40 m/s jet penetrates to a larger distance than the 20 m/s jet, $z = 1.52$ and $y = 0.45$ in the streamwise and wall-normal directions, respectively. The interaction of the shear layer with the microjet gives rise to a secondary peak in wall-normal velocity at $z = 1.52$

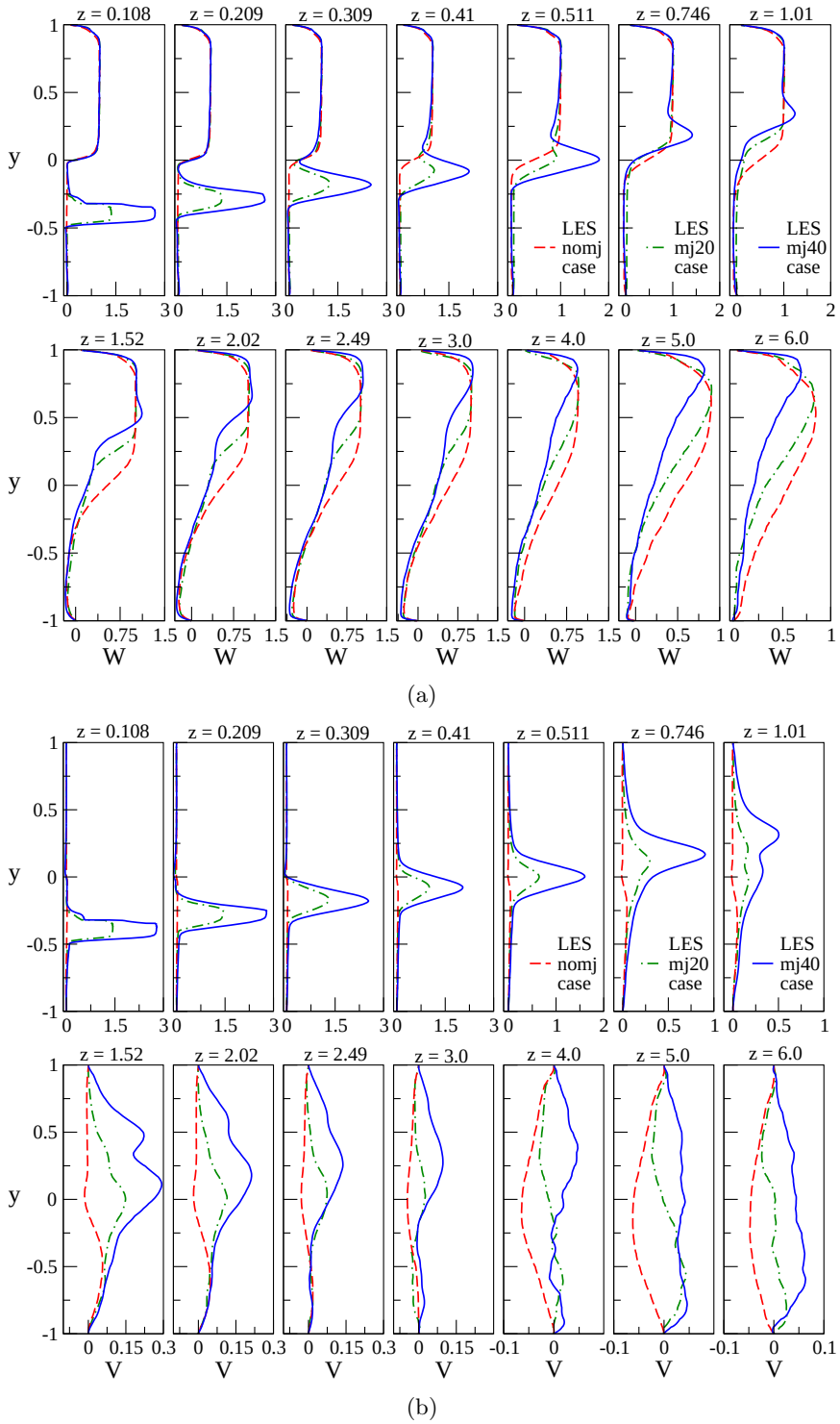

Figure 50. Comparison of line plots in the plane passing through the center of the microjet ($x = 0.0$): (a) average streamwise velocity and (b) average wall-normal velocity.

and $y = 0.0$ for the LES-mj20 case and $z = 1.52$ and $y = 0.12$ for the LES-mj40 case. These secondary peaks in the wall-normal velocity for the microjet cases occur in the region where the streamwise velocity is small. As the effect of the jet reduces, in the LES-mj20 case the values fo V range from positive values in the recirculation region to negative values above the shear layer where the values are closer to the LES-baseline case. The LES-mj40 case exhibits a greater effect of the microjet and shows positive values above and below the shear layer at $z = 5.0$ and $z = 6.0$.

The contour plots and the line plots have shown that the microjet impinges the shear layer and changes the flow field as compared to the baseline case. The 40 m/s jet exhibits a greater penetration into the flow field and hence affects the flow field to a higher extent as compared to the 20 m/s case. The microjet interacts with the shear layer to displace the primary flow in the spanwise direction and drags the fluid in the wall-normal direction. Therefore, the microjet flow imparts three-dimensionality to the shear layer and gives rise to a circular secondary motion.

The comparison of the average streamwise velocity contours for the RANS and LES microjet cases in the plane containing the microjet ($x = 0.0$) is shown in Figure 51. The velocity contours for the RANS-mj20 case differ from the LES-mj20 case because of the lower penetration of the microjet. However, the contours for the RANS-mj40 case and LES-mj40 case are similar.

Figure 51(e) shows the comparison of jet trajectories between the LES and RANS microjet cases. Due to the lower penetration of the 20 m/s microjet in the RANS simulation, the trajectory bends more due to interaction with the primary flow and hence, the trajectory for RANS-mj20 case is lower than the trajectory for the LES-mj20 case. The trajectory for the

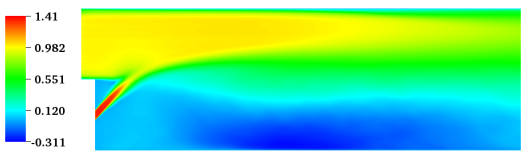

(a) LES-mj20 case

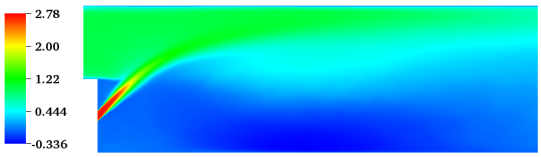

(b) LES-mj40 case

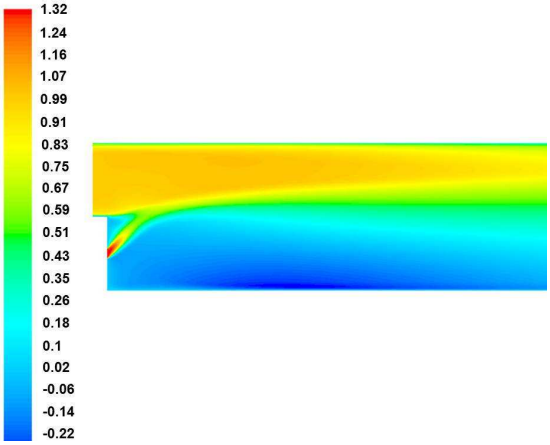

(c) RANS-mj20 case

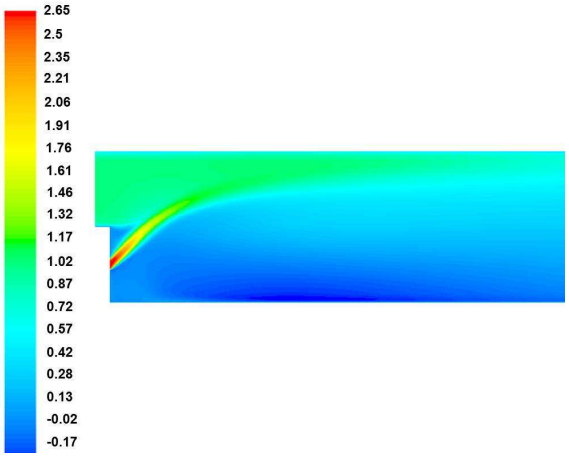

(d) RANS-mj40 case

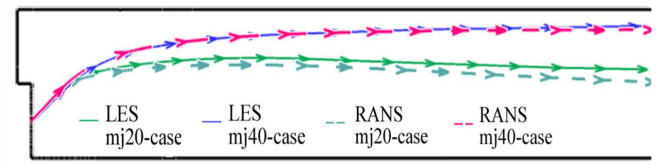

(e) Jet trajectory comparison

Figure 51. (a), (b), (c) and (d): Comparison of averaged streamwise velocity contours in the plane containing the microjet ($x = 0.0$) and (e) Jet trajectory comparison between RANS and LES for 20 m/s and 40 m/s microjet cases.

RANS-mj40 case compares well with the trajectory for the LES-mj40 case. As in LES results, RANS also predicts that the 40 m/s case has a higher impact on the flow field.

Figure 52 shows the comparison of streamwise velocity contours for the RANS and LES microjet cases in the streamwise plane $z = 1.5$. The RANS-mj20 case shows a greater spreading of the 20 m/s microjet in the spanwise direction as compared to the LES-mj20 case. For the mj40 case, the RANS simulation predicts more spreading of the 40 m/s microjet as compared to the LES-mj40 case. In both the microjet cases, RANS predicts a higher maximum negative value for the averaged streamwise velocity in the recirculation zone as compared to the LES results.

Figure 53 shows the line plot comparison of RANS and LES results for averaged streamwise velocity (W) and wall-normal velocity (V) for the mj20 case. Close to the microjet exit at $z = 0.108$, the peak microjet velocity for RANS is close to the LES data. However, as the microjet penetrates into the flow field, RANS predicts greater spreading of the microjet. Hence, RANS predicts a lower penetration of the microjet in the streamwise and wall-normal direction as compared to the LES prediction. The lower momentum of the microjet predicts an earlier onset of recirculation zone which leads to differences in the values of W and V close to the bottom wall. Once the effect of the microjet vanishes downstream of $z = 1.01$, the RANS results for W compare well with LES results. RANS over predicts the length of the recirculation zone which leadds to large differences in the values of V between RANS and LES results, downstream of $z = 2.49$. The value of Z_r for the RANS case is 9.72 as compared to 6.42 for the LES case.

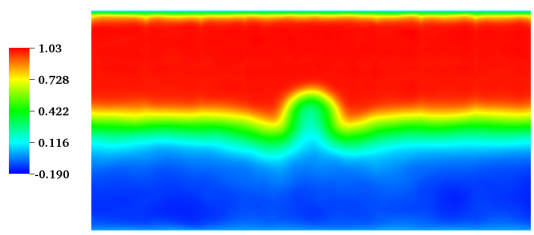

(a) LES-mj20 case

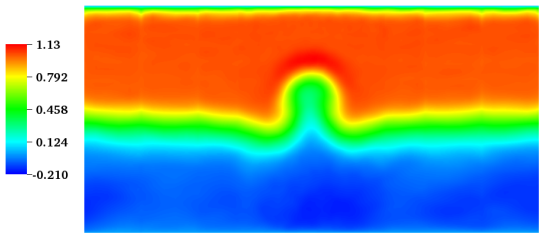

(b) LES-mj40 case

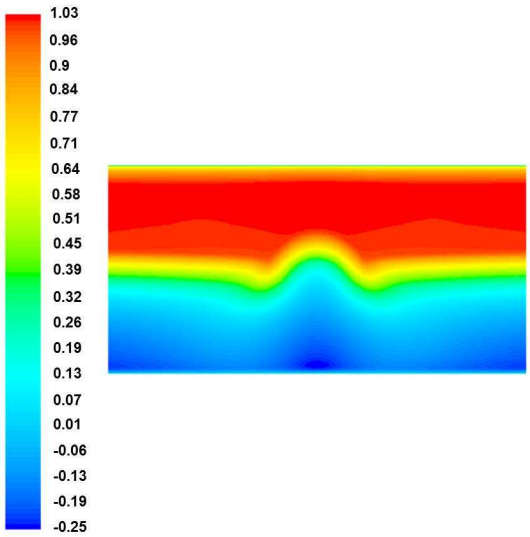

(c) RANS-mj20 case

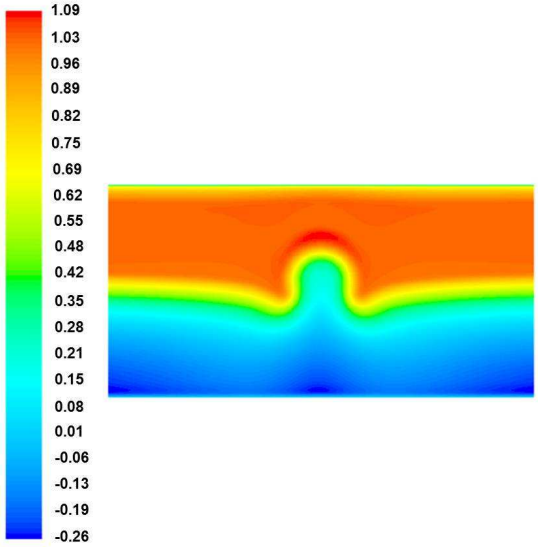

(d) RANS-mj40 case

Figure 52. Comparison of averaged streamwise velocity contours in the plane $z = 1.5$: (a) LES-mj20 case, (b) LES-mj40 case, (c) RANS-mj20 case and (d) RANS-mj40 case.

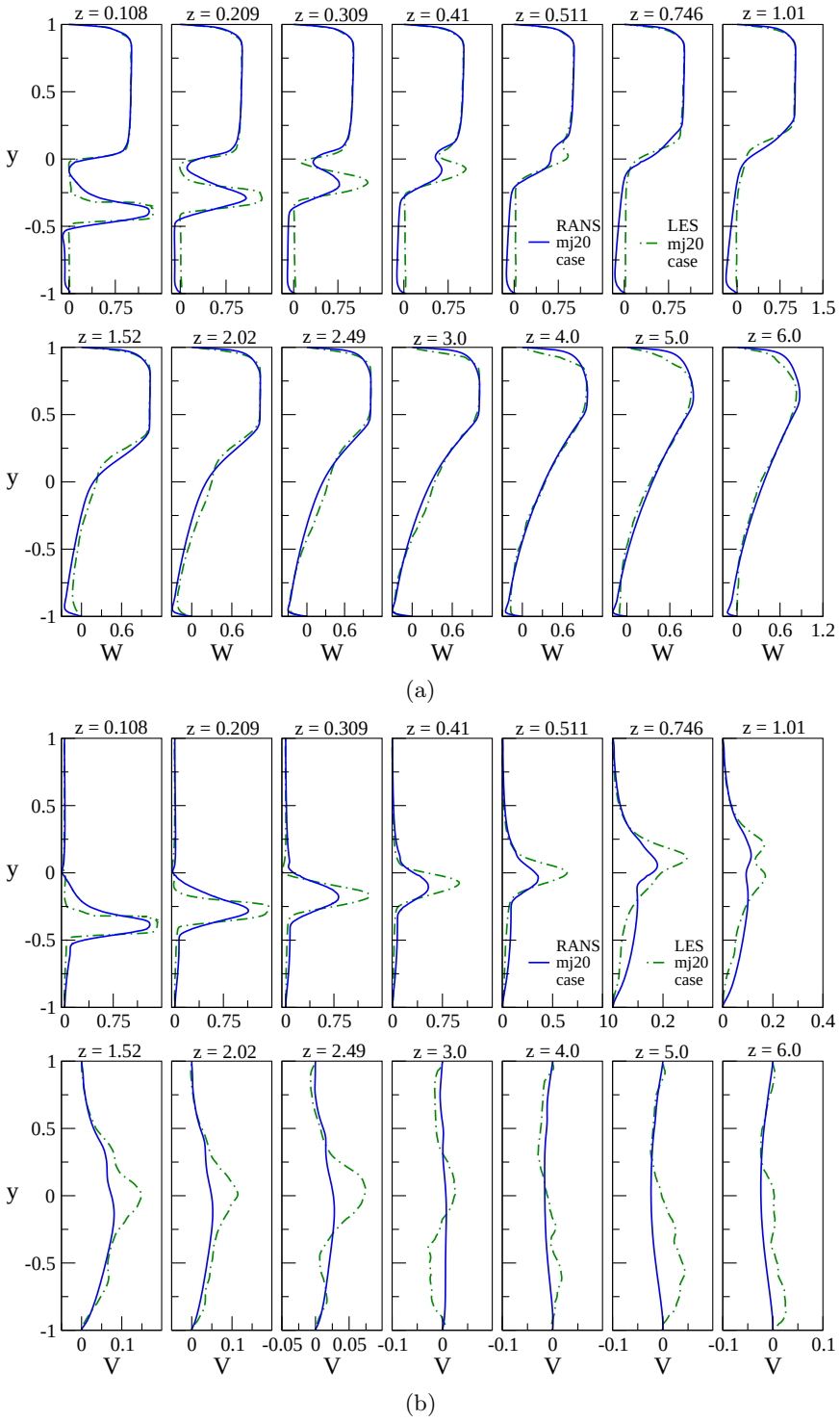

Figure 53. Comparison of RANS and LES line plots for 20 m/s microjet case in the plane passing through the center of the microjet ($x = 0.0$): (a) averaged streamwise velocity and (b) averaged wall-normal velocity.

A comparison of line plots for the RANS-mj40 case and LES-mj40 case are shown in Figure 54(a) and Figure 54(b) for the averaged streamwise velocity (W) and averaged wall-normal velocity (V), respectively. The penetration of the microjet in the RANS case compares well with the LES case.

The RANS results for W compare well with LES at all the streamwise locations, except for over prediction close to the bottom wall at $z = 5.0$ and $z = 6.0$. This over prediction is due to the over prediction in the length of the recirculation zone. The value of Z_r for the RANS case is 9.64 as compared to 6.22 for the LES case. The over prediction of Z_r also leads to differences in the values of V between the RANS and LES results.

The penetration of the 40 m/s microjet is well predicted by RANS $k - \varepsilon$ model, while the penetration of the 20 m/s microjet is under predicted. As stated earlier a dense mesh ($\sim$ 10 million cells) for the RANS-mj20 case also did not improve the prediction. For both the microjet cases the same mesh resolution is utilized for RANS simulations and the current mesh resolves the flow accurately for the RANS-mj40 case because the mean velocity data for RANS-mj40 case compares well with the LES-mj40 data and experimental data. Therefore, the under prediction is not because of the mesh resolution in the RANS-mj20 case. Rather, the under prediction is due to the assumption of $k - \varepsilon$ turbulence models which are valid for high Reynolds number fully developed flows. In the case of the 20 m/s microjet, the Reynolds number is 2570 which is in the transitional range. Hence, the flow around the microjet is in the transitional range and cannot be predicted by RANS $k - \varepsilon$ turbulence models. For transitional flow modeling, LES is more accurate than RANS simulations.

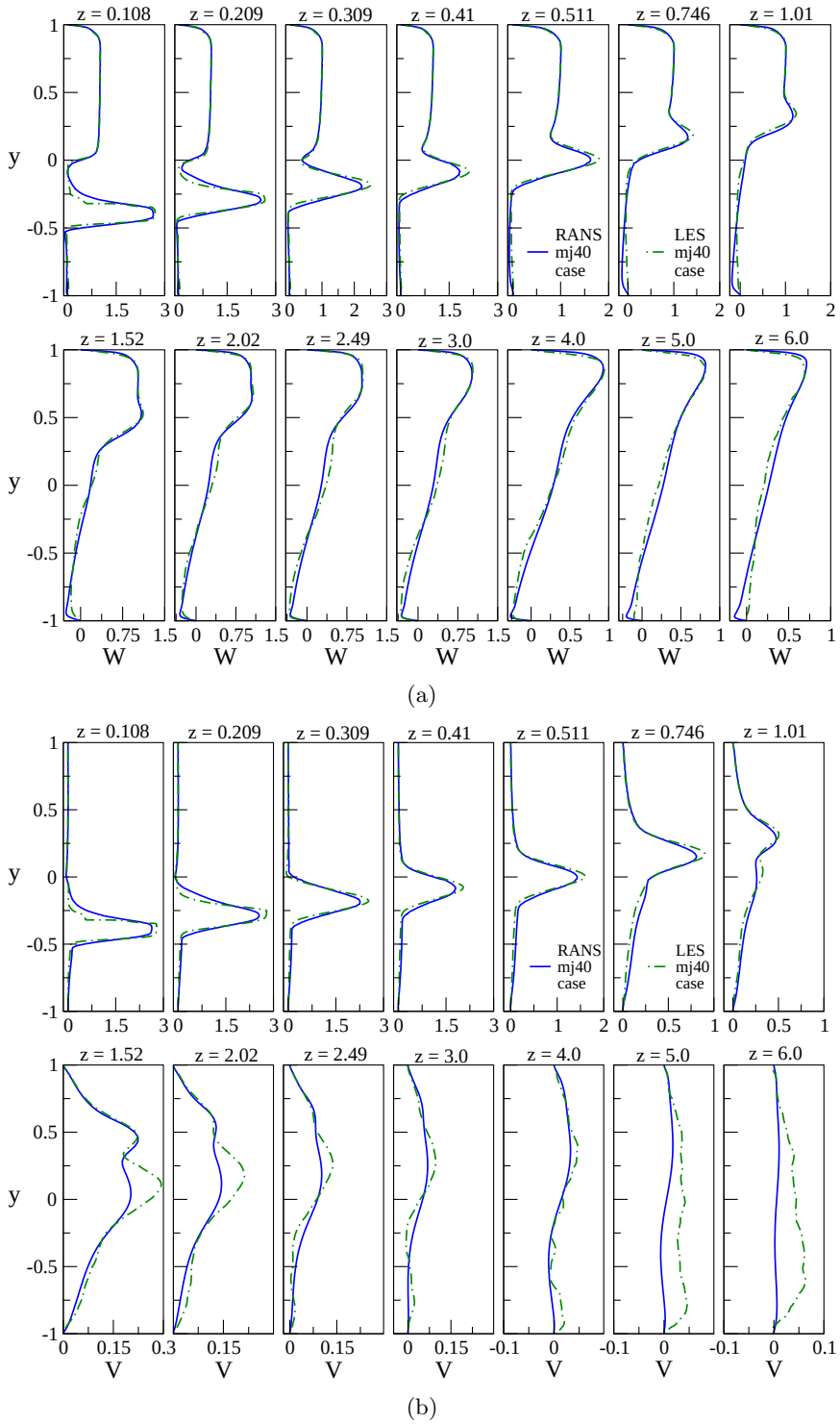

(a)

(b)

Figure 54. Comparison of RANS and LES line plots for 40 m/s microjet case in the plane passing through the center of the microjet ($x = 0.0$): (a) averaged streamwise velocity and (b) averaged wall-normal velocity.

5.5.2 Normal stresses and shear stresses

The comparison of streamwise velocity fluctuations (w_{rms}) and wall-normal velocity fluctuations (v_{rms}) are shown in Figure 55(a) and Figure 55(b), respectively. In the upstream region for the baseline case, the peak values for w_{rms} and v_{rms} are observed in the shear layer. However, close to the top wall the values of w_{rms} is comparable to the peak values in that plane. Close to the microjet exit and upstream of $z = 1.01$, the values of w_{rms} and v_{rms} for the microjet cases are higher than the baseline case. The microjets enter the domain and generate high velocity fluctuations because of the large gradients in the mean velocity, $\partial W/\partial z$ and $\partial V/\partial y$.

Two peaks in values of w_{rms} and v_{rms} are formed due to the large velocity gradient between the high velocity microjet and low velocity in the recirculation zones above and below the microjet. The presence of the microjet in the domain gives rise to two recirculation zones, one large and one small, as observed from the contours of streamwise velocity Figure 47. The large recirculation zone is formed below the microjet between the microjet and the bottom wall. The small recirculation zone is formed above the microjet between the microjet, the trailing edge of the step and the region where microjet impacts the primary shear layer. In the center region of the microjet the gradients of velocity are small, hence the value of normal fluctuations are small. However, the peak location for w_{rms} and v_{rms} are different. For w_{rms}, the streamwise velocity in the large recirculation zone is smaller, this gives rise to large gradients of streamwise velocity as compared to small recirculation zone. The opposite effect is observed in the value of v_{rms}, the large recirculation zone has higher values of wall-normal velocity as compared to

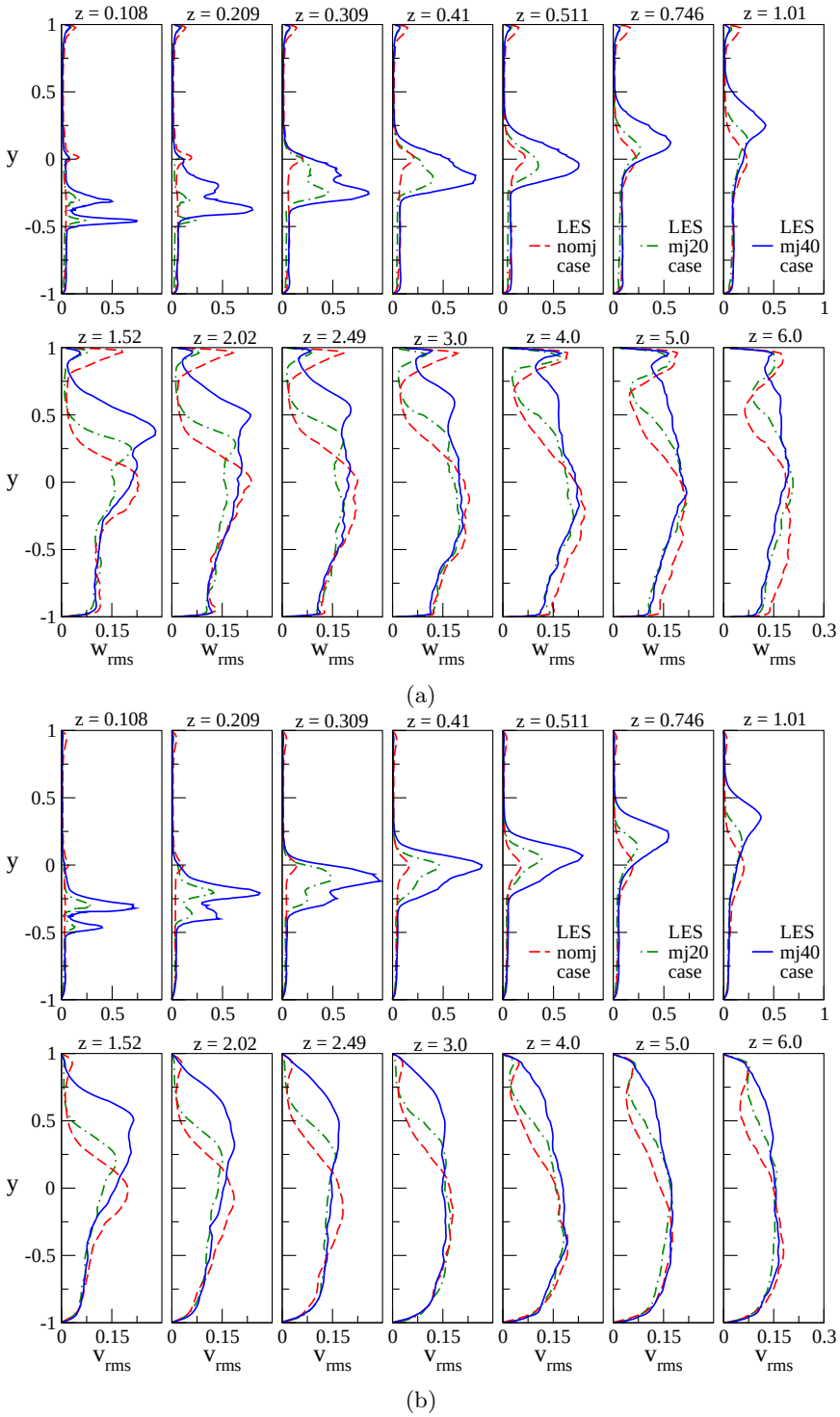

Figure 55. Comparison of line plots in the plane passing through the center of the microjet ($x = 0.0$) for the LES cases: (a) averaged streamwise velocity fluctuation and (b) averaged wall-normal velocity fluctuation.

the small recirculation zone. This gives rise to lower gradient of wall-normal velocity between the microjet and the large recirculation zone as compared to the small recirculation zone.

The two peak values in w_{rms} and v_{rms} exit till the microjet impacts the shear layer. As the microjet interacts with the shear layer, the peak values of w_{rms} and v_{rms} for the microjet cases rise in the wall-normal direction in each plane and follows the level of jet penetration. The 20 m/s jet has lower penetration and hence downstream of $z = 1.01$, the peak values of w_{rms} and v_{rms} reduce below the baseline case. With the higher penetration of the 40 m/s jet the peak values of velocity fluctuations reduces below the baseline case downstream of $z = 2.02$. However downstream of this location, the changes in the mean flow for the mj40 case around $y = 0.5$ give rise to peak values around $y = 0.5$. Downstream of $z = 2.02$ and below $y = 0.0$, the peak values of velocity fluctuations are comparable because the changes in the mean flow for all the cases are similar.

Figure 56 shows the comparison of the shear stresses, $\langle v'w' \rangle$, between the baseline case, LES-mj20 case and the LES-mj40 case. In the baseline case, the interaction of the positive streamwise values and negative wall-normal velocities give rise to negative values of $\langle v'w' \rangle$ in the shear layer. As the gradient of the mean streamwise velocity reduces along the streamwise locations, the width of the shear layer increases in the wall-normal direction. Upstream of $z = 2.02$, the peak values of $\langle v'w' \rangle$ are in the shear layer at $y = 0.0$. However downstream of this location and at $z \leq 3.0$, the interaction between the negative values of streamwise velocity and positive values of wall-normal velocity in the recirculation zone gives rise to peak values of $\langle v'w' \rangle$ that move downwards towards the bottom wall along the streamwise direction.

In the region before the microjet impinges the primary flow ($z = 0.5$), large positive values of shear stress are observed due to the interaction of low wall-normal velocity in the recirculation zone with the high streamwise velocity of the microjet. As observed for the normal stresses, two peaks in the values of $\langle v'w' \rangle$ are observed because of the interaction of the high microjet velocity with the low wall-normal velocity in the large and small recirculation zones.

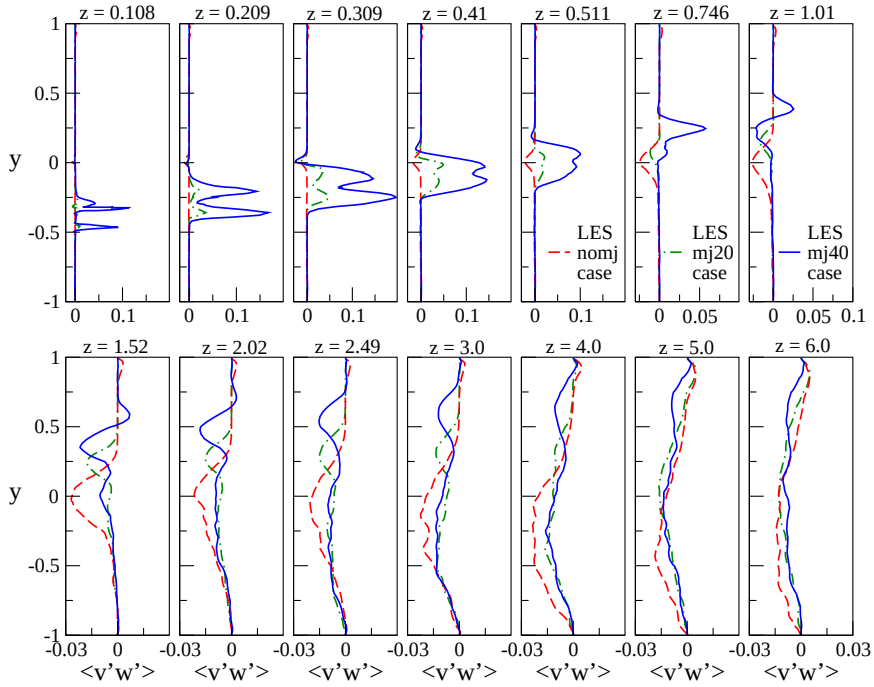

Figure 56. Comparison of Reynolds stresses between the LES cases in the plane passing through the center of the microjet, $x = 0.0$.

As the jet interacts with the primary flow and loses its momentum along the streamwise direction, the positive peak values of the $\langle v'w' \rangle$ vanish and negative peak values are observed. These negative values along with the positive velocity gradients enhance the production rate of turbulent kinetic energy. Downstream of $z = 0.511$, these negative peak values progressively move upward towards the top wall as the jet velocity increases. This shows that jet interacts with the primary flow, changes the shape of the shear layer and pushes the shear layer towards the top wall. However in the recirculation zone below $y = 0.0$, both the microjet cases provide similar values for $\langle v'w' \rangle$ because of similar behavior in the mean flow.

5.5.3 Turbulent kinetic energy

The previous discussion of the normal stresses and shear stresses lead to the important discussion of the jet turbulent kinetic energy (k) and its effect on the shear layer. A comparison of filtered turbulent kinetic energy for the baseline case, LES-mj20 case and LES-mj40 case is shown in Figure 57. The filtered turbulent kinetic energy is defined in Equation 5.1.

$$k = \frac{1}{2} \left\langle u_i' u_i' \right\rangle \tag{5.1}$$

In the baseline case, the peak turbulent kinetic energy occurs in the shear layer and progressively moves towards the bottom wall along the streamwise direction. The microjet enters the domain and generates high amounts of turbulent kinetic energy as compared to the baseline case. The higher turbulent kinetic energy of the 40 m/s jet has larger effect on the value of turbulent kinetic energy in the shear layer as compared to the 20 m/s jet. The peak values of turbulent

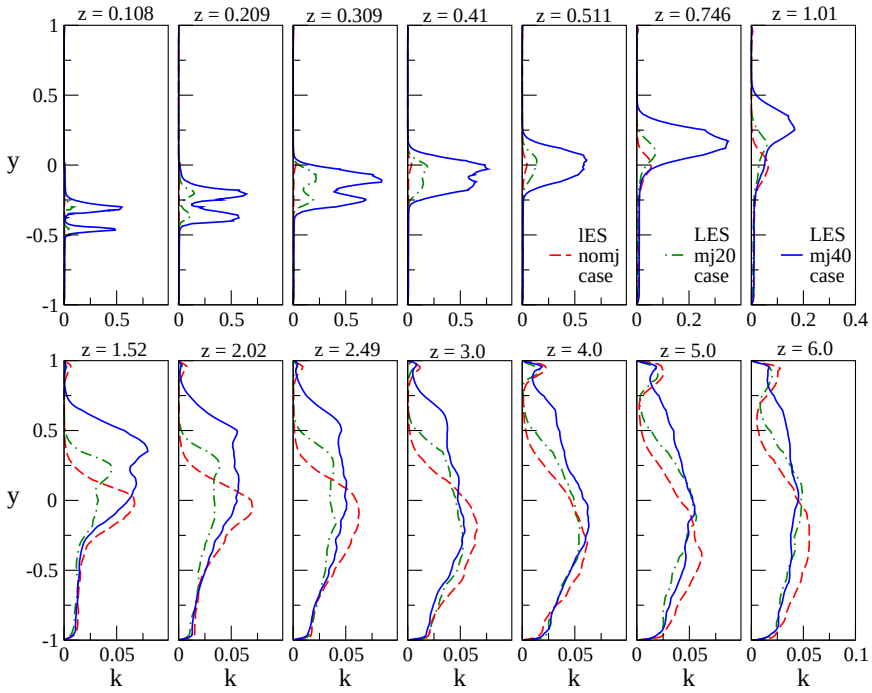

Figure 57. Comparison of filtered turbulent kinetic energy for the LES cases.

kinetic energy follows the change in the shape of the shear layer and moves upward towards the top wall. However, as the jet loses its momentum the value of peak turbulent kinetic energy reduces to below that of the baseline case.

For further analysis of the behavior of the turbulent kinetic energy, a comparison of the production rate of turbulent kinetic energy (P) is provided in Figure 58. For reference, the transport equation of turbulent kinetic energy (budget) is given in Equation 5.3, where the angled brackets represent Reynolds averaged components and U_j represents components of averaged velocity.

$$\underbrace{\frac{1}{2}\frac{\partial\left\langle u_i' u_i'\right\rangle}{\partial t}}_{\text{storage}} = \underbrace{-\frac{1}{2}U_j\frac{\partial\left\langle u_i' u_i'\right\rangle}{\partial x_j}}_{\text{convection}} \underbrace{-\left\langle u_i' u_j'\right\rangle\frac{\partial U_i}{\partial x_j}}_{\text{production}} \underbrace{-\frac{1}{2}\frac{\partial}{\partial x_j}\left\langle u_i' u_i' u_j'\right\rangle}_{\text{turbulent transport}} \tag{5.2}$$

$$+\underbrace{\frac{1}{2}\frac{1}{Re}\frac{\partial^2}{\partial x_j \partial x_j}\left\langle u_i' u_i'\right\rangle}_{\text{viscous diffusion}} \underbrace{-\left\langle u_j'\frac{\partial p'}{\partial x_j}\right\rangle}_{\text{pressure transport}} \underbrace{-\frac{1}{Re}\left\langle\frac{\partial u_i'}{\partial x_j}\frac{\partial u_i'}{\partial x_j}\right\rangle}_{\text{viscous dissipation}}$$

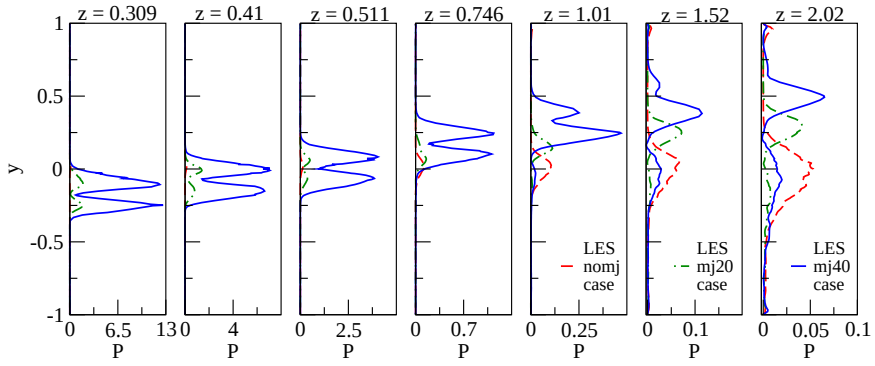

Figure 58. Comparison of production rate of turbulent kinetic energy (P) between the LES-baseline case, LES-mj20 case and LES-mj40 case.

The second term on the right hand side in Equation 5.3 is the rate of production term which consists of a sum of nine components. However, based on the values of v_{rms}, w_{rms}, $\langle v'w'\rangle$ and gradients of streamwise and wall-normal velocities, the contribution from four significant components to production rate of k, $P = -\left\langle u_i' u_j'\right\rangle \partial U_i/\partial x_j$, are analyzed and plotted in Figure 59.

The components are given in Equation 5.6 and as a note these components are scalar values and the subscript is only a notation used for ease of discussion.

$$P_{(22)} = \left\langle v'^2 \right\rangle \frac{\partial V}{\partial y} \tag{5.3}$$

$$P_{(23)} = \left\langle v' w' \right\rangle \frac{\partial V}{\partial z} \tag{5.4}$$

$$P_{(32)} = \left\langle w' v' \right\rangle \frac{\partial W}{\partial y} \tag{5.5}$$

$$P_{(33)} = \left\langle w'^2 \right\rangle \frac{\partial W}{\partial z} \tag{5.6}$$

Close to the microjet exit at $z = 0.309$, the large values of k in both the microjet cases are because of the velocity gradient terms $\partial V/\partial z$ and $\partial W/\partial z$ in $P_{(22)}$ and $P_{(33)}$, respectively, which contribute to the production rate of k. The two peaks are due to the peaks in the value of Reynolds stresses. The significant contribution to the values of k due to the interaction of the microjet with the shear layer comes from the terms $P_{(22)}$ and $P_{(33)}$. The production rate of k (P) follows the increase in the height of the shear layer in the wall-normal direction for the microjet cases. As the momentum of the jet decreases, the contribution to the values of k from the term $P_{(32)}$ become significant due to the shear generated by the gradient of mean flow, $\partial W/\partial y$. For the baseline case, the production of k occurs in the shear layer and the biggest contributor to the value k is from the term $P_{(32)}$. As the effect of the jet vanishes, the production rate of k in the baseline case is comparable to the 40 m/s microjet case at $z = 2.02$ and is higher than the 20 m/s microjet case at $z = 2.02$. This leads to higher values of k in the baseline case as compared to the microjet cases at $z = 2.02$.

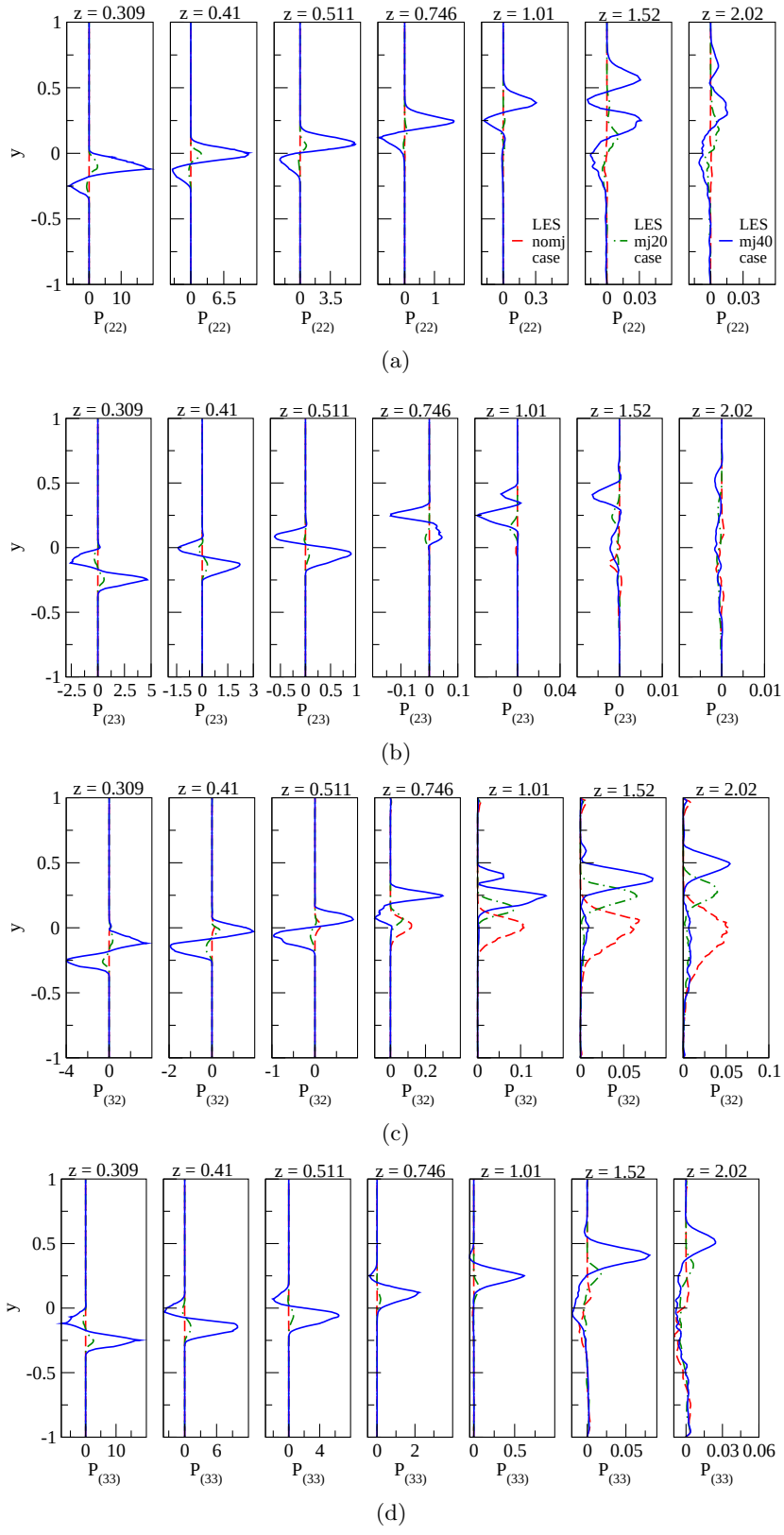

Figure 59. Comparison of components of P for the LES-baseline case, LES-mj20 case and LES-mj40 case: (a) $P_{(22)}$, (b) $P_{(23)}$, (c) $P_{(32)}$ and (d) $P_{(33)}$.

The last term on the right hand side of Equation 5.3 is the rate of viscous dissipation, ε, and a comparison of ε is shown in Figure 60. Close to the jet exit at $z = 0.309$, two peaks in the values of ε are observed because of the large gradients in the mean velocity. The two peak values of ε and P occur at the same wall-normal location at $z = 0.309$, however, as the jet penetrates the flow field only a single peak is observed and the peak value of ε occurs at a different location as compared to the peak values of P. As the jet expands, gradient of the mean flow reduces and the single peak value of ε moves towards the center of the peaks in P, at $z = 0.511$ and $z = 0.746$. The gradients of the mean flow due of the interaction of the jet and

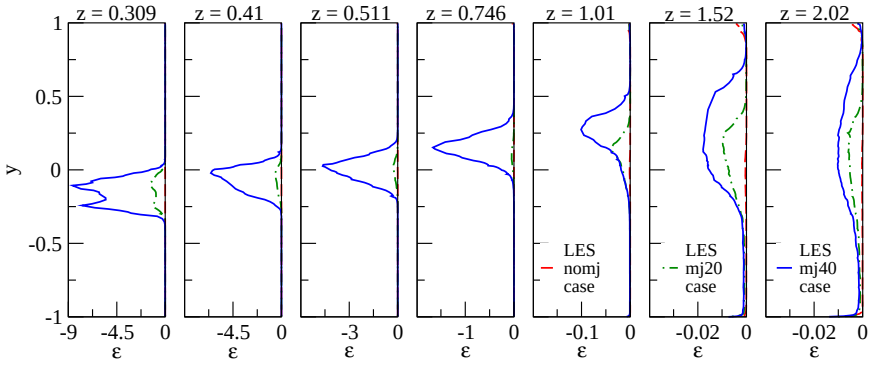

Figure 60. Comparison of viscous dissipation rate, ε, for the LES-baseline case, LES-mj20 case and LES-mj40 case.

the shear layer cause the peak value of ε to move toward the secondary peak of P, this effect occurs at $z = 0.511$ for the LES-mj20 case and at $z = 1.01$ in the LES-mj40 case. This change in location of peak values of ε and P signify the transport of k from regions where the local

values of the ratio of $P/\varepsilon > 1.0$ to region were the ratio is $P/\varepsilon < 1.0$. Before the jet impacts the shear layer, this ratio is higher than 1.0 on the edges of the jet. Hence, k is transported from the edge of the jet toward the center, where this ratio is less than 1.0. However, as the jet impacts the shear layer, this ratio is greater than 1.0 in the region where gradient of $\partial W/\partial y$ is higher, and hence the k is transported from this location to the other location as observed from the values of k.

Figure 61 compares the line plots of turbulent kinetic energy for the RANS and LES microjet cases. Close to the microjet exit, the RANS-mj20 case over predicts the value of turbulent kinetic energy of the microjet as compared to the LES-mj20 case. As the 20 m/s jet expands in the streamwise direction and its effect vanishes, the turbulent kinetic energy values of the RANS-mj20 case reduces and the values are closer to those from LES-mj20 case. For the 40 m/s microjet case, close to the microjet exit the values of turbulent kinetic energy for the RANS-mj40 case compare well with the values from LES-mj40 case. However, as the 40 m/s jet penetrates the flow field, RANS-mj40 case under predicts the values of turbulent kinetic energy as compared to LES-mj40 case. Downstream of $z = 0.746$, the trends in values of turbulent kinetic energy predicted by RANS resutls for both the microjet cases are similar to the those for the LES cases.

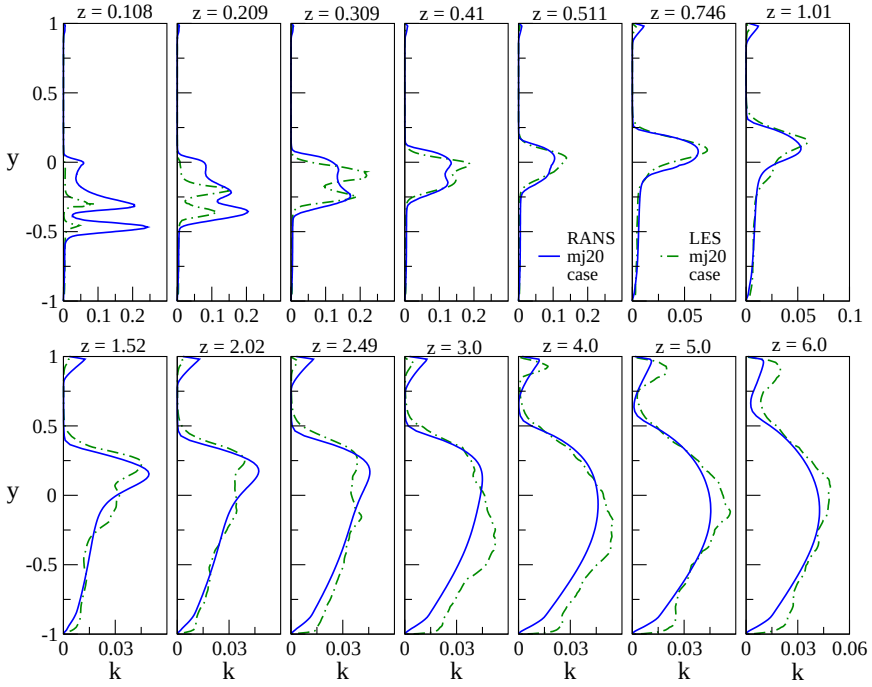

(a) mj20 case

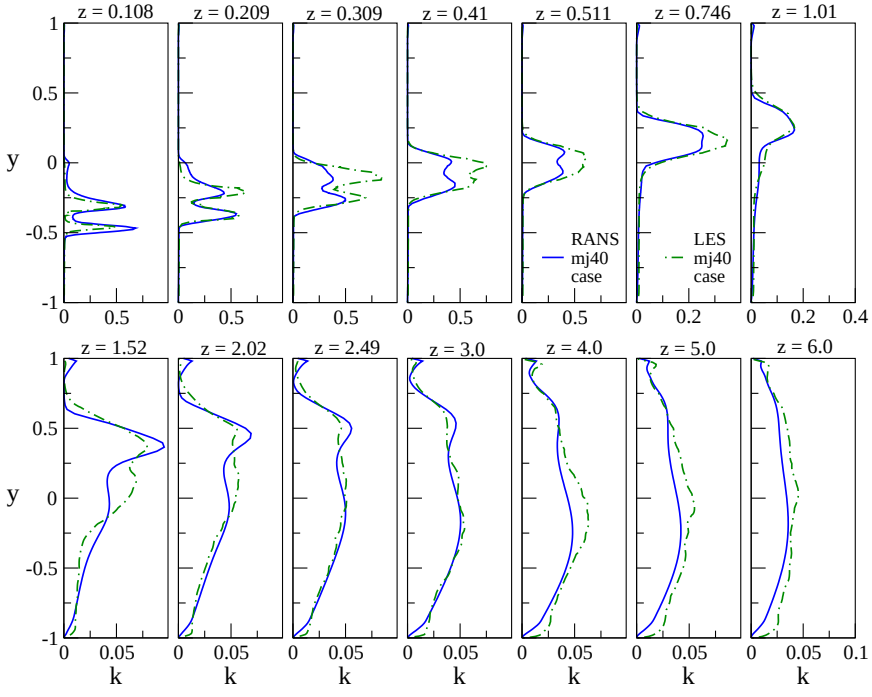

(b) mj40 case

Figure 61. Comparison of turbulent kinetic energy line plots between RANS and LES in the plane passing through the center of the microjet ($x = 0.0$): (a) 20 m/s microjet case and (b) 40 m/s microjet case.

5.5.4 Vorticity field

The jet impinges on the primary flow field and displaces the fluid in the spanwise direction. The jet also drags the fluid in the streamwise direction and this give rise to a secondary motion in the form of counter-rotating vortex pair. Figure 62 shows the comparison of average streamwise vorticity contours, $\langle \omega_z \rangle$, for the LES-mj20 case and the LES-mj40 case, in different streamwise locations. The 40 m/s case shows higher values of $\langle \omega_z \rangle$ as compared to the 20 m/s case. As the jet velocity increases, the size of the counter-rotating vortex pair increases and it moves towards the top wall in the streamwise direction. The counter-rotating vortex is the main mechanism by which the surrounding fluid is entrained into the jet. The higher values of the $\langle \omega_z \rangle$ contours for the LES-mj40 case suggest that there is higher entrainment of surrounding fluid in this case as compared to the LES-mj20 case.

5.5.5 Passive scalar

The contours of average mass fraction, $\langle Y \rangle$, in the plane passing through the center of the microjet ($x = 0.0$) are shown in Figure 63. The contours of $\langle Y \rangle$ spread more towards the top wall in the case of 40 m/s microjet as compared to the 20 m/s microjet case. The primary flow interacts with the low momentum 20 m/s jet and hampers the spreading of $\langle Y \rangle$ due to the bending of the jet. This effect is observed further downstream in the LES-mj40 case and is consistent with jet trajectories discussed earlier in Figure 48.

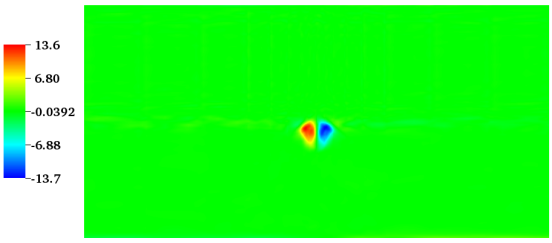

(a) LES-mj20: z = 0.4

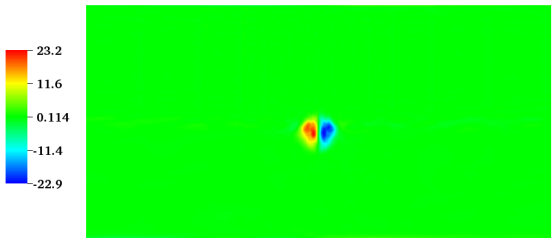

(b) LES-mj40: z = 0.4

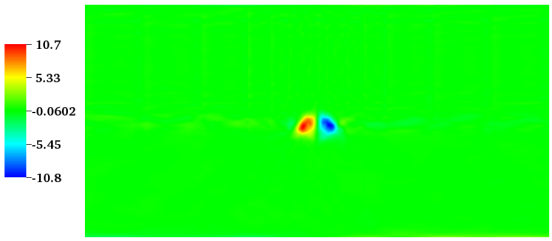

(c) LES-mj20: z = 0.5

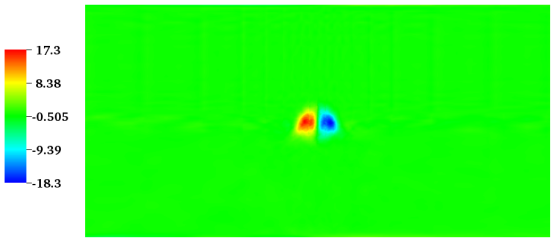

(d) LES-mj40: z = 0.5

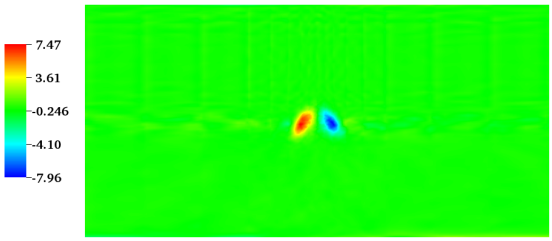

(e) LES-mj20: z = 0.6

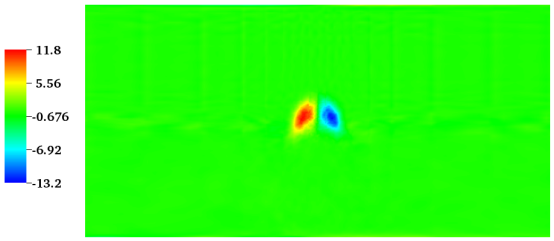

(f) LES-mj40: z = 0.6

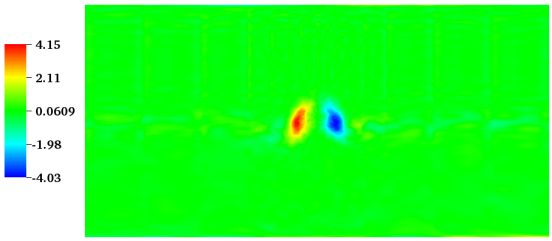

(g) LES-mj20: z = 0.8

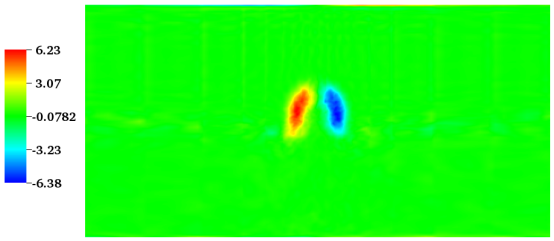

(h) LES-mj40: z = 0.8

Figure 62. Average streamwise vorticity, $\langle \omega_z \rangle$, generated by the 20 m/s and 40 m/s jets in the streamwise planes.

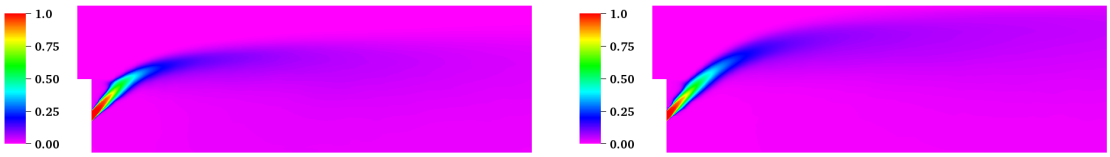

(a) LES-mj20: x = 0.0 (b) LES-mj40: x = 0.0

Figure 63. Contours of $\langle Y \rangle$ for the 20 m/s and 40 m/s microjet cases in the plane passing through the center of the microjet, $x = 0.0$.

The effect of the microjet on the contours of $\langle Y \rangle$ for the LES-mj20 case and LES-mj40 case, in different streamwise planes, are shown in Figure 64. For clarity rest of the domain is clipped and only a small square region is shown. The square region in all the streamwise planes is centered at $(x, y) = (0.0, 0.0)$ and extends to $(-0.7, 0.7)$ in the x-direction (spanwise) and y-direction (wall-normal), respectively.

The microjet impacts the primary shear layer at $(x, y, z) = (0.0, 0.0, 0.5)$ and entrains the surrounding fluid due to the counter-rotating vortex pair. This causes the spreading of the passive scalar in the wall-normal and spanwise directions, leading to a bean shape of the passive scalar in the streamwise direction. The extent of the spreading of the $\langle Y \rangle$ in the wall-normal direction depends on the effect of microjet on the shear layer. Using a line $y = 0.0$ in the shear layer as reference, the 20 m/s microjet has minimal effect on the shear layer and hence the passive scalar spreading is around the line $y = 0.0$ in all the streamwise planes. The 40 m/s microjet displaces the fluid to a greater extent and hence the spreading of the passive scalar rises above $y = 0.0$ along the streamwise direction.

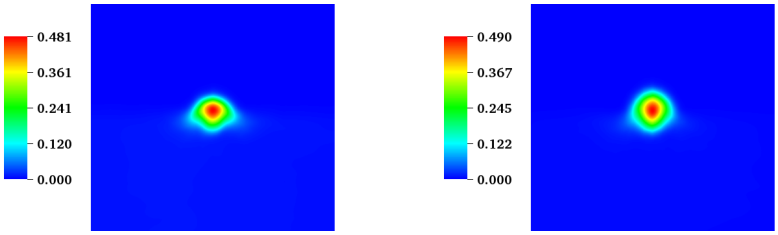

(a) LES-mj20: z = 0.5

(b) LES-mj40: z = 0.5

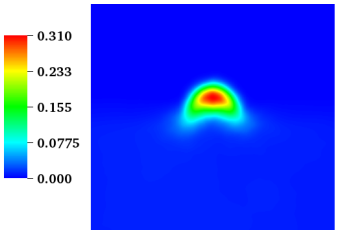

(c) LES-mj20: z = 0.7

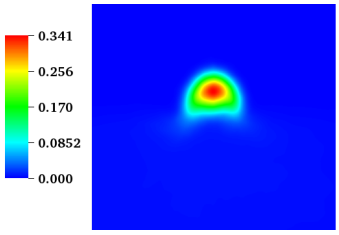

(d) LES-mj40: z = 0.7

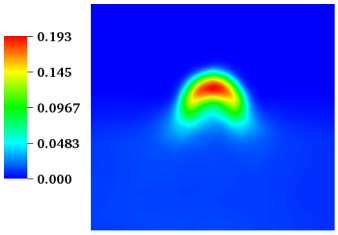

(e) LES-mj20: z = 1.0

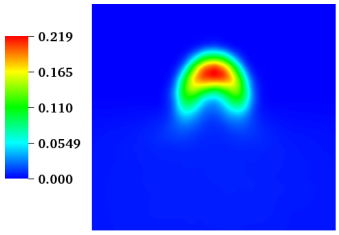

(f) LES-mj40: z = 1.0

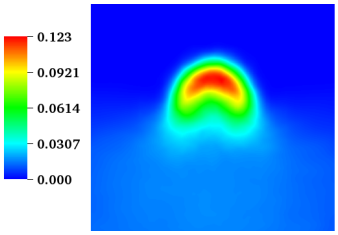

(g) LES-mj20: z = 1.5

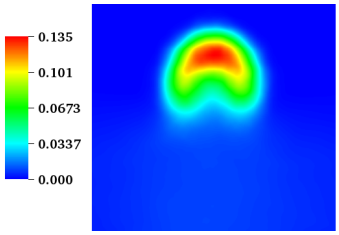

(h) LES-mj40: z = 1.5

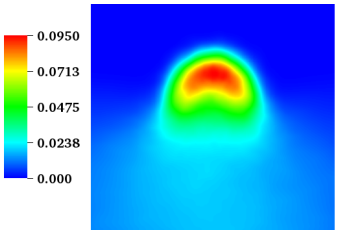

(i) LES-mj20: z = 2.0

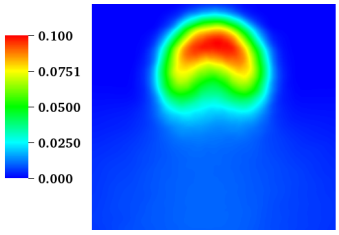

(j) LES-mj40: z = 2.0

Figure 64. Comparison of averaged mass fraction contours for the LES-mj20 case and LES-mj40 case in the streamwise planes.

At $z = 0.5$, the primary flow interacts with the lower momentum of 20 m/s microjet and starts spreading $\langle Y \rangle$ in the spanwise direction; while, the higher momentum of the 40 m/s microjet carries $\langle Y \rangle$ deeper into the flow filed. Along the streamwise direction, the entrainment of the surrounding fluid diminihses as the effect of the jet vanishes and intensity of streamwise vorticity decreases. For the 20 m/s microjet case, the effect of the jet vanishes around $z = 0.75$, hence downstream of the $z = 0.7$ the shear layer starts spreading the passive scalar. This effect is delayed for the 40 m/s microjet case because of the greater penetration of the jet, to about $z = 1.5$. The spreading of $\langle Y \rangle$ due to the interaction of the 40 m/s microjet with the shear layer, downstream of $z = 1.0$, leads to a circular shape of the $\langle Y \rangle$ at $z = 2.0$, this effect is absent in 20 m/s microjet case. There is a variation in the spreading of passive scalar in the upstream and downstream region for the 40 m/s jet as compared to the 20 m/s jet. In the upstream region, the spreading is lower and is higher in the downstream region.

Figure 65 shows the comparison of contours of $\langle Y \rangle$ for the RANS-mj20 case and LES-mj20 case at streamwise location $z = 1.0$ and $z = 1.5$. The RANS-mj20 results exhibit a lower penetration of the 20 m/s jet due to greater spreading of the jet. This low momentum jet interacts with the incoming primary flow and gives rise to the shape of $\langle Y \rangle$ contours which differs from the LES-mj20 case. The peak value of $\langle Y \rangle$ for the RANS-mj20 case is higher than that for the LES-mj20 case. This shows that at the streamwise planes, there is lower spreading of the jet in the RANS-mj20 case as compared to the LES-mj20 case.

Figure 66 shows the comparison of contours of $\langle Y \rangle$ for the RANS-mj40 case and LES-mj40 case at streamwise location $z = 1.0$ and $z = 1.5$. RANS simulations predicts a greater

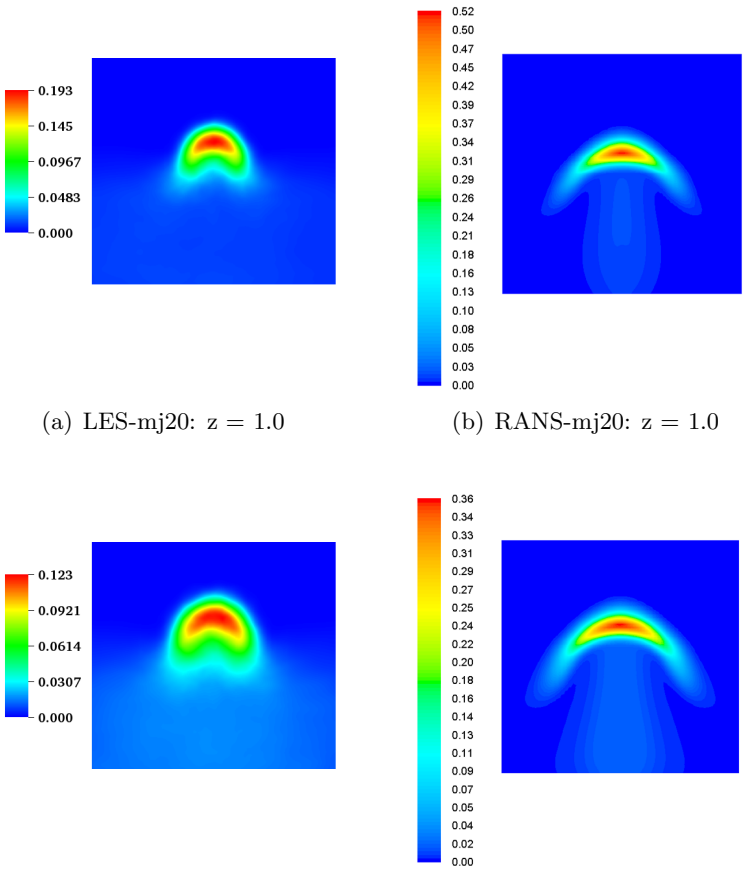

(a) LES-mj20: z = 1.0 (b) RANS-mj20: z = 1.0

(c) LES-mj20: z = 1.5 (d) RANS-mj20: z = 1.5

Figure 65. Comparison of averaged mass fraction contours for RANS-mj20 case and LES-mj20 case at the streamwise planes $z = 1.0$ and $z = 1.5$.

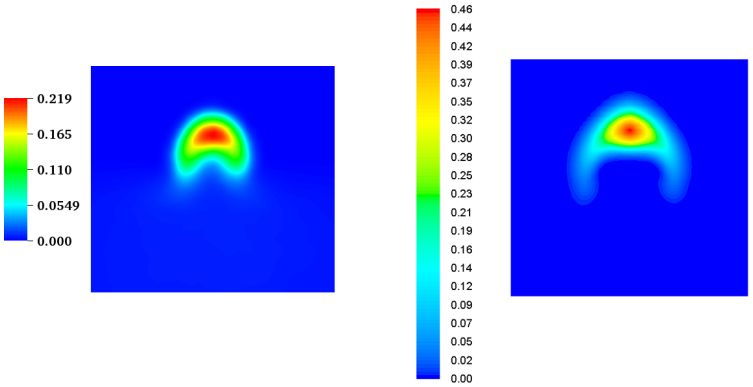

(a) LES-mj40: z = 1.0 (b) RANS-mj40: z = 1.0

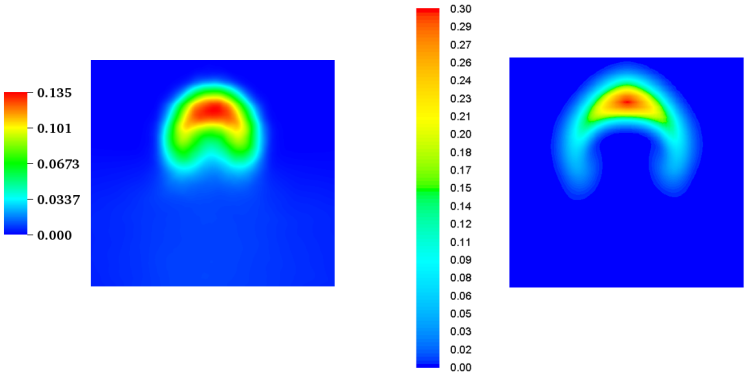

(c) LES-mj40: z = 1.5 (d) RANS-mj40: z = 1.5

Figure 66. Comparison of averaged mass fraction contours for RANS-mj40 case and LES-mj40 case at the streamwise planes $z = 1.0$ and $z = 1.5$.

displacement of the fluid in the spanwise direction and wall-normal direction, this leads to greater spreading of $\langle Y \rangle$ in these two directions. RANS predicts lower spreading of the $\langle Y \rangle$ as compared to LES results which is evident from the higher peak values of $\langle Y \rangle$ in the RANS-mj40 case as compared to LES-mj40 case. The lower spreading of the mass fraction causes the shape of the $\langle Y \rangle$ contours to differ from that observed for LES-mj40 case.

5.6 Quantification of scalar mixing

The aim of simulating the passive scalar is to quantify the mixing of the scalar due to the microjet. The spreading of the averaged mass fraction $\langle Y \rangle$ signifies the mixing of the scalar. To quantify mixing, two-dimensional rectangular Cartesian grids with constant z at various streamwise locations and spanning the entire domain in x and y are utilized. In the post-processing stage the averaged mass fraction field is interpolated on to the grids and the desired quantities are then computed on these grids. Three indices are utilized to assess mixing efficiency: uniformity index (UI), temporal mixing deficiency (TMD) and mixedness parameter (MIX).

5.6.1 Uniformity index (UI)

The definition of UI given in Equation 5.7 measures the uniformity in space, which is applied to the time averaged mean value Y_i at the i^{th} point.

$$UI = \frac{Y_{pl}^{rms}}{Y_{pl}} \tag{5.7}$$

where,

$$Y_{pl} = \frac{1}{A_{pl}} \sum_{i=1}^{n} a_i Y_i \tag{5.8}$$

$$Y_{pl}^{rms} = \sqrt{\frac{1}{A_{pl}} \sum_{i=1}^{n} a_i \left(Y_i - Y_{pl}\right)^2} \tag{5.9}$$

$$A_{pl} = \sum_{i=1}^{n} a_i \tag{5.10}$$

Here, a_i denotes the area weight of the i^{th} point, A_{pl} denotes the total area of the considered plane, Y_{pl} denotes the mean of $\langle Y \rangle$ in the plane and Y_{pl}^{rms} the related fluctuation of $\langle Y \rangle$ in the considered plane.

Figure 67 shows the results obtained for the uniformity index (UI) at different z-planes in the microjet cases. The values of UI drop substantially for both the microjet cases along the streamwise direction reflecting better mixing. The values for the LES-mj20 case are lower than those of the LES-mj40 case. Closer to the microjet exit, the higher momentum of the 40 m/s jet delays the uniform spreading of the scalar which gives higher values of UI. The lower momentum 20 m/s jet interacts with the primary flow leading to spreading of the mass fraction and lower values of UI, closer to the microjet exit. Around $z = 1.5$, there is sudden change in the value of UI for the LES-mj20 case because of the spreading of the passive scalar by the shear layer, as observed in Figure 64. For the LES-mj40 case between $z = 1.5$ and $z = 4.0$, there is a gradual change in the values of UI with a higher slope of the UI curve than LES-mj20 case because of two effects; first, the uniform spreading of $\langle Y \rangle$ due to the counter rotating vortex pair and second, the spreading of $\langle Y \rangle$ due to the shear layer after the effect of the jet vanishes. Overall, it can be concluded from the values of UI that there is better mixing of the passive scalar in the LES-mj20 case as compared to the LES-mj40 case.

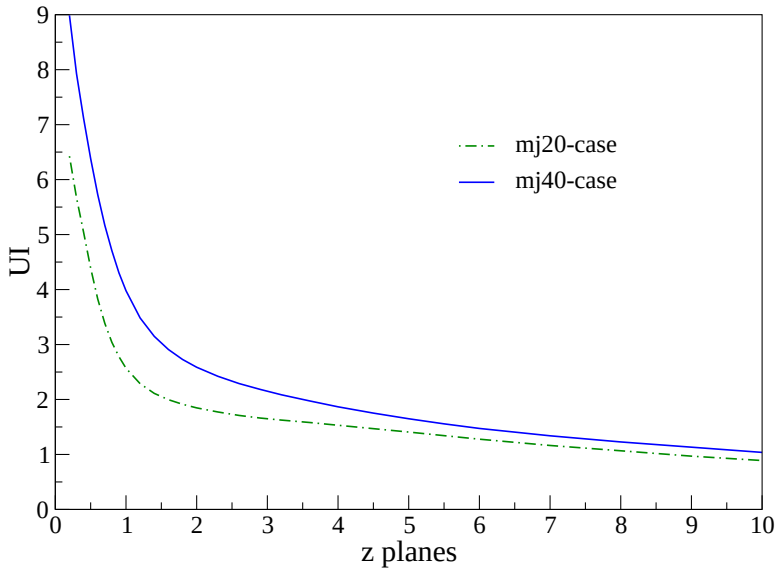

Figure 67. Comparison of UI for LES-mj20 and LES-mj40 cases.

5.6.2 Temporal mixing deficiency (TMD)

The TMD definition given in Equation 5.11 measures the uniformity in time by means of time averaged rms value y_i' at the i^{th} point.

$$TMD = \frac{1}{A_{pl}} \sum_{i=1}^{n} a_i \left(\frac{y_i'}{Y_i} \right) \tag{5.11}$$

Here, A_{pl} denotes the total area of the considered plane and Y_i denotes the time averaged mean value.

The normalization applied in this definition is the time average mean value Y_i. The results are averaged in each plane to obtain a single value for comparison. This normalization is

problematic for the microjet cases, since remote from the plane passing through the center of the microjet the mean mass fraction values tend to zero generating large values which overshadow the information from the microjet itself. Hence, the averaging is performed over the points where $Y_i > 0.01$.

The temporal mixedness is measured by the TMD curves shown in Figure 68. The values of TMD are higher for the LES-mj40 case as compared to the LES-mj20 case, closer to the microjet exit. The intermittency of mass fraction increases with increasing microjet velocity indicating a lower level of mixing. As observed in the UI curves, there is a sudden change in value of TMD around $z = 1.5$ in the LES-mj20 case because of the spreading of the passive scalar by the shear layer. The behavior of the LES-mj40 case is similar to that observed in the UI curve. The TMD curves for the microjet cases shows that there is higher level of mixing in the LES-mj20 case as compared to the LES-mj40 case.

5.6.3 Mixedness parameter (MIX)

The definition of MIX given in Equation 5.12 measures the portion of the mixed fluids in the considered plane.

$$MIX = \frac{1}{A_{pl}} \sum_{i=1}^{n} a_i Y_i (1 - Y_i) \tag{5.12}$$

Here, A_{pl} denotes the total area of the considered plane and Y_i denotes the time averaged mean value. The lower values of MIX indicate greater mixing of the fluids in the computational domain. To make the calculation independent of the A_{pl}, only points where $Y_i > 0.01$ are utilized for the calculation.

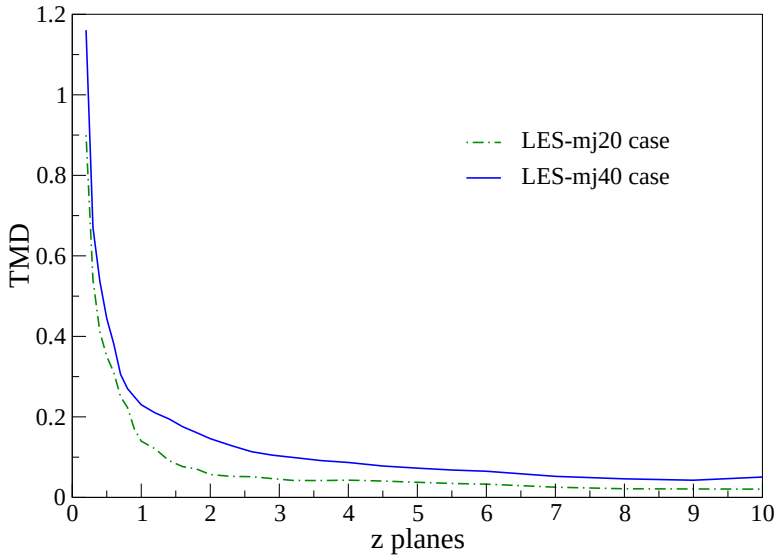

Figure 68. Comparison of TMD for LES-mj20 and LES-mj40 cases.

Figure 69 shows the values of MIX for the LES-mj20 case and LES-mj40 case in different streamwise planes. As observed in the UI and TMD plots, the higher momentum of the 40 m/s case delays the mixing of the fluids and hence, results in higher values of MIX. There is greater mixing of the fluids in the LES-mj20 case because of the interaction of the primary flow with the low momentum microjet. Downstream of $z = 1.0$, the value of MIX changes suddenly because of the loss in jet momentum and an increase in mixing by the shear layer. For the LES-mj40 case, the values of MIX reduce slowly due to the mixing of the mass fraction by the counter rotating vortex pair and then by the shear layer. Overall, the values for MIX shows that the LES-mj20 case has better mixing than the LES-mj40 case.

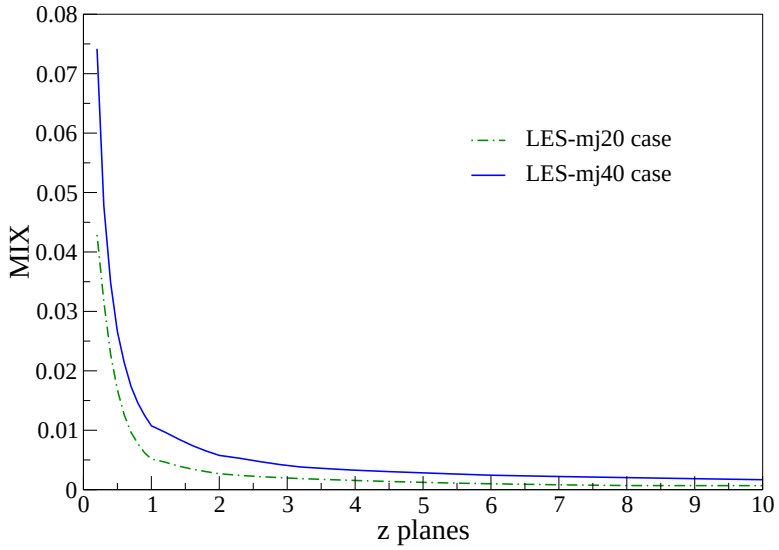

Figure 69. Comparison of MIX for LES-mj20 and LES-mj40 cases.

5.7 Conclusions

This chapter presents results from LES studies of the effect of a single microjet in flow over a backward facing geometry using the spectral element method. The microjet is placed on the step face and enters the geometry at an angle of 45° to the step face. The results are compared for three cases, a baseline case without microjet and two microjet cases, LES-mj20 and LES-mj40, with jet velocities 20 m/s and 40 m/s, respectively. A passive scalar (mass fraction) is introduced through the microjet to evaluate mixing of the passive scalar due to the microjet. In addition, RANS simulations are performed on the same geometry in the framework of $k-\varepsilon$ turbulence models and compared to the LES results.

This LES study to capture the dynamics of the interaction between the microjet and the primary shear layer in a backward-facing step geometry is the first of its kind. The results for averaged streamwise velocity and averaged streamwise normal fluctuations show good agreement with the experimental data. This validates the implicit LES (no model) technique for sub-grid dissipation mechanism in studying the effect of microjet.

RANS $k-\varepsilon$ turbulence model is utilized for modeling high Reynolds number fully developed turbulent flow and is not appropriate for modeling transitional flow around the 20 m/s microjet. However, the model provides good comparison with the experimental data and LES data for the 40 m/s microjet case.

In the baseline case without microjet, the shear layer is primarily two-dimensional. However, in the single microjet case, the microjet imparts three-dimensionality to the shear layer by displacing the primary flow in wall-normal and spanwise directions. The height of the shear layer increases in the wall-normal directions with increasing microjet velocity. The higher turbulent kinetic energy of the 40 m/s jet displaces the primary flow to a greater extent than the 20 m/s jet. Till the extent of jet penetration, the normal stresses and mean velocity gradients are the significant contributors to a large production in turbulent kinetic energy. With the increasing height of the shear layer and loss in jet momentum, the changes in the mean flow and shear stress values start contributing to the production of turbulent kinetic energy. The higher momentum of the 40 m/s jet leads to higher values of vorticity as compared to the 20 m/s case.

The entrainment of the surrounding fluid due to the counter-rotating vortex pair is the primary mixing mechanism of the mass fraction. The trajectory of the 20 m/s jet bends due to interaction with the primary flow; while, the 40 m/s jet penetrates deeper into the flow field. The momentum of the 40 m/s jet carries the mass fraction deeper into the flow field and leads to lower spreading of the mass fraction as compared to the 20 m/s jet. The mixing indices UI, TMD and MIX have higher values close to the microjet exit, indicating a lower level of mixing in the LES-mj40 case in the upstream region as compared to the LES-mj20 case. However in the downstream section, the counter-rotating vortex pair increases the spreading of the passive scalar due to higher vorticity. The values of UI, TMD and MIX reduce at the higher rate for the LES-mj20 case indicating a higher level of mixing as compared to the LES-mj40 case.

All the discussions presented in this chapter are aimed at establishing a process which can be followed to perform future LES studies on the effect of microjet in a backward-facing step flow.

CHAPTER 6

CONCLUSIONS AND FUTURE WORK

The objective of this thesis is to explore the use of microjets as an effective control mechanism to improve the performance of dump combustors using CFD tools. RANS simulations are utilized for performing various parametric studies to arrive at a finalized design for the implementation of microjets in dump combustors. LES studies are performed on the finalized combustor design for a more accurate understanding of the fluid dynamics using a semi-implicit Legendre spectral element code, Nek5000.

RANS simulations have shown that adding microjets in dump combustors significantly increases the heat release rate in a round (axisymmetric) and planar (asymmetric) dump combustors. Microjets are placed on the dump plane and angled at 45^{o} to the flow axis. The strong shear introduced by the microjets generates high levels of turbulent kinetic energy and increases the flame surface area due to the wrinkling effect. This significantly enhances the mixing of the reactants with the products, thus exposing the reactants to high temperatures that are essential for combustion. Compared to the baseline case without microjets, simulations show that adding microjets results in an increase in heat release rate of $\sim 22\%$ and $\sim 140\%$ in round and planar dump combustors, respectively. The finalized design for implementation of microjets in planar dump combustor is utilized for experimental validation. The data collected from the experiments qualitatively confirm the trends predicted by the simulations (2).

The percentage increase in the heat release rate at highest microjet velocity, relative to the baseline case, is large in the planar combustor compared to the round combustor. However, in spite of the large heat release rate in the planar combustor, still the majority of the fuel exits the combustor without participating in chemical reaction. Future desing studies with RANS simulations can be conducted to test different placements of the microjet on the step face for improving the fuel burning efficiency of the planar dump combustor.

LES studies with Nek5000 are conducted using the technique of implicit LES with no sub-grid model. Two different backward-facing step configurations are simulated at Reynolds numbers 5000 and $28,000$ to test the implicit LES technique. The simulations results of Nek5000 for averaged streamwise velocity data compare well with the published experimental data and DNS results. Hence, explicit filtering is a viable choice for sub-grid dissipation mechanism in LES studies using spectral element method.

The validated implicit LES technique is utilized for performing LES studies in a planar dump combustor with microjets. Adopting a step by step approach to tackle this problem, as a start non-reacting cases with only "one" microjet in the backward-facing step geometry are simulated with microjet velocities of 20 m/s and 40 m/s. For both the microjet velocities, the averaged streamwise velocity profiles and streamwise root-mean-squared (rms) velocity profiles are in good agreement with the experimental data. The microjet, entering the geometry at 45^{o} angle to the step face, imparts three dimensionality to the shear layer by displacing the primary flow and giving rise to a counter-rotating vortex pair. The entrainment of the surrounding fluid due to the counter-rotating vortex pair is the primary mixing mechanism of the passive scalar.

The momentum of the 40 m/s jet carries the passive scalar deeper into the flow field and leads to lower spreading of the mass fraction as compared to the 20 m/s jet. The mixing indices show that the mixing of the passive scalar varies for the two microjet cases in the upstream and downstream regions. The 20 m/s jet case has higher mixing in the upstream region; while, the 40 m/s jet has higher mixing in the downstream region.

This thesis has established a process that can be utilized to perform future LES studies on the effect of microjet in a backward-facing step flow. The current analysis is a first attemt at analyzing the effect of microjet. Further grid resolution studies need to be performed for the 20 m/s and 40 m/s case along with more analysis on the interaction of the microjet with the primary flow. From RANS simulations it is observed that the higher microjet velocities exhibit higher heat release rates and hence, are the most effective. Therefore, LES studies of non-reacting flow with microjet velocities of 60 m/s and 80 m/s can be part of future studies. To capture the interaction between microjets, future LES studies can be performed with a configuration of two microjets placed on the step face, a certain distance apart. Finally, moving towards the goal of simulating LES of reacting flow, Nek5000 can be developed for simulating reacting flow cases at different microjet velocities.

Although LES studies give a more accurate representation of the fluid dynamics as compared to RANS simulations, there is an important issue with respect to turnaround time of LES cases that need to be addressed. The computational time required for future LES studies with higher microjet velocity is going to be large because of the smaller time step size dictated by the CFL condition. In addition, the complexity of reacting flow simulations will further add

to the high computational cost, thus increasing the turnaround time for LES. However, the RANS simulations compare well with the LES results for the 40 m/s microjet case. Hence, RANS simulations can be utilized for predicting trends with new desing concepts which can be experimentally validated with lower turnaround time than LES. Therefore, RANS simulations present the best approach for testing future design concepts on the use of microjets as an effective control mechanism in dump combustors.

CITED LITERATURE

1. Forliti, D. J. and Strykowski, P. J.: Controlling turbulence in a rearward-facing step combustor using countercurrent shear. Journal of Fluids Engineering-Transactions of the ASME, 127(3):438–448, 2005.

2. Kanchi, H., Russell, K., Anderson, M. J., Beard, S. P., Strykowski, P. J., and Mashayek, F.: Fluidic control with microjets in dump combustors. International Journal of Heat and Mass Transfer, 54(25–26):5395–5405, 2011.

3. Sengupta, K., Russell, K., and Mashayek, F.: Numerical simulation of counter-current dump combustor for effecient flame stabilization. AIAA Paper, pages 2006–0174, 2006.

4. Sengupta, K., Russell, K., Taha, A., and Mashayek, F.: Shear flow control in dump combustor using microjets. in the Proceedings of the 20th ONR Propulsion Meeting, Washington, DC, December, 2007.

5. Russell, K., Sengupta, K., and Mashayek, F.: Effect of subsonic microjets on cold flow in dump combustors. AIAA Paper 2008–0167, 2008.

6. Alkislar, M. B., Choutapalli, L., Krothapalli, A., and Lourenco, L. M.: The effect of microjet control in aeroacoustics of supersonic twin jets. AIAA Paper 2004–11, 2004.

7. Arakeri, V. H., Krothapalli, A., Siddavaram, V., Alkislar, M. B., and Lourenco, L. M.: On the use of microjets to supress turbulence in a mach 0.9 axisymmetric jet. Journal of Fluid Mechanics, 490:75–98, 2003.

8. Greska, B. and Krothapelli, A.: Jet noise reduction using aqueous microjet injection. AIAA Paper 2004–2974, 2004.

9. Altay, H. M., Speth, R. L., Snarheim, D., Hudgins, D. E., Ghoniem, A. F., and Annaswamy, A. M.: Impact of microjet actuation on stability of a backward-facing step combustor. AIAA Paper 2007–563, 2007.

10. Altay, H. M., Hudgins, D. E., Speth, R. L., Annaswamy, A. M., and Ghoniem, A. F.: Mitigation of thermoacoustic instability utilizing steady air injection near the flame anchoring zone. Combustion and Flame, (157):686–700, 2010.

11. So, R. M. C. and Ahmed, S. A.: Effects on axisymmetric sudden expansion flows. Journal of Propulsion and Power, 4(3):270–274, 1988.

12. So, R. M. C. and Ahmed, S. A.: Characteristics of dump combustor flows. International Journal of Heat and Fluid Flow, 10(1):60–64, 1989.

13. Gould, R. D., Stevenson, W. H., and Thompson, H. D.: Simultaneous velocity and temperature measurements in a premixed dump combustor. Journal of Propulsion and Power, 10(5):639–645, 1994.

14. Mishra, D. P. and Vishak, T.: Computational studies of turbulent premixed flame based dump cobmustor. Fuel, 86:2881–2889, 2007.

15. Muppidi, S. and Mahesh, K.: Study of trajectories of jets in crossflow using direct numerical simulations. Journal of Fluid Mechanics, 530:81–100, 2005.

16. Muppidi, S. and Mahesh, K.: Direct numerical simulation of passive scalar transport in transverse jets. Journal of Fluid Mechanics, 598:335–360, 2008.

17. Yuan, L. L., Street, R. L., and Ferziger, J. H.: Large-eddy simulations of a round jet in crossflow. Journal of Fluid Mechanics, 379:71–104, 1999.

18. Denev, J. A., Frohlich, J., and Bockhorn, H.: Large eddy simulation of a swirling transverse jet into a cross flow with investigation of scalar transport. Physics of Fluids, 21(1):3354–3366, 2009.

19. Kanchi, H., Sengupta, K., and Mashayek, F.: Effect of turbulent inflow boundary condition in les of flow over a backward-facing step using spectral element method. International Journal of Heat and Mass Transfer, 62:782–793, 2013.

20. Sengupta, K., Russell, K., and Mashayek, F.: Step geometry and countercurrent effects in dump combustor, part 1: Cold flow. AIAA Journal, 45(8):2033–2041, 2007.

21. Magnussen, B. F. and Hjertager, B. H.: On mathematical modeling of turbulent combustion with special emphasis on soot formation and combustion. 16th Symposium (International) on Combustion, pages 719–729, 1976.

22. Kanchi, H., Russell, K., Mashayek, F., Anderson, M. J., Beard, S. P., and Strykowski, P. J.: Experimental and computational studies to advance operability and performance of combustion systems adopting fluidic control. in the Proceedings of the 22nd ONR Propulsion Meeting, Crystal City, VA, June, 2010.

23. Patera, A. T.: A spectral element method for fluid dynamics: laminar flow in channel expansion. Journal of Comput. Physics, 54:468–488, 1984.

24. Fischer, P. F., Lottes, J. W., and Kerkemeier, S. G.: nek5000 Web page: http://nek5000.mcs.anl.gov, 2008.

25. Maday, Y., Patera, A. T., and Ronquist, E. M.: An operator-integration-factor splitting method for time-dependent problems: Application to incompressible fluid flow. Journal of Scientific Computing, 5(4):263–292, 1990.

26. Deville, M. O., Fischer, P. F., and Mund, E. H.: High-order methods for incompressible fluid flow. Cambridge, UK, Cambridge University Press, 2002.

27. Blackburn, H. M. and Schmidt, S.: Spectral element filtering techniques for large eddy simulation with dynamic estimation. Journal of Computational Physics, 186:610–629, 2003.

28. Fischer, P. F. and Mullen, J. S.: Filter based stabilization of spectral element methods. Comptes Rendus a l'Academie des Sciences Paris, Ser. 1, Anal. Numer, 332:265–270, 2001.

29. Levin, J. G., Iskandarani, M., and Haidvogel, D. B.: A spectral filtering procedure for eddy-resolving simulations with a spectral element ocean model. Journal of Computational Physics, 137:130–154, 1997.

30. Karamanos, G. S.: Large eddy simulation using unstructured spectral/hp finite elements. Doctoral dissertation, Imperial College, London, 1999.

31. Karamanos, G. S. and Karniadakis, G. E.: A spectral vanishing viscosity method for large-eddy simulations. Journal of Comput. Physics, 163:22–50, 2000.

32. Domaradzki, J. A., Loh, K. C., and Yee, P. P.: Large eddy simulations using the subgrid scale estimation model and truncated Navier-Stokes dynamics. Theor. and Comput. Fluid Dynamics, 15(6):421–450, 2002.

33. Mathew, J., Lechner, R., Foysi, H., Sesterhenn, J., and Friedrich, R.: An explicit filtering method for large-eddy simulation of compressible flows. Physics of Fluids, 15:2279–2289, 2003.

34. Bogey, C. and Bailly, C.: Computation of a high Reynolds number jet and its radiated noise using large eddy simulation based explicit filtering. Computers and Fluids, 35:1344–1358, 2006.

35. Fischer, P., Lottes, J., Siegel, A., and Palmiotti, J.: Large-eddy simulation of wire-wrapped fuel pins I: Hydrodynamics in a periodic array. Joint Intl. Topical Meet. on Mathematics and Computation and Supercomp. in Nuclear Appl., Monterey, CA, 2007.

36. Sengupta, K.: Direct and large-eddy simulation of compressible flows with spectral/hp element methods. Ph.D. Thesis, University of Illinois at Chicago, Chicago, IL, 2009.

37. Boyd, J. P.: Two comments on filtering (artificial viscosity) for chebyshev and legendre spectral and spectral element methods: preserving boundary conditions and interpretation of the filter as a diffusion. J. Comput. Phys., 143(1):283–288, June 1998.

38. Mullen, J. S. and Fischer, P. F.: Filtering techniques for complex geometry fluid flows. Comm. Numer. Meth. Eng, 15:9–18, 1999.

39. Arnal, M. and Friedrich, R.: Large-eddy simulation of turbulent flows with separation. In 8th Symposium on Turbulent Shear Flows, pages 169–187. Springer-Verlag, Berlin, 1993.

40. Li, N., Balaras, E., and Piomelli, U.: Inflow conditions for large-eddy simulations of mixing layers. Physics of Fluids, 12:935–938, 2000.

41. Lund, T., Wu, X., and Squires, D.: Generation of turbulent inflow data for spatially-developing bounday layer simulations. Journal of Computational Physics, 140:233–258, 1998.

42. Lee, S., Lele, S., and Moin, P.: Simulation of spatially evolving turbulence and the applicability of Taylor's hypothesis in compressible flow. Physics Fluids A, 4:1521–1530, 1992.

43. Le, H., Moin, P., and Kim, J.: Direct numerical simulation of turbulent flow over a backward-facing step. Journal of Fluid Mechanics, 330:349–374, 1997.

44. Shinozuka, M.: Simulation of multivariate and multidimensional random processes. Journal of Acoustical Society of America, 49(1):357–368, 1971.

45. Schueller, G. I.: A state-of-the-art report on computational stochastic mechanics. Probabilistic Engineering Mechanics, 12(4):197–321, 1997.

46. Deodatis, G.: Simulation of ergodic multivariate stochastic precesses. Journal of Engineering Mechanics, 122(8):778–787, 1996.

47. Glaze, D. J. and Frankel, S. H.: Stochastic inlet conditions for large-eddy simulation of a fully turbulent jet. AIAA Journal, 41(6):1064–1073, 2003.

48. Klein, M., Sadiki, M., and Janicka, J.: A digital filter based generation of inflow data for spatially developing direct numerical or large-eddy simulations. Journal of Computational Physics, 186:652–665, 2003.

49. Jarrin, N., Benhamadouche, S., Laurence, D., and Prosser, R.: A synthetic-eddy-method for generating inflow conditions for large-eddy simulations. International Journal of Heat and Fluid Flow, 27:585–593, 2006.

50. Jovic, S. and Driver, D. M.: Backward-facing step measurement at low Reynolds number, Re_h=5000. NASA Tech. Mem. 108807, NASA, 1994.

51. Akselvoll, A. and Moin, P.: Large-eddy simulation of turbulent confined coannular jets and turbulent flow over a backward-facing step. Report, Dept. Mechanical Engineering TF-63, Stanford University, 1995.

52. Spalart, P. R.: Direct simulation of a turbulent boundary-layer up to $R_\theta = 1410$. Journal of Fluid Mechanics, 187:61–98, 1988.

53. Adams, E. W., Johnston, J. P., and Eaton, J. K.: Experiments on the structure of turbulent reattaching flows. Report, Thermosciences Division, Dept. Mechanical Engineering MD-43, Stanford University, 1984.

54. Gao, Z. and Mashayek, F.: Stochastic model for nonisothermal droplet-laden turbulent flows. AIAA Journal, 42(2):255–260, 2004.

55. Box, G. E. P. and Jenkins, G. M.: Time series analysis. Oakland, CA, Holden-Day, 1976.

56. Choi, H. and Moin, P.: Effects of the computational time step on numerical solutions of turbulent flows. Journal of Computational Physics, 113:1–4, 1994.

VITA

Harish P. Kanchi

Personal Information

Phone (work): (312) 413-9662

Email: hkanch1@uic.edu

EDUCATION:

Ph.D.	University of Illinois at Chicago	2013
M.S.	University of Illinois at Chicago	2006
B.E.	University of Pune	2001

PROFESSIONAL EXPERIENCE:

- Technical Service Engineer, ANSYS, Inc., September 2012 - Present
- Doctoral Research Assistant, Department of Mechanical and Industrial Engineering, University of Illinois at Chicago, August 2008 - August 2012
- Teaching Assistant, Department of Mechanical and Industrial Engineering, University of Illinois at Chicago, August 2008 - August 2012
- Graduate Assistant, TRIO Programs and African American Academic Network, University of Illinois at Chicago, February 2004 - August 2008
- Sales Engineer, Ritech Hydraulics Pvt. Ltd., October 2002 - June 2003
- Sales and Service Engineer, Greaves Limited, March 2002 - July 2002

JOURNAL PUBLICATIONS

1. Kanchi, H., Sengupta, K., and Mashayek, F.: Effect of turbulent inflow boundary condition in les of flow over a backward-facing step using spectral element method. International Journal of Heat and Mass Transfer, 62:782–793, 2013.
2. Kanchi, H., Russell, K., Anderson, M. J., Beard, S. P., Strykowski, P. and Mashayek, F.: Fluidic control with microjets in dump combustors. International Journal of Heat and Mass Transfer, 54(25–26):5395–5405, 2011.
3. Kanchi, H. and Masud, A.: A 3D Adaptive mesh moving scheme. International Journal for Numerical Methods in Fluids, 54(6–8):923–944, 2007.

4. Chakrabarti, S., Barnett, J., Kanchi, H., Mehta, A. and Yim, J.: Design Analysis of a Truss Pontoon Semi-Submersible Concept in Deep Water using Morison Equation. Journal of Ocean Engineering, 34(3–4):621–629, 2007.

AWARDS AND HONORS

- Litvin Graduate Honor Award, 2012
- University of Illinois Alumni Association Student Leadership Award, 2011
- Chancellor's Student Service and Leadership Award, 2011

LEADERSHIP EXPERIENCE

- Member on Search Committee for Vice Chancellor for Academic Affairs and Provost
- Memeber of Student Activities Funding Committee
- Treasurer of UIC Graduate Student Council
- President of Mechanical and Industrial Engineering Graduate Students Association
- President of Indian Graduate Students Association